Planetesimal Formation via Fluffy Dust Aggregates

Akimasa Kataoka

Department of Astronomy

Graduate University for Advanced Studies

This dissertation is submitted for the degree of

Doctor of Philosophy

2014

Abstract

Dust coagulation is the first step of planet formation. However, several theoretical problems still remain in dust coagulation models. One of the main problems is the radial drift barrier, which is a problem that dust grains with a size of 1 m quickly fall onto the central star and no planetesimal can form. In addition, laboratory experiments and numerical simulations found other problems: the fragmentation and the bouncing problems. The former is that dust grains experience high speed collisions resulting in collisional disruption, and the latter is that dust grains collide but sometimes bounce and do not form larger bodies. By contrast, astronomical observations have evidenced the grain growth in protoplanetary disks, which are the birthplace of extra-solar planets. It has been shown that protoplanetary disks possess millimeter-sized dust grains. Thus, we have to construct the dust coagulation theory overcoming the theoretical problems to explain the formation of planetary systems being consistent with the disk observations.

This thesis aims to elucidate the dust coagulation process by introducing porosity evolution of dust aggregates. In protoplanetary disks, dust grains stick to each other to form porous structure. These clusters are called dust aggregates. Dust grains are thought to form extremely porous aggregates in protoplanetary disks. However, compression mechanisms to form compact planetesimals are still uncertain. For example, it has been shown that collisional compression is inefficient to compress highly porous aggregates. Therefore, compression mechanisms other than collisions are required to explain planetesimal formation.

In this thesis, we introduce static compression of porous dust aggregates. First, we perform numerical simulations of dust aggregates and derive the compressive strength of porous dust aggregates. The derived compressive strength has a form of $P = (E_{\rm roll}/r_0^3)\phi^3$, where $E_{\rm roll}$ is the rolling energy, r_0 is the monomer radius, and ϕ is the filling factor of dust aggregates. We also analytically derive the formula and confirm the results of the numerical simulations. In addition, the derived formula smoothly connects to the results of laboratory experiments of relatively compact silicate aggregates.

Next, in order to introduce the static compression to dust coagulation in protoplanetary

disks, we consider two origins of static compression, which are due to gas drag and self-gravity. As a result, we show the overall porosity evolution of dust aggregates in protoplanetary disks: dust grains coagulate to form fluffy aggregates, and then they are compressed by the gas-drag pressure and their self-gravity to form planetesimals. The size and mass of the planetesimals are consistent with comets in the solar system, which are believed to be the remnants of planetesimals. Moreover, we found that icy aggregates are free from the three problems of planetesimal formation, which are the radial drift, fragmentation, and bouncing problems. In this way, the proposed scenario is the first coherent theory of dust coagulation from grains to planetesimals.

Finally, to investigate the observational properties of porous dust aggregates, we calculate the opacities of porous dust aggregates. We find that the opacities of porous dust aggregates are characterized by the product of the aggregate radius and the filling factor, except for the case where the aggregate radius is similar to the wavelength. The results suggest that the aggregate radius and the filling factor mostly degenerate in observations. They also suggest that the millimeter-wave emission of protoplanetary disks, which has been interpreted as the emission from compact millimeter-sized grains, can be interpreted as the emission from the extremely porous dust aggregates. In addition, we also derive the analytical expressions of the absorption and scattering opacities of porous dust aggregates, which will greatly reduce the computational costs to calculate the opacity. Moreover, we find a difference in absorption opacity between compact and highly porous aggregates caused by the interference, which occurs when aggregate radius is similar to observation wavelengths. Using the difference, we propose a way to distinguish between compact grains and fluffy dust aggregates in expected future observations.

Contents

Chapter 1

Background

Planets are believed to form by coagulation of dust grains in circumstellar disks around young stars. The disks are called protoplanetary disks. When young stars form, dust grains are as tiny as 0.1 μm. In protoplanetary disks, dust grains are believed to stick to each other due to molecular force and form kilometer-sized planetesimals. They further stick due to their gravity, and finally form planets. However, how dust grains coagulate and grow to planetesimals is still unknown: there are mainly three problems in planetesimal formation, which are the radial drift, the fragmentation, and the bouncing problems. The first problem is that when dust grains coagulate to form 1 meter sized bodies, they quickly fall onto the central star and thus no planetesimals can form (e.g., Adachi et al., 1976; Weidenschilling, 1977). The second is that collisional energy of dust grains is so large that they are disrupted in protoplanetary disks (e.g., Blum & Münch, 1993). The third is that dust grains collide other grains and sometimes do not stick but bounce (e.g., Zsom et al., 2010).

By contrast, observations of protoplanetary disks suggest grain growth. Sub-mm observations suggest that the maximum size of dust grains is 1 mm at least in the outer part of the disk (e.g., D'Alessio et al., 2001). From a viewpoint of dust dynamics in disks, 1 mm-sized grains have to radially migrate inward due to the same mechanism of the radial drift barrier.

In order to explain planetesimal formation, several ideas have been proposed (e.g., Johansen et al., 2007; Okuzumi et al., 2012; Windmark et al., 2012a). However, there has been no conclusive scenario of planetesimal formation.

One of the promising scenarios is to introduce porosity evolution on dust coagulation. Porous dust aggregates possibly overcome the radial drift barrier due to the rapid growth (Okuzumi et al., 2012) and overcome the bouncing due to their porous structure (Wada et al., 2008), and icy aggregates can overcome the fragmentation problem due to their stickiness (Wada et al., 2009).

However, the fluffy growth scenario also has problems. Once dust grains form porous aggregates, the aggregates are not effectively compressed by collisions, but their filling factor becomes $\sim 10^{-5}$ (Okuzumi et al., 2012). This is inconsistent with the properties of planetesimals, which are believed to be compact. In addition, there has been no observational evidence on highly porous aggregates. The link between porous aggregates and observations is still missing.

Therefore, finding other mechanisms to compress the aggregates to form planetesimals is a way to construct a coherent scenario of planetesimal formation. Moreover, the growing dust aggregates must be consistent with observations of protoplanetary disks. In this thesis, we will introduce static compression as a new compression mechanism of porous dust aggregates. In addition, we investigate the observational properties of the porous dust aggregates.

As an introduction to this thesis, in this chapter, we first introduce the three problems in planetesimal formation. Next, we also introduce the observational results to be explained. Then, we explain the strategy of this thesis toward the planetesimal formation theory. In Chapter 1.1, we denote the basic dynamics of dust grains in protoplanetary disks to introduce the radial drift barrier. In Chapter 1.2, we introduce the laboratory experiments and the numerical simulations of dust collisions to introduce the bouncing and fragmentation problems. In Chapter 1.3, we introduce the porosity evolution and explain the problem for compression of porous dust aggregates. In Chapter 1.4, we introduce the results of the observations of protoplanetary disks, which illustrate the grain growth. The planetesimal formation model has to explain the observations. In Chapter 1.5, we describe the goals and the strategy of this thesis, which are to construct a successful scenario of planetesimal formation by introducing the static compression.

1.1 Dust dynamics: introducing the radial drift barrier

Dust grains, which are the seeds of planets, commonly spread in the Universe. In the region of dense molecular clouds, stars are formed by gravitational collapse (Larson, 1969). At this stage, dust grains inside the clouds are also contracted and form larger bodies because of their high density, which yields to planets. If dust grains collide each other with sufficiently low velocities, they stick to form larger bodies. Their collision frequency strongly depends on the spatial density of dust grains. In molecular-cloud phase, however, the collision frequency of grains is too low to make larger bodies in a free-fall timescale (Ormel et al., 2009; Ossenkopf, 1993). Therefore, the birthplace of planets should be more dense.

The protoplanetary disks are good cradles of dust coagulation.

In this section, we review theoretical modelings of dust growth and dynamics in protoplanetary disks. For the modeling, we first describe the disk model that we use. Then, we derive the dynamics of gas and dust grains in the disk. In the derivation of the dynamics, we introduce the radial drift barrier and explain possibilities to overcome the barrier.

1.1.1 Protoplanetary disks

The gas of molecular cloud cores has an angular momentum in their collapsing phase. Thus, the gas does not fall in spherical symmetry, but form a disk-like structure. This disk is believed to become a protoplanetary disk. The formation process of protoplanetary disks in the context of star formation is currently under debate (e.g., Machida et al., 2010). Thus, we do not proceed to the formation process of the disk, but use a simple model of disk structure.

Protoplanetary disks have been usually modeled with simple power-law density and temperature distributions. Here, the gas surface density Σ is taken to be $\Sigma = \Sigma_0(R/1\mathrm{AU})^{-p}$ and temperature to be $T = T_0(R/1\mathrm{AU})^{-q}$. Hayashi et al. (1985) proposed a minimum mass solar nebula model (MMSN), where the solid distribution corresponds to the averaged planet-mass distribution in our solar system. The dust temperature is derived by balancing between the heating by stellar radiation and the cooling by blackbody radiation at each location. In the MMSN model, Σ_0 is usually taken to be $\Sigma_0 = 1700$ g cm^{-2}, the surface density power to be $p = 1.5$, T_0 to be $T_0 = 280$ K, and the temperature power to be $q = 1/4$. The dust mass fraction is usually assumed to be 1/100 of the gas, which is the value in the interstellar medium.

However, the temperature distribution is not appropriate for protoplanetary disks in star-forming regions. Protoplanetary disks are optically thick at infrared wavelengths, and thus the radiation from the central star does not penetrate into the disk midplane. As a result, the midplane temperature is considered to be much lower than the MMSN model. Chiang & Goldreich (1997) proposed the two-layered model, where the disk is composed of the surface layer which is directly irradiated by the central star and the midplane which is indirectly heated by the surface layer (see Appendix of Tanaka et al. 2005 for the analytical expressions). This model well reproduces the observed SEDs of protoplanetary disks (Chiang et al., 2001; D'Alessio et al., 2001). Figure 1.1 represents the temperature at the disk midplane and the disk surface (Chiang et al., 2001). The model of T_{BB} corresponds to the optically thin disk model. We note that, in the two-layerd model, the midplane temperature is remarkably lower than the surface temperature. This greatly affects the dust coagulation

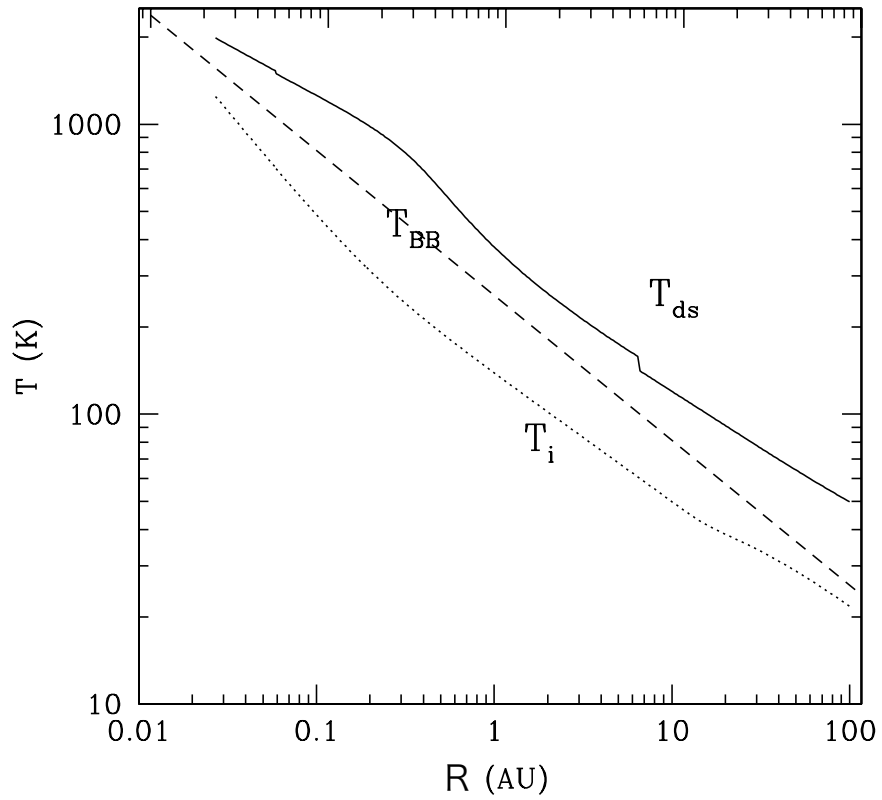

Fig. 1.1 The temperature distributions at the disk midplane and at the surface layer. $T_{\rm i}$ represents the temperature at the disk midplane, $T_{\rm ds}$ at the disk surface, and $T_{\rm BB}$ where the temperature is determined by blackbody radiation. The figure is originally from Fig.5 of Chiang et al. (2001).

in protoplanetary disks, such as coagulation efficiency, location of the snowline, and the scale height of the disk.

As a fiducial case, in this thesis, we adopt the surface density of the MMSN model, where $\Sigma_0 = 1700$ g cm^{-2} and $p = 1.5$, and adopt the temperature profile of that of Chiang et al. (2001) at the midplane.

1.1.2 Gas dispersal

The protoplanetary disks are thought to be accretion disks. The source of viscosity is believed to be the turbulent motion because of the magneto-rotational instability (Balbus & Hawley, 1991). In the modeling of disks, the viscous accretion usually modeled with α parameter such that

$$\nu = \alpha c_s h_g, \tag{1.1}$$

where c_s is the sound speed and h_g is the disk scale height (Lynden-Bell & Pringle, 1974; Shakura & Sunyaev, 1973), which we will discuss later. The accretion timescale can be estimated to be

$$t_{\rm diff} \sim \frac{R^2}{\nu}. \tag{1.2}$$

The timescale depends on the radius of the disk. If we take the value of $\alpha \sim 10^{-3}$ and the disk radius to be a few tens of AU, the dispersion timescale of the disk is $\sim 10^6$ years.

However, the mechanisms of the disk dispersion is still uncertain. Several mechanisms to explain the disk dispersal have been proposed, which are the viscous accretion (Lynden-Bell & Pringle, 1974), photoevaporation, stellar encounters, or the disk wind (see the review by Hollenbach et al., 2000). In the viewpoint of observations, infrared observations suggest that the dispersal timescale is between 10^6 and 10^7 years (Hernández et al., 2007). Figure 1.2 shows that the disk frequency for each star in star clusters. The disks are detected at infrared wavelengths. The result shows that the protoplanetary disks have a dissipation timescale of a few $\times 10^6$ years.

Here, we focus on dust coagulation in disks. The observational results suggest that the planet formation have to be completed within a few Myr.

1.1.3 Dynamics of gas particles and dust grains

In this section, we briefly summarize the motion of dust grains and disk gas. The dynamics of dust grains is strongly affected by the disk gas. If dust grains are small enough, they are strongly coupled to the gas. Thus, the dynamics of small grains are the same as that of the

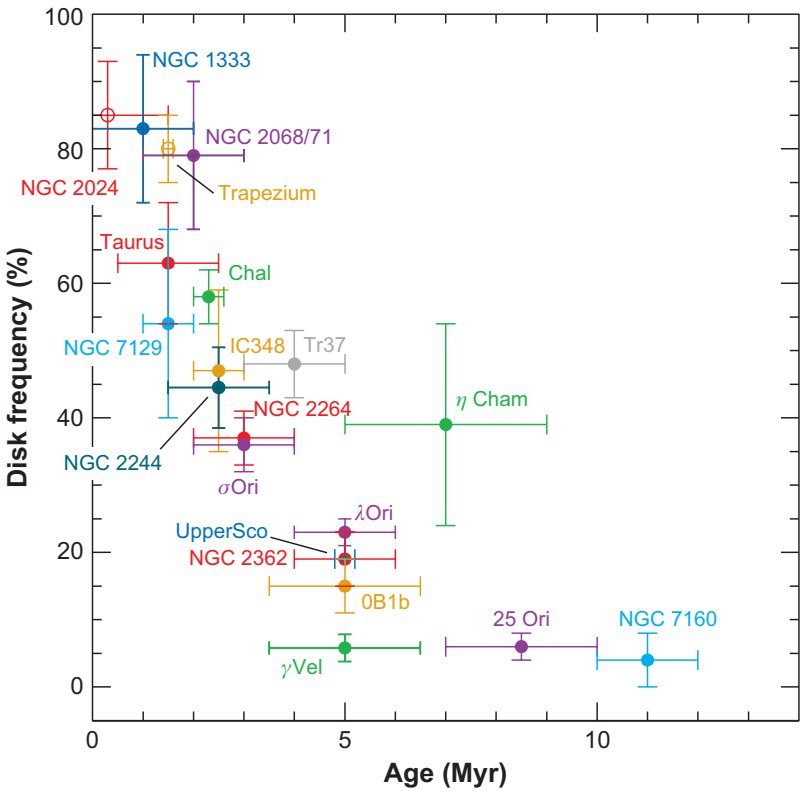

Fig. 1.2 The disk frequency for each star clusters against their ages. This figure represents the dissipation timescale of protoplanetary disks. The figure is taken from Fig.2 of Wyatt (2008).

disk gas. When dust grains coagulate to form larger bodies, they become decoupled from the gas, and thus their motion becomes different from the gas. In calculating the force acting on grains with a relative velocity v, there are two physical regimes (e.g., Adachi et al., 1976). If the dust radius is smaller than the mean free path of the gas, $a < \lambda_{\rm mfp}$, the gas behaves as particles at a scale of the dust grains and the drag force is called Epstein drag. If $a > \lambda_{\rm mfp}$, the drag force is determined by calculating the fluid flow, which is called Stokes drag. The drag force in these two regimes is described with the stopping time of dust grains, $t_s \equiv mv/F_{\rm drag}$, which represents the timescale to stop the relative motion of the dust grains against the gas. The stopping time is given by

$$t_s = \begin{cases} \dfrac{3m}{4\rho_g v_{\rm th} A} & (a < \dfrac{9}{4}\lambda_{\rm mfp}) \\ \dfrac{3m}{4\rho_g v_{\rm th} A}\dfrac{4a}{9\lambda_{\rm mfp}} & (a > \dfrac{9}{4}\lambda_{\rm mfp}) \end{cases} \tag{1.3}$$

where the dust radius is a, the dust mass m, the thermal velocity of dust grains $v_{\rm th} = \sqrt{8/\pi}c_s$, and $\lambda_{\rm mfp}$ the mean free path of the gas. The coupling efficiency between the grains and the gas is described with Stokes number, St, which is the stopping time of dust grains normalized by dynamical timescale. Thus, the Stokes number is defined as St= $t_s\Omega_{\rm K}$.

Next, we derive the basic motions of dust and gas. For simplicity, we assume that the dust to gas mass ratio is much less than unity. The basic equations of motions of the dust grains and gas are given by

$$\frac{d\boldsymbol{v}_d}{dt} = -\frac{\boldsymbol{v}_d - \boldsymbol{v}_g}{t_s} - \Omega_{\rm K}^2 \boldsymbol{R}, \tag{1.4}$$

$$\frac{d\boldsymbol{v}_g}{dt} = -\frac{\rho_d}{\rho_g}\frac{\boldsymbol{v}_g - \boldsymbol{v}_d}{t_s} - \Omega_{\rm K}^2 \boldsymbol{R} - \frac{1}{\rho_g}\nabla P, \tag{1.5}$$

where $\boldsymbol{v}_d$ is the velocity of dust grains, $\boldsymbol{v}_g$ the velocity of disk gas, $\Omega_{\rm K}$ the Keplerian frequency, $\boldsymbol{R}$ the position vector, ρ_d the spatial dust density, ρ_g the spatial gas density, and P the gas pressure. Both dust grains and gas fluid have almost Keplerian rotational motion. Thus, we use cylindrical coordinate (R, ϕ, z) and simplify the equations by retaining only the lowest order terms. We obtain the equations of motion of dust grains as (e.g., Nakagawa et al., 1986)

$$\frac{\partial v_{d,r}}{\partial t} = -\frac{v_{d,r} - v_{g,r}}{t_s} + 2\frac{v_{\rm K}(v_{d,\phi} - v_{\rm K})}{R}, \tag{1.6}$$

$$\frac{\partial v_{d,\phi}}{\partial t} = -\frac{v_{d,\phi} - v_{g,\phi}}{t_s} - \frac{1}{2}\frac{v_{\rm K}^2}{R}, \tag{1.7}$$

$$\frac{\partial v_{d,z}}{\partial t} = -\frac{v_{d,z} - v_{g,z}}{t_s} - \Omega_{\rm K}^2 z, \tag{1.8}$$

and for the gas,

$$\frac{\partial v_{g,r}}{\partial t} = -\frac{v_{g,r} - v_{d,r}}{t_s} + 2\frac{v_{\rm K}(v_{g,\phi} - v_{\rm K})}{R} - \frac{1}{\rho_g}\frac{\partial P}{\partial R}, \tag{1.9}$$

$$\frac{\partial v_{g,\phi}}{\partial t} = -\frac{v_{g,\phi} - v_{d,\phi}}{t_s} - \frac{1}{2}\frac{v_{\rm K}^2}{R}, \tag{1.10}$$

$$\frac{\partial v_{g,z}}{\partial t} = -\frac{v_{g,z} - v_{d,z}}{t_s} - \Omega_{\rm K}^2 z - \frac{1}{\rho_g}\frac{\partial P}{\partial z}. \tag{1.11}$$

Hereafter, we remove the subscript d for dust velocity.

Next, we proceed to the structure of the gas in protoplanetary disks. In the vertical direction, disk gas is thought to reach hydrostatic balance. The density distribution in the vertical direction is obtained by considering steady state in Eq.(1.11) and the temperature is isothermal in the vertical direction, which is

$$\rho_{\rm g} = \frac{\Sigma_{\rm g}}{\sqrt{\pi} h_g} \exp[-(z/h_g)^2]. \tag{1.12}$$

$h_g \sim c_s/\Omega_K$ is the gas scale height, where c_s is the sound speed of the gas.

In the same manner, we obtain the radial motion of the gas. The disk gas is rotating around the central star with almost the Keplerian speed. Due to the pressure gradient, however, the rotational velocity of gas $v_{{\rm g},\phi}$ is slightly less than the Keplerian speed $v_{\rm K}$. From Eq.(1.10), the radial force balance of the gas can be written as

$$\frac{v_{{\rm g},\phi}^2}{R} = \frac{v_{\rm K}^2}{R} + \frac{1}{\rho_{\rm g}}\frac{dP}{dR}. \tag{1.13}$$

Integrating the equation in z direction and substituting the surface density and temperature distribution, we obtain

$$v_{g,\phi} \equiv v_{\rm K}(1-\eta) \simeq v_{\rm K}\left(1 - \frac{1}{2}\frac{c_s^2}{v_{\rm K}^2}\frac{R}{\Sigma_g}\frac{d\Sigma_g}{dR}\right), \tag{1.14}$$

where we introduce a dimensionless parameter η, which represents the sub-Keplerian motion. Here, we assume that $\eta \ll 1$. η can be rewritten as $\eta = (p/2)(h/R)^2$, which means that η corresponds to the square of the aspect ratio of the disk. The value of η is only ~ 0.004, for example. In spite of this small value, this motion greatly affects the motion of dust grain, which will be discussed later.

1.1.4 The radial drift barreir

Next, we proceed to the radial motion of dust grains. As discussed earlier, the disk gas rotates around the central star with sub-Keplerian speed. This is because the gas feels the pressure. By contrast, dust grains do not feel such pressure, and thus they rotate with the Keplerian speed if there is no gas. This velocity difference between dust grains and the disk gas decelerates the dust grains. As a result, dust grains radially migrate onto the central star. From Eq.(1.6) and Eq.(1.14), the radial drift velocity is given by

$$v_r = \frac{{\rm St}^{-1}v_{g,r} - \eta v_{\rm K}}{{\rm St} + {\rm St}^{-1}}. \tag{1.15}$$

Figure 1.3 shows the radial drift timescale, which is the orbital radius divided by the radial drift speed (e.g., Adachi et al., 1976). We assume that the MMSN model at 5 AU. When dust grains are small enough or large enough, the drifting timescale is longer than the disk dispersal timescale, which is an order of 10^6 years. However, the minimum drifting timescale of particles where St= 1 is $\sim$ 1000 years. This timescale is much less than the disk dispersal timescale, which is $\sim 10^6$ years. Therefore, in the coagulation process, dust grains have a size where they migrate onto the central star.

Next, to estimate the dust growth timescale, we briefly summarize the source of velocity differences in protoplanetary disks. Dust grains have thermal velocity. The Brownian motion induces collisions of dust grains. The Brownian-motion-induced velocity is given by

$$\Delta v_B = \sqrt{\frac{8(m_1+m_2)k_BT}{\pi m_1 m_2}}, \tag{1.16}$$

where m_1 and m_2 represent the masses of colliding two dust grains (e.g., Weidenschilling,

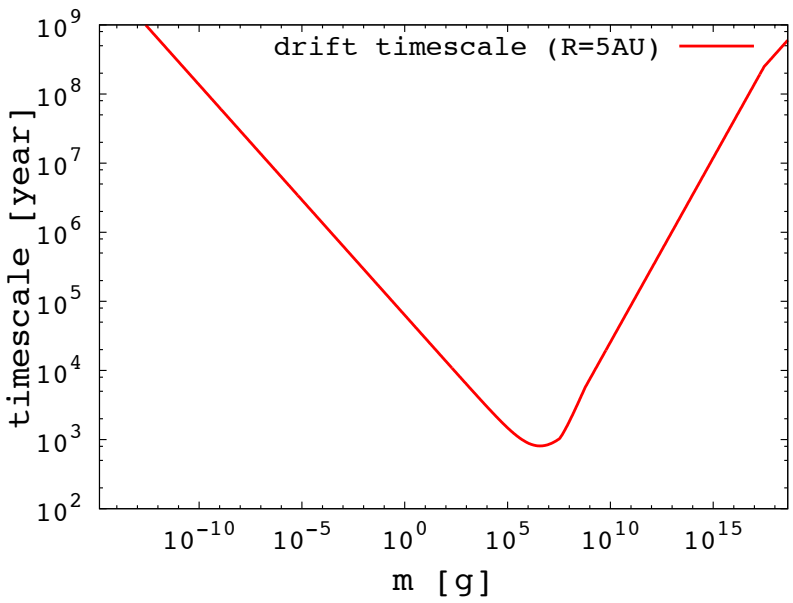

Fig. 1.3 The radial drift timescale against solid mass at 5AU in the MMSN model. The shortest timescale corresponds to St $\sim$ 1.

1977).

The differential motions in radial and azimuthal direction are given by $\Delta v_r = v_r(\mathrm{St}_1) - v_r(\mathrm{St}_2)$ and $\Delta v_\phi = v_\phi(\mathrm{St}_1) - v_\phi(\mathrm{St}_2)$, where St_1 and St_2 represent the Stokes numbers of colliding dust grains, respectively. The azimuthal velocity of dust grains against the disk gas v_ϕ is given from Eq. (1.15) as

$$v_\phi = -\frac{\eta v_\mathrm{K}}{1+\mathrm{St}^2} \tag{1.17}$$

The differential settling velocity $\Delta v_z = v_z(\mathrm{St}_1) - v_z(\mathrm{St}_2)$ is given from Eq. (1.8) and Eq. (1.11) by

$$v_z = -\frac{\mathrm{St}}{1+\mathrm{St}}\Omega_\mathrm{K} z, \tag{1.18}$$

where z is the vertical height from the midplane.

The dust grains are also stirred by gas turbulence. The gas turbulent motion is well modeled by Ormel & Cuzzi (2007). The relative velocity between dust grains that have the

Stokes numbers St_1 and St_2 due to the gas turbulence is given by

$$\Delta v_t = \begin{cases} \delta v_g \mathrm{Re}_t^{1/4} \Omega_\mathrm{K} & (t_{s,1} \ll t_\eta) \\ C_t \delta v_g \sqrt{\mathrm{St}_1} & (t_\eta \ll t_{s.1} \ll \Omega_\mathrm{K}^{-1}) \\ \delta v_g \left(\frac{1}{1+\mathrm{St}_1} + \frac{1}{1+\mathrm{St}_2} \right)^{1/2} & (1 \ll \mathrm{St}) \end{cases} \tag{1.19}$$

where Re_t is the turbulent Reynolds number, t_η the turnover time of the smallest eddies and C_t a numerical factor of order of unity (see also Okuzumi et al. 2012).

Here, let us discuss the timescales of dust growth and radial drift. The drift timescale is defined as

$$t_\mathrm{drift} \equiv \frac{R}{v_r}. \tag{1.20}$$

The growth timescale is also defined as

$$t_\mathrm{growth} \equiv \frac{m}{\dot{m}} = \frac{m}{\rho_d \pi a^2 \Delta v}, \tag{1.21}$$

where Δv is the summation of velocity difference between dust grains and gas. We take $\Delta v = \sqrt{\Delta v_B^2 + \Delta v_r^2 + \Delta v_\phi^2 + \Delta v_t^2 + \Delta v_z^2}$. Figure 1.4 represents the both timescales. When the

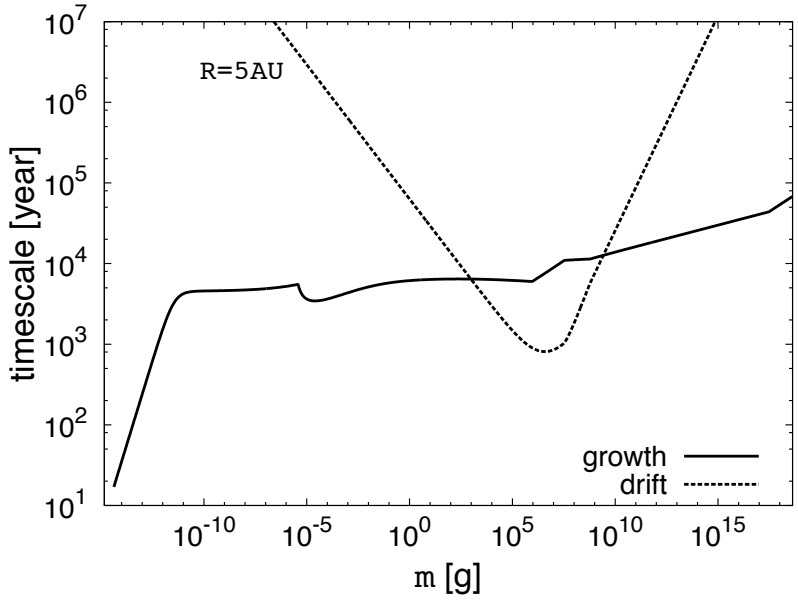

Fig. 1.4 The comparison of timescales between the dust drift and growth.

dust grains are sufficiently small or large, $t_{\rm growth} < t_{\rm drift}$. This means that dust grains can grow before they fall onto the central star. However, when dust grains have their mass of 10^{3-9} g, which correspond to 10 cm to 100 m in dust radius, $t_{\rm growth}$ is larger than $t_{\rm drift}$. In other words, meter-sized solid bodies radially migrate to the central star before they grow to planetesimals. This obstacle to form planetesimals is called the radial drift barrier (Adachi et al., 1976; Weidenschilling, 1977).

In the following, we discuss possibilities to overcome this barrier.

1.1.5 Gravitational instability to form planetesimals

When dust grains coagulate to form mm or cm-sized bodies, dust grains gradually sediment onto the midplane of the disk. The large grains form the thin dust layer, which has been thought to be the birthplace of planetesimals because of gravitational collapse. At Earth orbit, Nakagawa et al. (1981) showed that it takes 3×10^3 years to form the thin dust layer and 5×10^3 years to form planetesimals as a fragments of gravitational instabilities.

However, turbulent motion prevents the formation of thin dust layer. Weidenschilling (1980) pointed out that the dust layer itself causes the turbulence to break the dust layer. When dust grains are dense enough for gravitational instability, the dust spatial density is much higher than that of gas. Because the gas molecules can not freely get into the dust layer, the dust grains rotate with Keplerian speed. On the other hand, the disk gas keeps to rotate with sub-Keplerian speed. Thus, the dust and gas have a shear motion. This motion triggers the Kelvin-Helmholz instability to break the dust layer. The forming condition of planetesimals by gravitational instability has been investigated by several authors (Sekiya, 1998; Youdin & Shu, 2002). Sekiya (1998) suggested that formation of planetesimals by gravitational instability is unlikely but it could be possible if the composition is different from solar composition. Johansen et al. (2007) proposed that locally overdense region of grains can form planetesimals. However, the uncertain points are how to form initial meter-sized bodies and how to prevent the disk turbulence which diffuses the locally over dense regions. In this way, the formation of planetesimals by gravitational instability is still under debate.

1.1.6 Direct coagulation to overcome the radial drift barrier

When the disk turbulence is strong enough, dust grains are stirred up by the disk-gas turbulence. When the dust grains are small enough to couple to the gas, the distribution of dust is the same as the gas. However, if dust size is large, dust grains are decoupled from the gas

and has different distribution from the gas. The coupling efficiency depends on the dust size and mass. Considering the balance between being stirred up by the disk gas and the gravity onto the midplane, the dust grains also has a Gaussian distribution with dust scale height $h_{\rm d}$ (Brauer et al., 2008; Dubrulle et al., 1995; Youdin & Lithwick, 2007). The dust scale height is given by

$$h_{\rm d} = h_{\rm g}\left(1 + \frac{\rm St}{\alpha}\frac{1+2{\rm St}}{1+{\rm St}}\right)^{-1/2}. \tag{1.22}$$

Here, let us estimate the growth timescale. The spatial density of dust grains is estimated to be

$$\rho_d \sim \frac{\Sigma_d}{h_d}. \tag{1.23}$$

If the dominant velocity source of collisions is caused by turbulent motion of the disk gas and the Stokes number is much less than unity, ${\rm St} \ll 1$, the velocity of dust grains is

$$\Delta v_t \sim \sqrt{{\rm St}\,\alpha} c_s. \tag{1.24}$$

Using that $h_d \sim h_g \sqrt{\alpha/{\rm St}} \sim (c_s/\Omega_{\rm K})\sqrt{\alpha/{\rm St}}$, we obtain

$$\Delta v_t \sim {\rm St}\Omega_{\rm K} h_d \tag{1.25}$$

Assuming that the gas drag law is Epstein regime, which is equivalent to $a < \lambda_{\rm mfp}$, we finally obtain the growth timescale as

$$t_{\rm growth} \sim \left(\frac{\Sigma_g}{\Sigma_d}\right)\Omega_{\rm K}^{-1}. \tag{1.26}$$

This equation has a strong conclusion. The growth timescale does not depend on turbulent strength or surface density, but depends on the dust-to-gas mass ratio. On the other hand, the drift timescale can be written as

$$t_{\rm drift} \sim \frac{R}{{\rm St}\,\eta v_{\rm K}}, \tag{1.27}$$

when ${\rm St} < 1$. To overcome the radial drift barrier, we have to reduce $t_{\rm growth}$ less than $t_{\rm drift}$ when ${\rm St} \sim 1$. This happens when the dust-to-gas mass ratio is higher.

Brauer et al. (2008) used numerical simulations of dust coagulation and suggested that if the initial dust-to-gas-mass ratio is higher than the interstellar medium, dust grains can grow to planetesimals. This is due to the growth timescale depends on the dust-to-gas-mass ratio.

Another possibility is to consider the case that the gas drag law changes from Epstein to

Stokes regime. In the discussion above, we assume that the grain radius is much less than the mean free path of gas. The assumption is valid if we consider dust grains have the same internal density as the material density. However, if dust grains form aggregates and their effective radius becomes larger than the mean free path, the situation changes. If we assume the Stokes regime as a gas drag law, the growth timescale is given by

$$t_{\rm growth} \sim \frac{\lambda_{\rm mfp}}{a}\left(\frac{\Sigma_g}{\Sigma_d}\right)\Omega_{\rm K}^{-1}. \tag{1.28}$$

This equation suggests that a large radius causes a rapid growth of dust aggregates and it may overcome the radial drift barrier.

Okuzumi et al. (2012) considered the growth of porous dust aggregates based on numerical modeling of dust aggregates. When the Stokes number is around unity, the aggregate radius is larger than the mean free path of the gas, and thus the gas drag law changes from Epstein to Stokes regime. This results in the rapid growth of dust aggregates to overcome the radial drift barrier. In their scenario, however, the dust aggregates are too fluffy compared to planetesimals. We will review the porosity evolution later in this chapter.

In addition, Windmark et al. (2012a) and Drążkowska et al. (2013) suggested that the bouncing behavior can help to form planetesimals. We will also discuss this point later in this chapter.

1.2 Dust microphysics: introducing the fragmentation and bouncing barriers

For simplicity, grains have been considered to be always spherical and to have a constant internal density. In coagulation of dust grains, however, dust grains are no longer grains with an uniform density but construct an aggregated structure. In this section, we review the process of the aggregation of dust grains in astronomical environments.

1.2.1 Fractal growth of aggregates

There are two-limiting cases of dust cluster growth models: particle-cluster aggregation (PCA or BPCA) and cluster-cluster aggregation (CCA or BCCA). BPCA is created by adding each constituent particle from a random direction, while BCCA is made by sticking with the same-sized cluster from a random direction. These clusters are often characterized

by the gyration radius $r_{\rm g}$. The gyration radius is calculated by

$$r_g = \sqrt{\frac{1}{N}\sum_{k=1}^{N}(\boldsymbol{x}_k - \boldsymbol{x})^2}, \tag{1.29}$$

where N is a number of monomers, $\boldsymbol{x}_k$ the position vectors, and $\boldsymbol{x}$ the position of the center of coordinate. The fractal dimension of clusters D_f is defined such that the gyration radius of the clusters and the number of monomers N have a relation of $N \propto r_{\rm g}^{D_f}$ or $D_f \equiv \partial \ln r_g / \partial \ln N$. Mukai et al. (1992) examined the fractal dimension of BPCA and BCCA, and found that $D_f \approx 3$ for BPCA and $D_f \approx 2$ for BCCA. Several authors applied these two limits of clusters

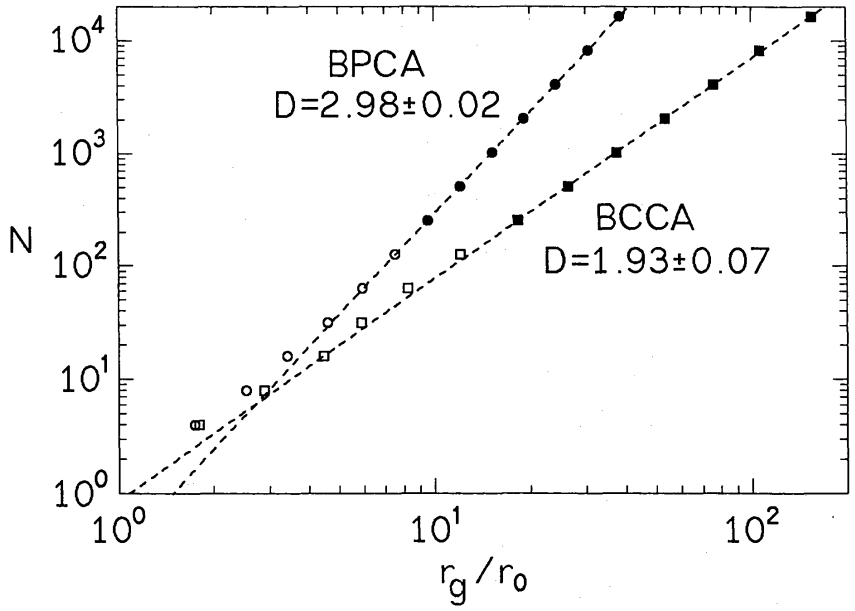

Fig. 1.5 A number of monomers against the normalized gyration radius. Two lines represents the BCCA and BPCA cases. This figure is taken from Fig. 2 of Mukai et al. (1992).

to dust coagulation in the Universe (Blum, 2004; Kempf et al., 1999; Ormel et al., 2007; Ossenkopf, 1993). In planet formation, however, the dominant process depends strongly on the physics of dust coagulation. Dust grains are sticking each other with van der Waals force or some electric force. To determine the structure evolution of dust aggregation, modeling including the sticking force is required.

1.2.2 Monomers in contact

The forces between two micron-sized bodies have an importance on several fields of studies. The basic theory of two elastic bodies in contact was first derived by Hertz. The Hertz theory formulated the displacement of two elastic bodies in contact when external force is exerted. We consider two spherical bodies, which have radii R_1 and R_2, Young's moduli E_1 and E_2, the Poisson ratios ν_1 and ν_2, and the radius of contact surface is a. Figrue 1.6 represents the two-dimensional view of the contact surface of the two monomers in contact. Here, we

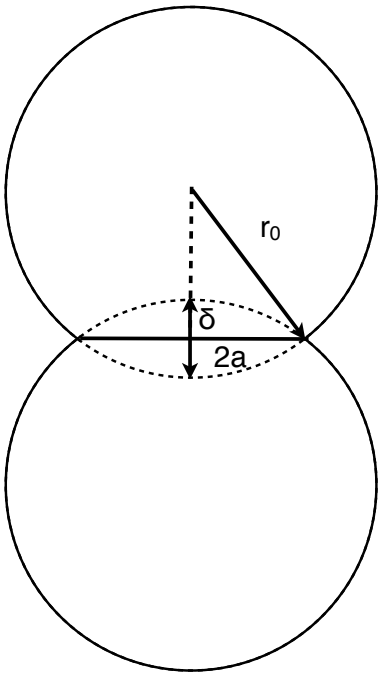

Fig. 1.6 The monomers in contact. The contact surface has a radius a, the monomer has a radius r_0, and the displacement δ.

assume that the two monomers have the same radius and physical properties. The contact surface has a radius a and the monomers has a displacement δ. The monomer radius r_0, the displacement δ, and the radius of the contact surface a have a relation of

$$(r_0 - \delta/2)^2 + a^2 = r_0^2. \tag{1.30}$$

Assuming that $\delta \ll r_0$,

$$a = \sqrt{r_0 \delta}. \tag{1.31}$$

By Hooke's theory, the repulsive force of the elastic body is given by a description

with the Young's modulus and the displacement. Applying the Hooke's theory to a volume including the contact surface, when the force is exerted, the force F and the displacement δ has a relation of

$$\frac{\delta}{a} \sim \frac{F}{Ea^2}. \tag{1.32}$$

Using Eq. (1.31) and Eq. (1.32), we obtain

$$F = \frac{4E^* R^{1/2}}{3}\delta^{3/2}, \tag{1.33}$$

where $R = R_1R_2/(R_1+R_2)$ and $E^* = ((1-\nu_1)^2/E_1 + (1-\nu_2)^2/E_2)^{-1}$. See Dominik & Tielens (1997) for the derivation of the factor.

When the two bodies have an attractive force, whose surface energy is γ, it can balance with the repulsive force. Johnson et al. (1971) expand the Hertz theory with the adhesion force, with the surface energy γ (hereafter, JKR theory). The binding energy is given by

$$U_s = -2\pi a^2 \gamma \tag{1.34}$$

Thus, the adhesion force is given by

$$F_s = \frac{dU_s}{d\delta} = -2\pi\gamma R. \tag{1.35}$$

The repulsive force and the adhesion force can balance with a certain contact radius. We represent the contact radius and the displacement in the equilibrium with $a = a_0$ and $\delta = \delta_0$. Using the Eqs. (1.33) and (1.35), the equilibrium contact radius is given by

$$a_0 = \left(\frac{9\pi\gamma R^2}{2E^*}\right)^{1/3}. \tag{1.36}$$

At the equilibrium, the displacement δ is $\delta_0 = a_0^2/(3R)$ (see Dominik & Tielens, 1997, for the derivation of the factor). The pull-off force required to separate the two monomers is derived as $F_c = 3\pi\gamma R$. At the moment of separation, $\delta \equiv \delta_c = (9/16)^{1/3}\delta_0$. The JKR theory gives the basic understanding of the interaction between astronomical grains.

Here, we revisit some important quantities to consider the interaction of monomers. Chokshi et al. (1993) derived the kinetic collisional energy below which the two grains can stick each other. The critical energy is given by

$$E_{\rm stick} = 0.4 \times F_c\delta_c \approx 9.6 \times \frac{\gamma^{5/3}R^{4/3}}{E^*}. \tag{1.37}$$

Once the two monomers stick together, larger energy is required to separate these two monomers. The total energy required to break the contact is given by

$$E_{\rm break} = 1.8 \times F_c \delta_c \approx 43 \times \frac{\gamma^{5/3} R^{4/3}}{E^*}. \tag{1.38}$$

In addition, two monomers in contact can have a tangential force. Using the JKR theory, Dominik & Tielens (1997) and their collaborators (Chokshi et al., 1993; Dominik & Tielens, 1995) formulated the interaction between two spherical elastic bodies with adhesion force. Their formulation provides us a basic physics between astronomical grains.

The relative motion between monomers in contact has 4 degrees of freedom. Figure 1.7 illustrates the 4 degrees of freedom. There is one in normal direction, two in rolling and sliding motion, and the other for twisting motion.

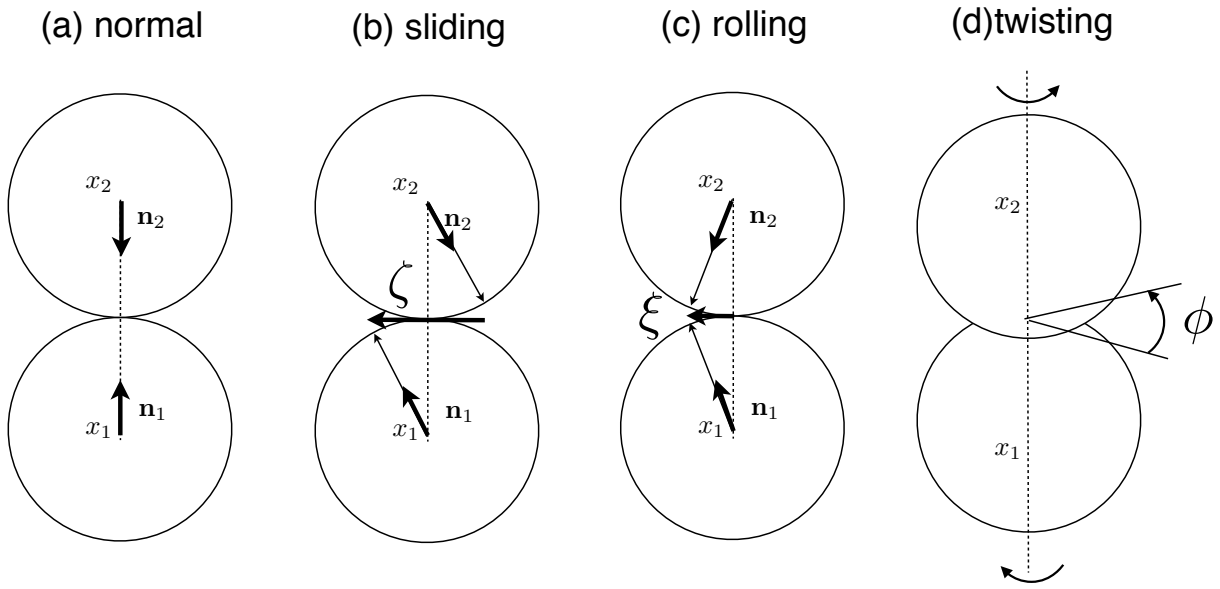

Fig. 1.7 Geometry of the four modes of deformation between two monomers in contact (Wada et al., 2007). x_1 and x_2 are the position vectors of the monomers. $\boldsymbol{n}_1$ and $\boldsymbol{n}_2$ are the normal vectors in the direction to the other monomer before deformation. ζ and ξ are the displacements of sliding and rolling motions and ϕ is the displacement degree in twisting motion.

Here, we focus on the rolling motion, which is represented in Fig. 1.7(b). For small motions around the contact area, the monomers make deformation. This leads to asymmetric pressure to produce a friction force against the tangential motion. The resultant torque is

given by

$$M = 4F_{\rm c}\left(\frac{a}{a_0}\right)^{3/2}\xi, \tag{1.39}$$

where ξ is the linear displacement on the contact area (see Dominik & Tielens, 1995, for derivation).

For a small motion, the energy does not dissipate. However, the particles are made up of molecules, and thus the surface is not totally smooth. When a particle makes tangential motion on the contact surface, it feels a friction force because of the roughness. Figure 1.8 represents the rolling motion of the monomers in contact. When the two particles roll

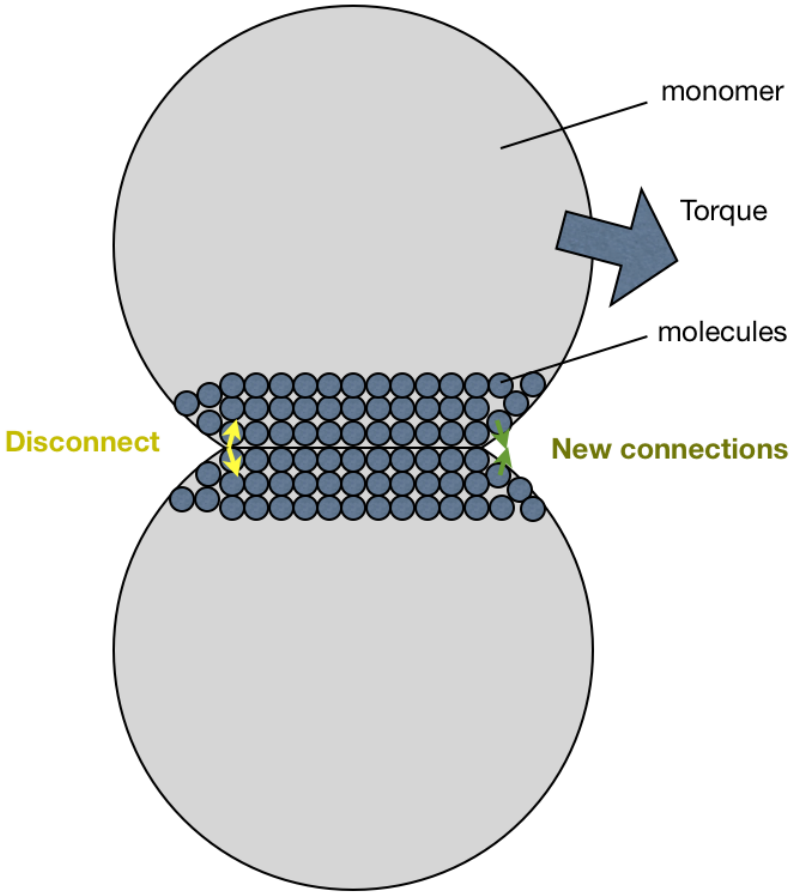

Fig. 1.8 Schematic drawing to illustrate the microscopic view of the rolling friction.

over each other, new contacts are made at the leading edge and some contacts are lost at the trailing edge. The critical displacement where the new contacts are made is defined as $\xi_{\rm crit}$.

The required torque to start rolling motion is

$$M_{\rm crit} = 4F_{\rm c}\left(\frac{a}{a_0}\right)^{3/2}\xi_{\rm crit}. \tag{1.40}$$

The restored energy is given by $M_{\rm crit}(\xi_{crit}/2R)$ where $(\xi_{crit}/2R)$ is the rotational degree in radian. The factor (a/a_0) does not change seriously in the deformation, and thus we assume that the factor is unity. Thus, the required energy to start rolling motion is then

$$e_{\rm roll} = 4F_c\xi_{\rm crit}\frac{\xi_{\rm crit}}{2R} = 6\pi\gamma\xi_{\rm crit}^2. \tag{1.41}$$

The rolling energy $E_{\rm roll}$, which is the energy required to roll 90 degrees, is derived by calculating the energy to rotate the length of πR,

$$E_{\rm roll} = 12\pi^2\gamma R\xi_{\rm crit} \tag{1.42}$$

This energy is useful for later discussions.

1.2.3 Basic equations for numerical simulations

Based on the concept of Dominik & Tielens (1997), Wada et al. (2007) formulated the basic equations of numerical simulations of dust aggregates. Here, we follow Wada et al. (2007) to introduce the basic equations.

They introduced the normal and tangential forces using a potential energy for each case. The potential energy for normal motion is given by

$$U_{\rm n} = 4\times 6^{1/3}\left(\frac{4}{5}\left(\frac{a}{a_0}\right)^5 - \frac{4}{3}\left(\frac{a}{a_0}\right)^{7/2} + \frac{1}{3}\left(\frac{a}{a_0}\right)^2\right)F_{\rm c}\delta_{\rm c}. \tag{1.43}$$

Using the potential energy, the force acting on the particle 1 due to the contact with the particle 2 is given by

$$\boldsymbol{F}_{n,1} = -\frac{\partial U_n}{\partial \boldsymbol{x}_1}. \tag{1.44}$$

Figure 1.7 shows the schematic illustration of the normal and tangential motions. In the same manner as discussed above, the sliding, rolling, and twisting potential energies are given by

$$U_{\rm s} = \frac{1}{2}k_s|\zeta|^2, \tag{1.45}$$

$$U_{\rm r} = \frac{1}{2} k_r |\xi|^2, \tag{1.46}$$

$$U_{\rm t} = \frac{1}{2} k_t |\phi|^2, \tag{1.47}$$

where ζ and ξ are the displacements of sliding and rolling motions and ϕ is the displacement degree in twisting motion represented in Figure 1.7. The spring constants k_s, k_r, k_t are given by

$$k_s = 8 a_0 G^*, \tag{1.48}$$

$$k_r = \frac{4F_c}{R}, \tag{1.49}$$

$$k_t = \frac{16}{3} G^* a_0^3, \tag{1.50}$$

where $G^* = (2-\nu_1)/G_1 - (2-\nu_2)/G_2$ and G_1 and G_2 are the shear moduli of each monomer.

When the tangential motion of the particles exceeds some critical points, the motion does not obey the above equations of the elastic regime, but of the inelastic regime. We discussed this point for the rolling motion in the previous section. In the formulations of Wada et al. (2007), the force is treated as continuos friction. The critical displacements of each force are given by

$$\zeta_{\rm crit} = \frac{2-\nu}{16} a_0. \tag{1.51}$$

$$\phi_{\rm crit} = \frac{1}{16\pi}. \tag{1.52}$$

The displacement $\xi_{\rm crit}$ is a free parameter, which is related to the surface roughness of the molecules, and thus it is expected to have an order of ~ 1 Å. Dominik & Tielens (1995) set it to be 2 Å, although Heim et al. (1999) suggested $\xi_{\rm crit} = 32$ Å from their laboratory experiments of silica particles. We note that the critical displacement of the rolling motion is still under debate.

Dust grains in protoplanetary disks are believed to be composed of mixture of ice, silicate, organics, and some other materials. Due to the difficulties to reproduce the dust grains in protoplanetary disks, laboratory experiments usually have used silica (SiO_2) particles. Heim et al. (1999) experimentally confirmed the linear relation between the particle radius and the pull-off force, expected from JKR theory as shown in Figure 1.9. They also measured the rolling friction and obtained the critical displacement $\xi_{\rm crit} = 32$ Å. This value is

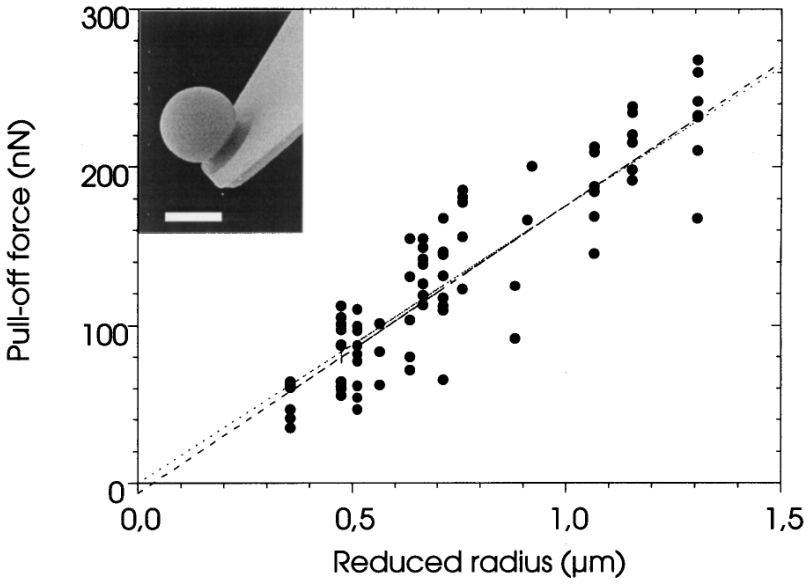

Fig. 1.9 The laboratory experiment performed by Heim et al. (1999). The pull-off force versus the reduced radius of the monomers.

one order of magnitude higher than the theoretically expected value, $\xi_{\rm crit} = 2$ Å (Dominik & Tielens, 1995).

1.2.4 The fragmentation behavior

Dust grains can be disrupted by high-speed collisions. Blum & Münch (1993) performed experiments on dust collisions of silica particles and the critical velocity for the disruption is a few m/s. This is significantly lower than the typical collisional velocity in protoplanetary disks, which is a few tens of m/s. Therefore, dust grains are disrupted before forming larger bodies. This is called the fragmentation barrier. The critical velocity for the fragmentation has been discussed both by numerical simulations and laboratory experiments.

Dominik & Tielens (1997) performed a series of two dimensional numerical simulations of colliding aggregates of monomers. As a result, they formulated a recipe of collisions of aggregates as follows. When the effective kinetic energy is below $5E_{\rm roll}$, the results are sticking or bouncing without visible restructuring of the aggregates.. When $E_{\rm eff} > 5E_{\rm roll}$, by contrast, some visible restructuring occurs. Finally, when $E_{\rm eff} > E_{\rm break}$, the outcome of the collision becomes catastrophic disruption. The results are often quoted as DT recipe, which is summarized in Table 1.1.

The formulation is revisited by Wada et al. (2007) as described above. The reformu-

Table 1.1 DT recipe

Energy	Collisional Outcome
$E_{\rm imp} \approx 5E_{\rm roll}$	First visible restructuring
$E_{\rm imp} \approx n_k E_{\rm roll}$	Maximum compression
$E_{\rm imp} \approx 3n_k E_{\rm break}$	Loss of one particle
$E_{\rm imp} > 10n_k E_{\rm break}$	Catastrophic distruption

lation enables heavier numerical simulations of collisions of aggregates because the introduction of the potential energies ensure the energy conservation in the case of no dissipation. Although Dominik & Tielens (1997) performed numerical simulations with roughly 40 particles, Wada et al. (2007) did it with ∼2000 particles. In addition, Wada et al. (2008) performed 3D numerical simulations with BCCA clusters composed of ∼4000 particles. They confirmed that the criteria that was proposed by Dominik & Tielens (1997) is consistent with their 2D and 3D simulations. We discuss the results of numerical simulations on porosity evolution in Sec. 1.3.

Collisions of dust aggregates have also been investigated by laboratory experiments. If a particle or an aggregate hit another with some speed higher than a critical velocity, they are disrupted. Poppe et al. (2000) performed laboratory experiments and suggested that maximum velocity that two aggregates stick is one order of magnitude higher than the results of previous theoretical work (Chokshi et al., 1993; Dominik & Tielens, 1997). They suggested that the deviation is explored by the fact that the previous theoretical work had assumed a smooth surface and ignored a small roughness.

Although silica particles have been used in laboratory experiments, some theoretical studies of aggregate collisions (Dominik & Tielens, 1997; Wada et al., 2007, 2008) have shown that icy aggregates can grow through their mutual collisions when the collisional velocity is less than ~ 30 m s^{-1} in the cases of head-on collisions. Paszun & Dominik (2006) pointed out the importance of the off-set collisions, and Wada et al. (2009) studied the criteria of the net growth including the cases of off-set collisions. The net growth is defined as the target aggregate gain some amount of mass through the collisional event. As a result, they derive the critical velocity for net growth as $v = 50$ m s^{-1} for ice and $v = 6$ m s^{-1} for SiO_2. More recently, Wada et al. (2013) have included the high mass ratio collisions, and they derived the critical velocities as

$$v_{\rm crit} = 80 \times \left(\frac{r_0}{0.1\ \mu{\rm m}} \right)^{-5/6} {\rm m\ s^{-1}\ for\ ice}, \tag{1.53}$$

and

$$v_{\rm crit} = 8 \times \left(\frac{r_0}{0.1\ \mu{\rm m}} \right)^{-5/6} {\rm m\ s^{-1}} \text{ for silicate,} \tag{1.54}$$

where r_0 represents the monomer radius. Therefore, icy aggregates are candidates to overcome the fragmentation barrier.

1.2.5 Bouncing behavior

Laboratory experiments have shown that collisions of dust aggregates sometimes lead to bouncing. Güttler et al. (2010) pointed out that if the colliding speed is too low to be disrupted and too high for sticking, the two aggregates bounce. The bouncing has been reproduced in several laboratory experiments (Blum & Münch, 1993; Weidling et al., 2012). Zsom et al. (2010) introduced the bouncing barrier in planet formation theory and claimed that the steady-state size distribution is achieved by bouncing barrier. More recently, Windmark et al. (2012a,b) showed that the bouncing barrier can be avoided by introducing a little amount of large bodies or by considering a high velocity tail in Maxwellian velocity distribution.

By contrast, the bouncing behavior was first reproduced in numerical simulations by Wada et al. (2011). They pointed that the bouncing behavior is reproduced when the coordinate number is 6 or more. This critical number corresponds to the filling factor of 0.3. Thus, the bouncing barrier is not a problem when the filling factor is lower than ~ 0.3. Therefore, if we consider fluffy dust aggregates, the bouncing is no longer a problem in planetesimal formation.

1.3 Porosity evolution of dust aggregates

Using the basic physics of dust interaction, the porosity (or volume) evolution has been investigated by numerical simulations, and also by laboratory experiments. With low-speed collisions, dust grains stick and no restructuring can occur. The very first stage of dust coagulation leads the aggregates to be very fluffy because of the low-speed collisions. The aggregation leads to very open structure with fractal dimension of $D_f = 1 - 2$. Laboratory experiments have confirmed the open structure as shown in Figure 1.10 (Wurm & Blum, 1998). The construction of BCCA structure has also been confirmed by numerical simulations (Okuzumi et al., 2009; Suyama et al., 2008; Wada et al., 2007, 2008).

The next step of the dust coagulation is compression. Aggregate collisions have shown

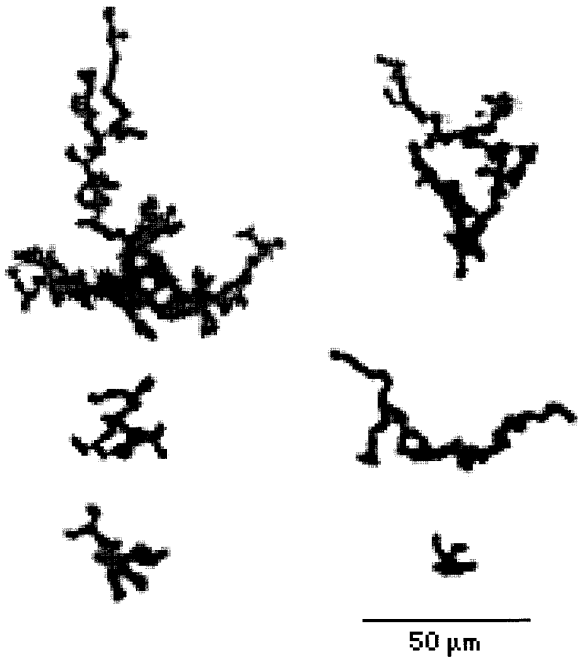

Fig. 1.10 Dust aggregates observed in laboratory experiments by Wurm & Blum (1998). The monomers are SiO_2 particles with 1.9 μm diameter.

to be not effective to compress the fluffy dust aggregates. Ormel et al. (2007) performed the pioneering work on porosity evolution in protoplanetary disks. They used BPCA and BCCA limits and interpolation between them. In their interpolation, the compressed aggregates assumed to be have a fractal dimension of 3. However, Okuzumi et al. (2009) performed numerical simulations of aggregate collisions with various mass ratios and have shown that the Ormel model does not reproduce the porosity evolution. They have shown that collisions of similar size aggregates lead them to have fractal dimension around 2.

About the collisional compression, Wada et al. (2008) and Suyama et al. (2008) found that the aggregates which are compressed by collisions have a fractal dimension of 2.5. Figure 1.11 shows the results of internal density evolution of dust aggregates with constant collisional velocity. Because they stick to the same-sized cluster, the initial density evolution is on the line of BCCA (dashed line). At a critical point, the density evolution deviates from the BCCA line because of the collisional compression. However, the fractal dimension of compression is 2.5, which is inefficient to compress the aggregates. This means that the collisional compression is not as effective as expected in Ormel et al. (2007). Suyama et al. (2008, 2012) investigated the porosity evolution through collisions, and confirmed that collisions hardly compress the aggregates.

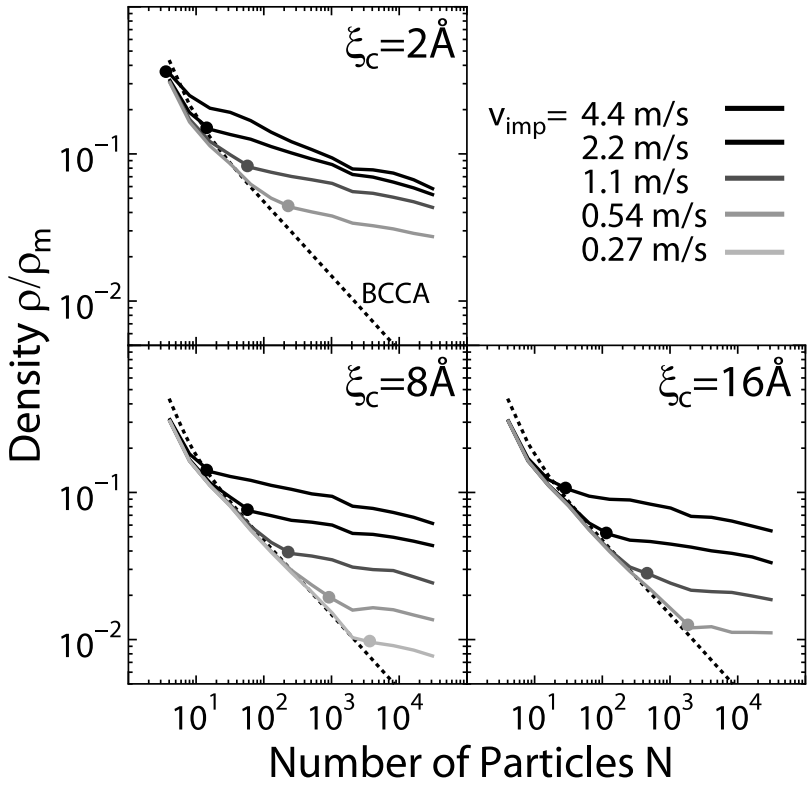

Fig. 1.11 The internal density or the filling factor evolution of sequential growth of dust aggregates with a constant collision speed by Suyama et al. (2008). The critical displacement is ranging in $\xi_c = 2, 8, 16$ Å.

Using the porosity evolution model depending on mass ratio (Okuzumi, 2009) and the compression model investigated by Suyama et al. (2008, 2012), Okuzumi et al. (2012) includes the collisional compression model to perform coagulation simulations in a protoplanetary disk. Figure 1.12 shows that the porosity evolution of dust aggregates at 5 AU in protoplanetary disks. As a result, the coagulation and collisional compression process has

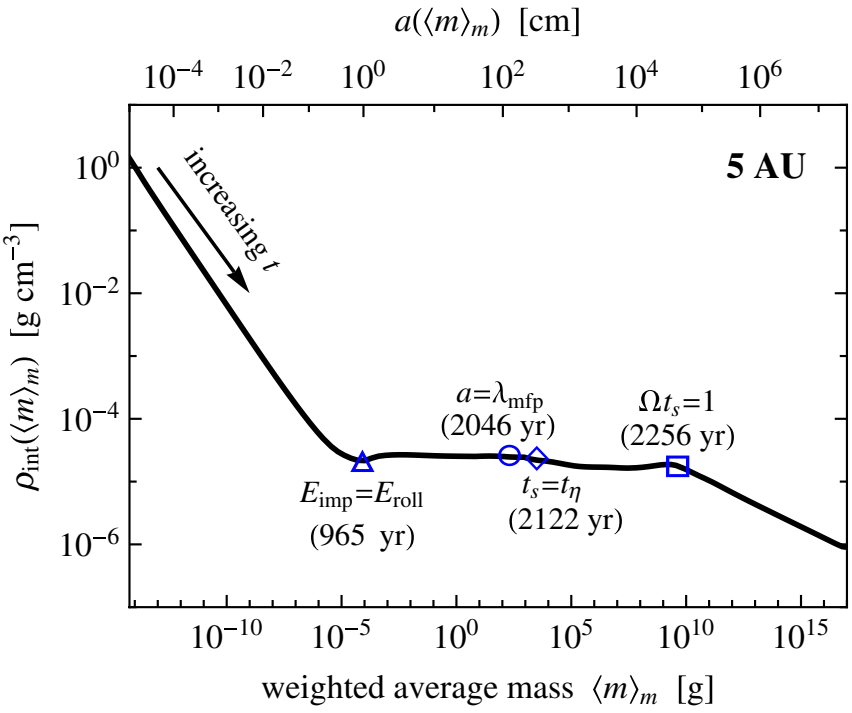

Fig. 1.12 The internal density evolution of dust aggregates at 5 AU in orbital radius (Okuzumi et al., 2012).

been revealed as follows. The initial growth is fractal, and the fractal dimension is approximately equal to 2. This means that initial growth is dominated by collisions of similar size clusters and thus they form BCCA-like aggregates. Next, when the impact energy exceeds the critical energy, which is $E_{\rm roll}$ in this case, the collisional compression becomes effective. Combining the facts that the fractal dimension of the collisional compression is 2.5 and the relative velocity depends on the Stokes number, the internal density keeps constant during the collisional compression regime. The filling factor is as low as 10^{-5}, which is not consistent with planetesimals, which are believed to have a high density, ~ 1 g cm^{-3}. This result has a strong conclusion: once dust aggregates get high porosity, collisional compression is insufficient to compress the aggregates.

Therefore, one of the purposes of this paper is to find a way of the density evolution

toward the compact planetesimals by introducing some kinds of compression mechanisms other than collisions.

1.4 Dust growth evidenced by astronomical observations

In this section, we will briefly review the observational results of protoplanetary disks, especially focusing on grain growth.

1.4.1 Dust opacity

Dust opacity depends on their grain size and composition. In the interstellar medium, dust grains are believed to have power-law size distribution with a^{-p} and p=3.5, where a is grain radius. The maximum radius is thought to be sub-micron size (Mathis et al., 1977). In protoplanetary disks, by contrast, dust grains are thought to be larger than the ISM. Thus, the dependence of dust opacity on thier size is essential to understand the emission from protoplanetary disks.

The size dependence has been studied by Miyake & Nakagawa (1993). They used Mie theory to calculate the optical properties of spherical dust grains. Figure 1.13 shows the opacities of dust grains with size distribution with $p = 3.5$ and different maximum radius. They found that the opacity decreases with increasing maximum grain radius at short wavelengths. Also, the slope of the opacity at long wavelengths changes to be flatter with increasing maximum grain radius.

D'Alessio et al. (2001) also investigated the size and compositional dependence, such as with and without ice particles in order to reproduce the observed SEDs of protoplanetary disks. They found that many general features of protoplanetary disks can be explained with disk models with power-law size distributions of grains with $p \sim 2.5 - 3.5$, and maximum radius of $a_{\max} \sim 1$ mm. This suggests that the size distribution of dust grains in protoplanetary disks are completely different from the ISM, where $p \sim 3.5$ and the maximum size is sub-micron size.

1.4.2 Observations of protoplanetary disks

Pre-main sequence stars often possess circumstellar disks around themselves. IRAS satellite have detected infrared excesses on pre-main sequence stars (Rucinski, 1985). These infrared excesses have been interpreted as emission from disks (Adams et al., 1987; Calvet et al., 1991; Kenyon & Hartmann, 1987). On the other hand, Beckwith & Sargent (1991);

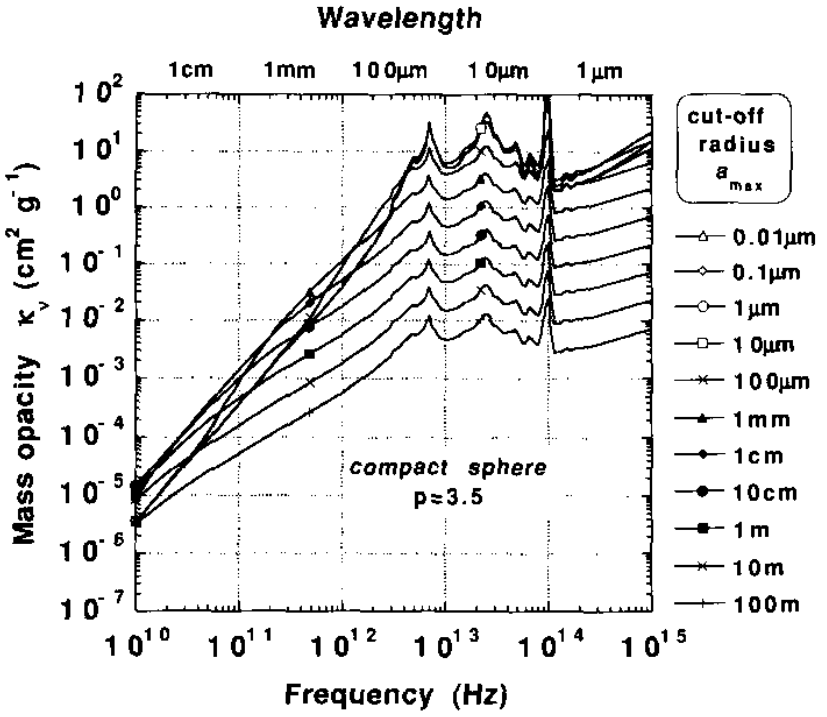

Fig. 1.13 The absorption mass opacity of dust grains per gram of gas (Miyake & Nakagawa, 1993). The different lines represent the different maximum grain radius. The size distribution is assumed to have a power of −3.5.

Beckwith et al. (1990) performed continuum observations at 1.3 mm wavelengths of pre-main sequence stars. Circumstellar disks are thought to be optically thin at 1 mm, thus they brought a great insight onto dust grains in disks. Combining the multi-wavelength data, the overall evolution of protoplanetary disks has been revealed.

Focusing on grain growth, we pick up the millimeter-wave observations of protoplanetary disks. Figure 1.14 is the typical spectral energy distribution of protoplanetary disks. Beckwith et al. (1990) derived spectral indices of some circumstellar disks. The spectral

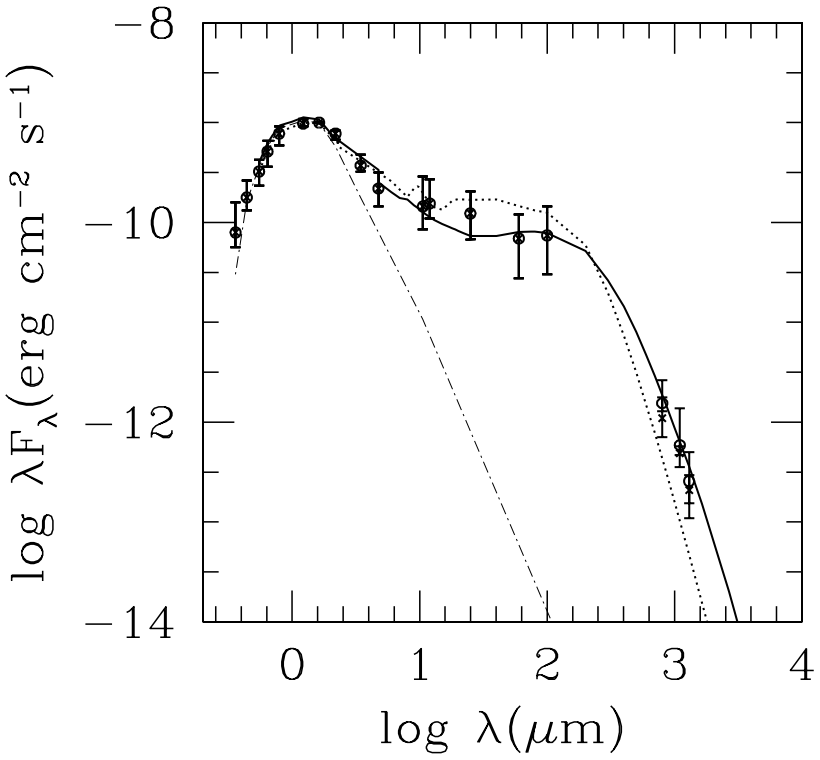

Fig. 1.14 The median SED of T Tauri stars with disks. The figure is taken from D'Alessio et al. (2001).

index α such that $F_\nu \propto \nu^\alpha$ between at 1.3 mm and 2.7 mm in wavelengths is significantly lower than the interstellar medium, where $\alpha \sim 2$ (e.g., Schwartz, 1982). Note that the spectral index α is related to the opacity slope β with $\beta = \alpha - 2$ if the medium is optically thin.

The spectrum at millimeter wavelengths is strongly affected by grain size. As already discussed, D'Alessio et al. (2001) showed that the maximum grains size should be larger than 1 mm at least to explain the observed spectral index. Figure 1.15 shows the spectral index as a function of the maximum size of grain radius. To explain the low spectral index, the maximum grain size should be larger than 1 mm.

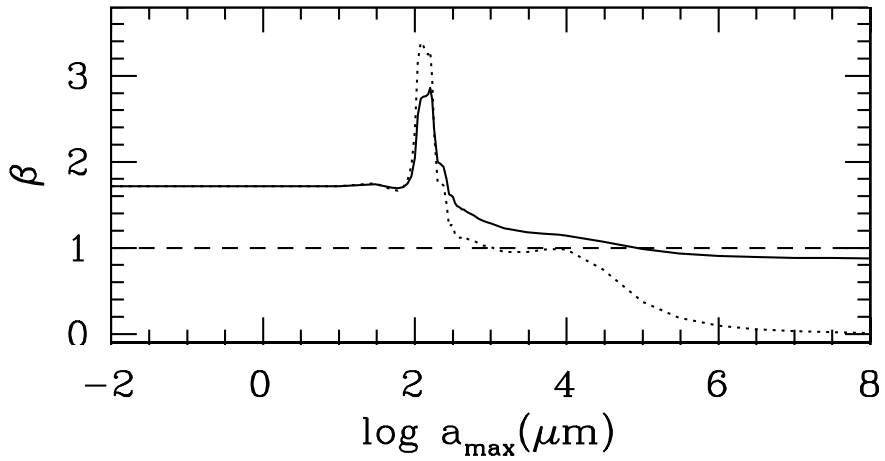

Fig. 1.15 The opacity index β between 0.769 and 1.3 mm wavelengths. The figure is originally from Fig.3 of D'Alessio et al. (2001).

More recently, radio interferometer observations resolved protoplanetary disks. Andrews & Williams (2005) compiled millimeter observations toward Taurus-Auriga region and derived disk properties. The spectral index is derived to be $\alpha = 2.0 \pm 0.5$. This is a strong evidence of grain growth. Figure 1.16 shows the summary of previous work on obtaining the spectral index. Many authors have observed to derive the spectral index and proven that $\alpha = 2.0 - 3.0$ (Andrews & Williams, 2007; Guilloteau et al., 2011; Isella et al., 2009; Ricci et al., 2010a,b), which corresponds to opacity index is $\beta = 1.0 - 2.0$ at millimeter wavelengths.

In addition, some observations have revealed radial profiles of dust-grain size. Isella et al. (2010) and Pérez et al. (2012) have analyzed the radial profile of the spectral index α. Their best fit model of Pérez et al. (2012) has shown that the maximum grain size monotonically increases in outer region of the disks with the distance from the central star as shown in Figure 1.17.

1.4.3 Theoretical explanation of low β

Although many observations protoplanetary disks suggest that dust grains grow to 1 mm-sized grains at least, holding millimeter-sized dust grains in the outer part of the protoplanetary disks is theoretically challenging. Because the timescale of radial drift is shorter than the growth timescale in the outer region of protoplanetary disks, millimeter-sized dust grains quickly fall onto the central star. This is the same mechanisms as the radial drift barrier. Due to the coupling efficiency of dust grains and disk gas depends on orbital radius, the most de-

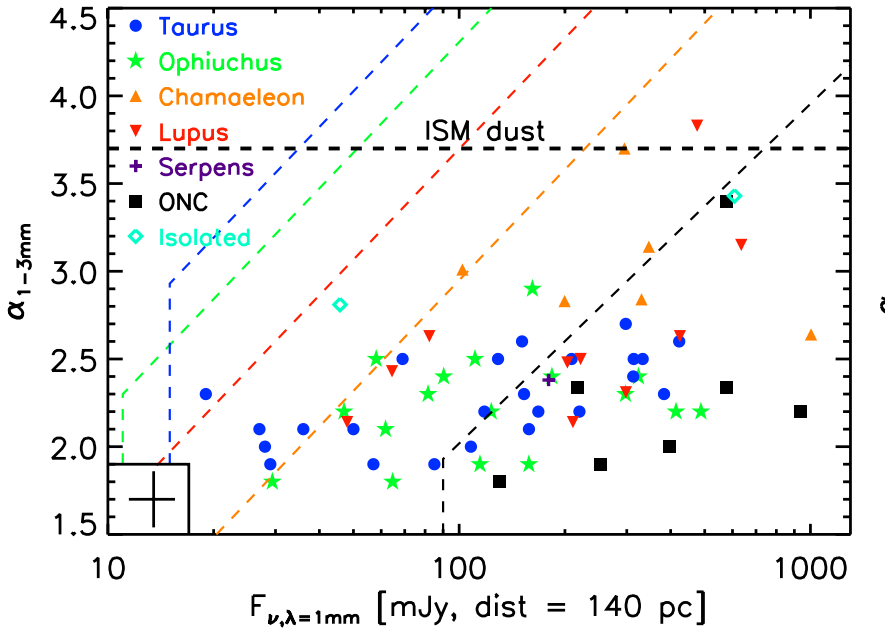

Fig. 1.16 Spectral index β between 1.1 and 3 mm plotted against the flux at 1.1 mm for disks around single stars, which is scaled for a common distance of 140 pc (Testi et al. 2014).

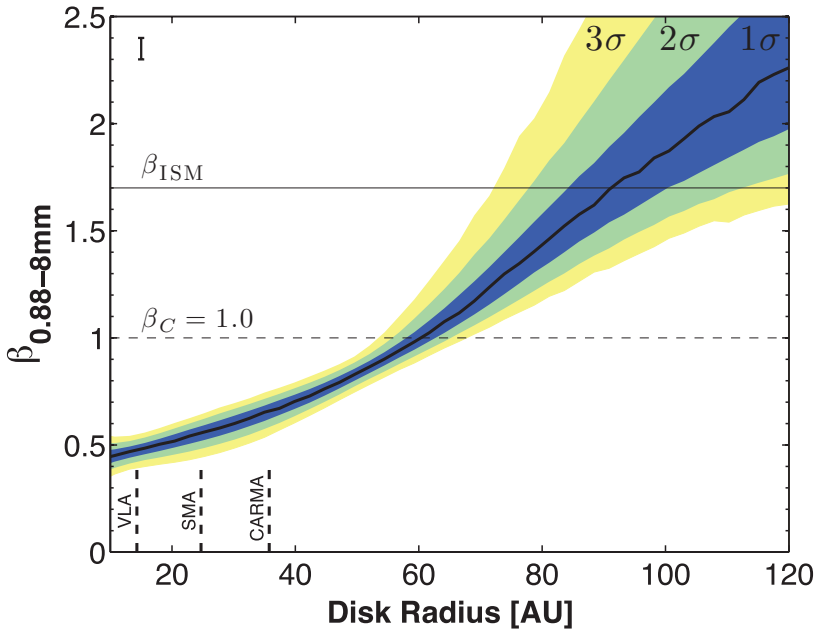

Fig. 1.17 The best fit model of the radial distribution of β of a protoplanetary disk AS209 (Pérez et al., 2012).

coupled grain size also depends on the orbital radius (see Eq.(1.3)). For example, the radial drift barrier at 5 AU occurs when dust grains have 1 m-sized. This corresponds to at 50 AU with 1 mm-sized dust grains. Because the observations represent the outer disk, the low-β problem is a good test bed of the radial drift problem.

Many explanations have applied to the mystery of the grain growth. Pinilla et al. (2012) proposed that if the disk gas has density irregularities, the pressure bumps can prevent the millimeter grains from falling onto the central star. They have shown how large the amplitude of gas density is required. However, mechanisms are uncertain such as the origin of these density perturbation and the timescale during which bumps are maintained. Ricci et al. (2012) tried to explain the millimeter-wave observations by including optically thick regions. They proposed the potential explanations of millimeter-wave observations by optically thick sub-regions, where the particles are concentrated.

1.4.4 Opacity of porous dust aggregates

As discussed in the previous sections, dust grains can form porous aggregates in protoplanetary disks. Opacity of porous dust aggregates has also been studied. To calculate the optical properties of porous dust aggregates, Draine (1988) proposed a discrete-dipole approximation method, which is by replacing the constituent particles as dipoles. However, DDA takes a huge computational cost. Kozasa et al. (1992) investigated the optical properties of BCCA and BPCA aggregates. They compared the results derived from the discrete dipole approximation (DDA) and the Mie theory with effective medium theory (EMT). EMT is expected to greatly reduce the computational cost but is not as accurate as DDA. The results show that the absorption cross section is reproduced by the effective medium theory within a factor of 1.3. However, the scattering cross section at short wavelengths is not reproduced by the EMT. At short wavelengths, the results of EMT deviates from the results of DDA. In contrast, EMT reproduces the results of DDA at long wavelengths. Shen et al. (2008, 2009) also compared the DDA and EMT, and show that EMT approximation provide a good approximation with an error in 20% in the case of absorption cross section.

In the previous calculations by DDA, a number of monomers is less than 10^5 because of a limit of computational costs. However, dust aggregates that we discuss in this thesis have larger number of monomers. Thus, we use EMT to calculated the opacity of dust aggregates in Chapter. 4. Although the accuracy of EMT in the case of a large number of monomers has not been confirmed yet, this would be a first step to calculate the opacity of highly porous aggregates.

1.5 This thesis: introducing the static compression

The ultimate goal is to reveal the dust coagulation in planetesimal formation, which is the first stage of planet formation. There have been three major problems in planetesimal formation, which are radial drift (Adachi et al., 1976), fragmentation (Blum & Münch, 1993), and bouncing (Zsom et al., 2010) problems as discussed in this chapter. Recently, several authors have proposed that highly porous aggregates can avoid these barriers: the rapid growth to avoid the radial drift (Okuzumi et al., 2012), sticky ice to overcome the fragmentation (Wada et al., 2009), and fluffy structure which does not make bouncing behavior (Wada et al., 2008).

The problem of the porous aggregation is that the result of the porosity evolution is not consistent planetesimals. Figure 1.18 summarizes the problems and filling factor evolution in previous studies. In this figure, we do not plot the fragmentation barrier because icy aggregates can avoid the complete disruption (Wada et al., 2009). Thus, we consider the region beyond the snowline in protoplanetary disks. The fractal growth with collisional compression avoids the bouncing and radial drift barriers. However, they are not compressed by collisions to make compact planetesimals, whose internal density is ~ 1 g cm^{-5} (Okuzumi et al., 2012). Therefore, in order to create planetesimals, we have to consider other mechanisms to compress the fluffy aggregates to kilometer-sized planetesimals.

In this thesis, we are aiming to tackle this problem by introducing another mechanism of compressing porous dust aggregates: static compression. To introduce the static compression in porosity evolution of dust aggregates, we investigate the compressive strength of porous dust aggregates in Chapter 2. We will formulate the compressive strength both numerically and analytically.

Next, we will apply the formula to the porosity evolution in protoplanetary disks in Chapter 3. As origins of the static compression, we consider the pressure due to gas drag and self-gravity of dust aggregates. The dust aggregates are possibly compressed by ram pressure of the disk gas because the dust aggregates have relative velocity against the disk gas. The velocity increases as dust aggregates grow and become decoupled from the gas. Therefore, the gas-drag compression is expected to be effective when the dust aggregates are mostly decoupled from the gas. In addition, when the dust aggregates grow and their mass becomes massive enough, the aggregates no longer support their structure against their own gravity. Then, the aggregates are expected to be compressed due to their self-gravity. We will show that the dust aggregates are successfully compressed to form compact and massive objects, which are consistent with planetesimals. Moreover, we will show that the

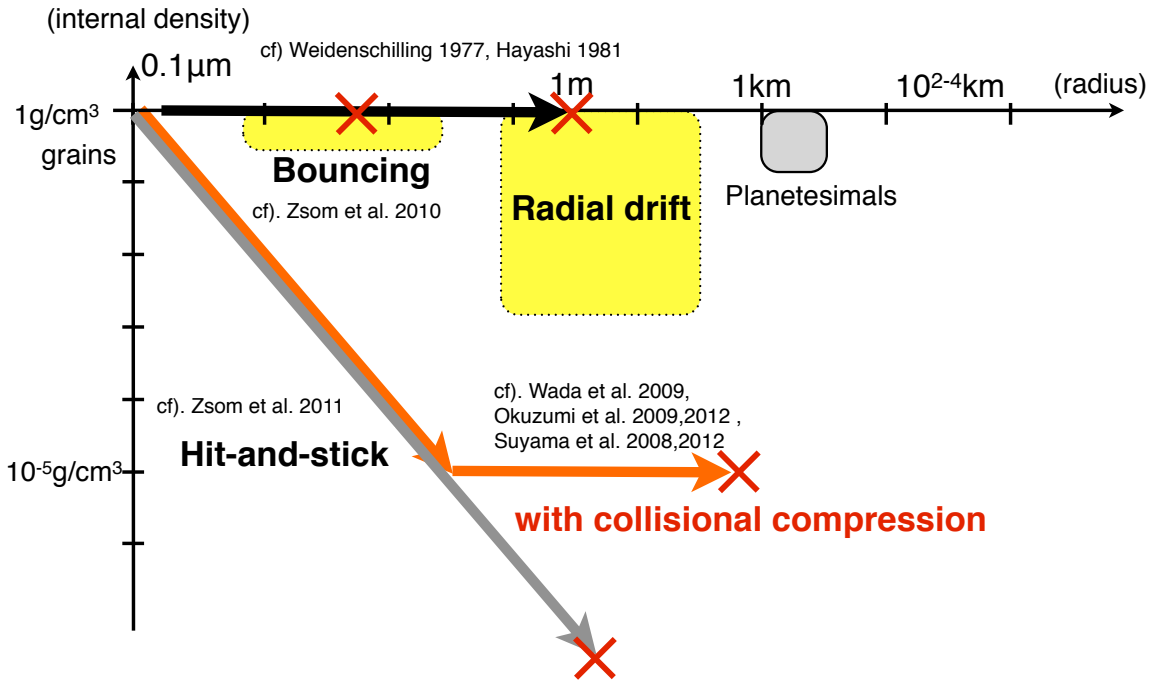

Fig. 1.18 The filling factor (or porosity) evolution of dust aggregates in previous studies. The filling factor is plotted against aggregate radius. The black solid line shows the compact growth (e.g., Hayashi, 1981). The gray solid line shows the fractal growth without compression (Zsom et al., 2011). The orange solid line shows the fractal growth with collisional compression (Okuzumi et al., 2012). The yellow regions represent the bouncing and radial drift barriers.

aggregates successfully overcome the three problems in planetesimal formation.

Finally, we calculate the observational properties of the fluffy dust aggregates expected to be observed in protoplanetary disks in Chapter 4. We will show that the aggregate radius and the filling factor generally degenerate in opacity, except for the resonance and scattering opacity at long wavelengths. This means that the observed emission of protoplanetary disks could be from fluffy dust aggregates. We will also propose a way to distinguish between porous aggregates and compact grains from radio-wave observations.

In Chapter 5, we summarize this thesis and discuss the future work.

Chapter 2

Static compression of porous dust aggregates

A part of this chapter has been published as Kataoka, A., Tanaka, H., Okuzumi, S., & Wada, K. 2013a, A&A, 554, A4 (Kataoka et al., 2013a).

In protoplanetary disks, dust grains coagulate with each other and grow to form aggregates. While these aggregates grow by coagulation, their filling factor ϕ decreases to $\phi \ll 1$; however, comets, the remnants of these early planetesimals, have $\phi \sim 0.1$. Thus, static compression of porous dust aggregates is important in planetesimal formation. However, the static compressive strength has only been investigated for relatively high-density aggregates ($\phi > 0.1$). We investigate and find the compressive strength of highly porous aggregates ($\phi \ll 1$). We performed three-dimensional N-body simulations of aggregate compression with a particle-particle interaction model. We introduced a new method of static compression: the periodic boundary condition was adopted, and the boundaries move with low speed to get closer. The dust aggregate is compressed uniformly and isotropically by themselves over the periodic boundaries. We empirically derive a formula of the compressive strength of highly porous aggregates ($\phi \ll 1$). We check the validity of the compressive strength formula for wide ranges of numerical parameters, such as the size of initial aggregates, the boundary speed, the normal damping force, and material. We also compare our results to the previous studies of static compression in the relatively high-density region ($\phi > 0.1$) and confirm that our results consistently connect to those in the high-density region. The compressive strength formula is also derived analytically.

2.1 Introduction

Planetesimal formation is a key issue in the study of how planets form in protoplanetary disks (Hayashi et al., 1985; Weidenschilling & Cuzzi, 1993). However, the collisional growth of the dust from submicron-sized dust to kilometer-sized planetesimals is still unknown.

In the growth process, one of the most important but unresolved problems is to determine the internal structural evolution of dust aggregates. The internal structure of dust is important in planetesimal formation because the dynamics of dust aggregates in protoplanetary disks are determined by coupling of gas and dust, in other words, the size and internal density of dust aggregates. In the early stage of dust coagulation in protoplanetary disks, the collision energy of the aggregates is too low to cause collisional compression (Blum, 2004; Okuzumi et al., 2012; Ormel et al., 2007; Zsom et al., 2011, 2010). As a result, the internal mass density ρ decreases to $\rho < 1.0$ g cm^{-3}.

Both theoretical and experimental studies have shown that mutual collisions lead dust aggregates to have their fractal dimension $D \sim 2$, which is so-called ballistic cluster-cluster aggregation (BCCA) (Blum & Wurm, 2000; Kempf et al., 1999; Krause & Blum, 2004; Meakin, 1991; Paszun & Dominik, 2006; Smirnov, 1990). The dust aggregates would be gradually compacted or disrupted in coagulation because of the increase in impact energy. This compaction has been investigated with numerical N-body simulations that consider particle-particle interactions (Dominik & Tielens, 1997; Paszun & Dominik, 2008, 2009; Seizinger et al., 2012; Suyama et al., 2008, 2012; Wada et al., 2007, 2008, 2009).

In most previous studies investigating dust growth in protoplanetary disks, dust grains have been assumed to have constant internal mass density for simplicity (Birnstiel et al., 2010a; Brauer et al., 2008; Nakagawa et al., 1981; Tanaka et al., 2005). However, dust porosity evolves during dust growth in real protoplanetary disks. In recent dust coagulation calculations, porosity evolution has been considered to be based on experimental and theoretical results (Okuzumi et al., 2012, 2009; Ormel et al., 2007; Zsom et al., 2011). These results also suggest that ρ decreases as $\rho \ll 0.1$g cm^{-3}.

In the most recent work, the dominant coagulation mode has been shown to be similar-size collisions of dust aggregates though dust grains have size distribution (Okuzumi et al., 2012). As a result, their fractal dimension is approximately equal to two, and their internal mass density ρ has been shown to become 10^{-5} g cm^{-3} (equivalent to be the filling factor $\phi = 10^{-5}$ for ice particles with a density of 1.0 g cm^{-3}). Such fluffy dust aggregates are believed to become planetesimals. Since comets in our solar system, which would be remnants

of planetesimals, have their internal mass density of ~ 0.1 g cm^{-3} (A'Hearn, 2011), dust aggregates must be compressed from $\rho \ll 0.1$ g cm^{-3} to $\rho \sim 0.1$ g cm^{-3} in protoplanetary disks.

Compression at dust aggregate collisions has been investigated in previous studies. When collisional impact energy exceeds the critical energy, dust aggregates are compacted by their collision (e.g. Dominik & Tielens, 1997; Suyama et al., 2008; Wada et al., 2007, 2008, 2009). However, the collisional compression is not effective at compressing dust aggregates (Okuzumi et al., 2012).

One of the other compression mechanisms in protoplanetary disks is static compression by disk gas or self-gravity. The static compressive strength of dust aggregates has been investigated both experimentally and numerically (Güttler et al., 2009; Paszun & Dominik, 2008; Seizinger et al., 2012). However, the compressive strength has been examined only relatively compact aggregates with $\rho \gtrsim 0.1$g cm^{-3} because their initial aggregates are ballistic particle-cluster aggregation (BPCA) clusters. Because ρ decreases to $\rho \ll 0.1$g cm^{-3}, at least in the early stage of dust growth, we need to reveal the static compressive strength with $\rho \ll 0.1$g cm^{-3}.

In this work, we investigate the static compression of highly porous aggregates with $\rho < 0.1$g cm^{-3} by means of numerical simulations and an analytical approach. It is challenging to perform numerical simulations of the static and uniform compression of highly porous aggregates. Because such porous aggregates have low sound speed, we have to compress them at a much slower velocity than in the case of compact aggregates, as is shown in our simulations. Such a slow compression of the fluffy aggregates costs much computational time.

In previous numerical studies of static compression, a dust aggregate is compressed by a wall moving in one direction (Paszun & Dominik, 2008; Seizinger et al., 2012). However, this method has disadvantages when reproducing uniform and isotropic compression. There are also side walls that do not move. These side walls also obstruct the tangential motion of monomers in contact with the walls, causing artificial stress on the aggregate, which restructures them. Moreover, since they measure the pressure with the force on the moving wall, the side walls may affect the pressure measurement. In the present work, we develop a new method reproducing static compression. Instead of the walls, we adopt periodic boundary conditions and the boundaries get closer to each other. With these slowly moving periodic boundaries, the aggregate is compressed uniformly and naturally. The periodic boundary condition also enables us to represent a much larger aggregate than inside the computational region. This saves on computational time remarkably.

This paper is organized as follows. We describe the model of our numerical simulations in Section 2.2. We show the results of our simulations and find the compressive strength in Section 4.3. We confirm the obtained static compressive strength formula analytically in Section 2.4, and present our conclusion in Section 4.6.

2.2 Simulation setting

We performed three-dimensional numerical simulations of the compression of a dust aggregate consisting of a number of spherical monomers. As the initial aggregate, we adopted a BCCA cluster. In this method, we solved interactions between all monomers in contact in each time step. Interactions between monomers in contact are formulated by Dominik & Tielens (1997) and reformulated by using the potential energies by Wada et al. (2007). We used the interaction model proposed by Wada et al. (2007) in this work. We briefly summarize the particle interaction model and material constants (see Wada et al. (2007) for details). Moreover, we describe the additional damping force in normal direction and the simulation setting in this section. In our simulations, the aggregate is gradually compressed by its copies over the moving periodic boundaries. This is an appropriate method of simulating uniform and isotropic compression. We also describe the boundary condition in this section. Since we do not have walls to measure the pressure in the periodic boundary condition, we use a similar manner of pressure measurement in molecular dynamics simulations. We also introduce the method of pressure measurement below.

2.2.1 Interaction model

We calculate the direct interaction of each connection of particles, taking all mechanical interactions modeled by Dominik & Tielens (1997) and Wada et al. (2007) into account. The material parameters are the monomer radius r_0, surface energy γ, Young's modulus E, Poisson's ratio ν, and the material density ρ_0. Table 2.1 lists the values of the material parameters for ice and silicate.

We perform N-body simulations with ice particles except for one case with silicate particles. In protoplanetary disks, ice particles are the most dominant dust material beyond the snowline. Moreover, the computational time required for calculating ice particles is less than for silicate. Thus, we adopt ice particles in most simulations. We also treat a silicate case to compare with a previous study (Seizinger et al., 2012).

The critical displacement still shows a discrepancy between theoretical ($\xi_{\rm crit} = 2$ Å) and

Table 2.1 Material parameters in our simulation

Material	ice	silicate (same as Seizinger et al. (2012))
Monomer radius r_0 [μm]	0.1	0.6
Surface energy γ [mJ m^{-2}]	100	20
Young's modulus E [GPa]	7.0	2.65
Poisson's ratio ν	0.25	0.17
Material density ρ_0 [g cm^{-3}]	1.0	2.65
critical rolling displacement $\xi_{\rm crit}$ [Å]	8	20

experimental ($\xi_{\rm crit}$ = 32 Å) studies (Dominik & Tielens, 1997; Heim et al., 1999). We note that the experimental studies used silica particles. We adopt the same parameter as in Wada et al. (2011), $\xi_{\rm crit}$ = 8 Å as a typical length for ice particles, and $\xi_{\rm crit}$ = 20 Å for silicate particles to compare with Seizinger et al. (2012).

The parameter $\xi_{\rm crit}$ is related to strength of rolling motion. The rolling motion between monomers is crucial in compression. The rolling energy $E_{\rm roll}$ is the energy required to rotate a particle around a connecting point by 90 degrees. The rolling energy can be written as

$$E_{\rm roll} = 6\pi^2 \gamma r_0 \xi_{\rm crit} \tag{2.1}$$

(see Wada et al. (2007) for details). In the case of ice monomers, for example, $E_{\rm roll}$ = 4.74×10^{-9} erg for $\xi_{\rm crit}$ = 8Å.

We use a normalized unit of time in our simulations. For ice particles, the normalized unit of time is

$$t_0 = 0.67 \left(\frac{\rho_0^{1/2} r_0^{7/6}}{E^{*1/3} \gamma^{1/6}} \right) = 1.37 \times 10^{-10} \text{ s}, \tag{2.2}$$

where $E^* = 2(1-\nu^2)/E$. t_0 is a characteristic time, and approximately represents the oscillation time of particles in contact at the critical collision velocity (see Wada et al. (2007) for details).

2.2.2 Damping force in normal direction

The normal force between two monomers is repulsive when the monomers are close or attractive when they are stretched out. Thus, normal oscillations occur at each connection. For realistic particles, these oscillations would dissipate because of viscoelasticity or hysteresis in the normal force (e.g. Greenwood & Johnson, 2006; Tanaka et al., 2012). For such

damping of normal oscillation, we add an artificial normal damping force to the particle interaction model, following the previous studies (Paszun & Dominik, 2008; Seizinger et al., 2012; Suyama et al., 2008).

Assuming that two particles in contact have their position vectors $\boldsymbol{x}_1$ and $\boldsymbol{x}_2$, respectively, the contact unit vector $\boldsymbol{n}_c$ is defined as

$$\boldsymbol{n}_c = \frac{\boldsymbol{x}_1 - \boldsymbol{x}_2}{|\boldsymbol{x}_1 - \boldsymbol{x}_2|} \tag{2.3}$$

(see Figure 2 in Wada et al. (2007)). We introduce a damping force between contact particles in normal direction, defined as

$$\boldsymbol{F}_{\rm damp} = -k_{\rm n}\frac{m_0}{t_0}\boldsymbol{n}_c \cdot \boldsymbol{v}_{\rm r}, \tag{2.4}$$

where k_n is the damping coefficient in normal direction and m_0 the monomer mass. The adopted value of k_n is on the order of 0.01. To show that the result is independent of the normal oscillation damping, we perform N-body simulations with the damping factor k_n as a parameter.

The timescale of damping is

$$\tau_{\rm damp} \sim \frac{t_0}{k_n} \sim 10^2 t_0, \tag{2.5}$$

for $k_n = 0.01$, it is much shorter than the simulation timescale, which is typically $\sim 10^7 t_0$. We show that the obtained compressive strength is independent of the artificial normal damping force in our simulations (see Section 2.3.4).

2.2.3 Uniform compression by moving boundaries

We adopt the periodic boundary condition in our simulations. The aggregate in the computational region is surrounded by its copies, as shown in Figure 2.1. Initially, we set a cubic box whose sides are periodic boundaries with a size of L larger than the aggregate. Thus, the initial BCCA cluster is detached from its neighboring copies over the periodic boundaries. In our simulations, we gradually move the boundaries to the center of the aggregate to get closer to one another. As a result, the aggregate sticks to the neighboring copies and is compressed by them in a natural way. Therefore, the aggregate in the computational region corresponds to a small part of a whole large aggregate. In other words, although the number of particles in numerical simulations are limited because of computational cost, the periodic

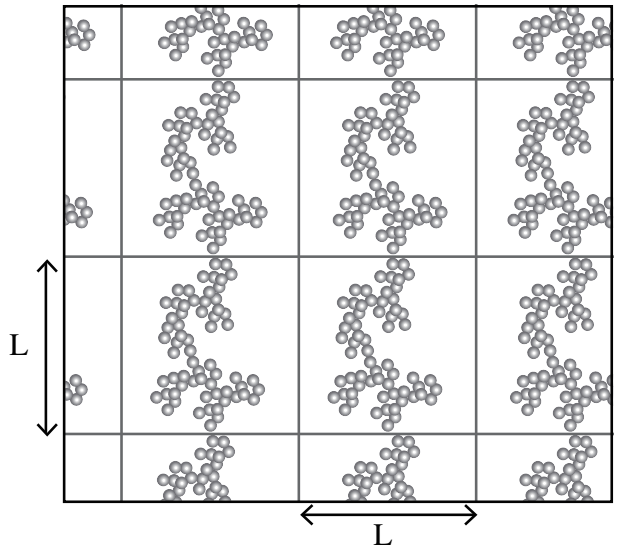

Fig. 2.1 Schematic drawing of the periodic boundary condition. Each box illustrates a boundary box with a side length L for all directions. When the boundary starts to get closer, the aggregate sticks to the neighboring aggregates over the boundary and is compressed by them. It should be noted that this picture is illustrated in the 2D direction, but our simulations are performed in 3D.

boundary condition enables us to investigate a large aggregate, such as a $\sim$ cm-sized dust aggregate in protoplanetary disks.

Another advantage of the periodic boundary condition is that we do not need to introduce the wall for compression. In the previous N-body simulations of static compression, dust aggregates are compressed by using the wall against the dust aggregate (Paszun & Dominik, 2008; Seizinger et al., 2012). The wall itself may have some artificial effects on such experiments. For example, the wall moves in one direction and thus this may be different from isotropic compression. Besides, wall-particle interaction is different from particle-particle interaction, so it must be treated carefully. In contrast, the periodic boundary condition does not need walls for compression because a dust aggregate is compressed by the neighboring aggregate over the periodic boundary. In addition, the periodic boundaries in three directions make it possible to compress the aggregate isotropically. We calculate not only the interactions of particles in contact inside the computational region but also the interactions of the particles in contact across the periodic boundaries. Thus, no special treatment of interactions, which is wall-particle interactions in the case of simulations with walls in previous studies, is required when a particle crosses the periodic boundaries.

The computational cubic region has length L, and the coordinates in x, y, and z directions

are set to be $-L/2 < x < L/2$, $-L/2 < y < L/2$, and $-L/2 < z < L/2$, respectively. We adopt periodic boundary conditions for all directions to reproduce a part of a large aggregate, where L decreases with time t, $L = L(t)$. The initial size of the box L_0 is adopted as the maximum size of the dust aggregate in x, y, and z directions.

With the settings above, we move the boundaries of the computational region toward the center of the region with a constant strain rate. The velocity at the boundary is given by

$$v_{\rm b} = -\frac{C_{\rm v}}{t_0} L(t), \tag{2.6}$$

where $C_{\rm v}$ is a dimensionless parameter (we call $C_{\rm v}$ the strain rate parameter hereafter). Owing to this definition of the boundary speed, the aggregate is compressed at a constant strain rate independent of the region scale L.

The box size decreases with the constant rate $C_{\rm v}$ in three directions. This corresponds to isotropic compression. Since $\frac{dL}{dt} = 2v_b$, the box size is written as

$$L = L_0 \exp\left(-2C_{\rm v}\frac{t}{t_0}\right). \tag{2.7}$$

Therefore, the whole time of compression is $t_0/C_{\rm v}$. Typically we chose $C_{\rm v} = 3\times10^{-7}$ so the compression time is ~ 0.5 ms.

When a particle crosses a periodic boundary, the velocity should be treated carefully to reproduce the quasi-static compression with periodic boundary condition. Figure 2.2 illustrates how to calculate the velocity of particles across the periodic boundary. When a particle goes out of the computational region across the boundary at $x = L/2$, we relocate the particle to the opposite side (i.e., from the boundary at $x = -L/2$). In that case, the position of the particle in x direction is converted as

$$x \longmapsto x - L \tag{2.8}$$

Since the two boundaries at $x = -L/2$ and $x = L/2$ have a relative velocity of $2v_{\rm b}$, the x-component of the velocity v_x of the particle is also converted as

$$v_x \longmapsto v_x + 2v_b. \tag{2.9}$$

Owing to the conversion of v_x, the velocity of particle against the boundary that the particle crosses does not change before and after the crossing. For a particle across the boundary at

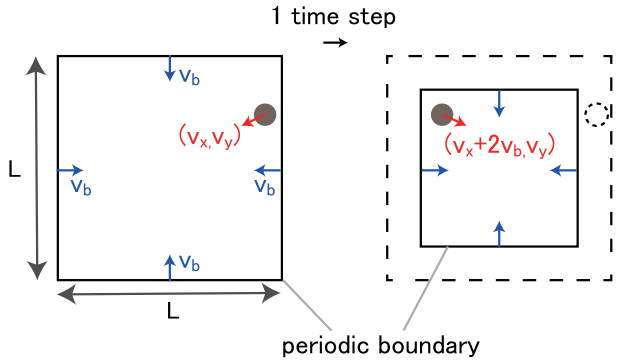

Fig. 2.2 Schematic drawing to illustrate how the particle velocity is calculated when a particle crosses a periodic boundary. For simplicity, we consider this situation in a 2D field, but we actually calculate this in a 3D situation. We consider that a dust particle is close to the boundary in the left figure. In the next time step, the particle crosses the boundary (dashed circle in the right figure). We put the particle on the other side of the boundary as expressed in Equations (2.8) and (2.10). The velocity component is converted as expressed in Equations (2.9) and (2.11). This treatment reproduces the isotropic compression in the velocity field well.

$x = -L/2$, the position and the velocity are converted as

$$x \longmapsto x + L \tag{2.10}$$

$$v_x \longmapsto v_x - 2v_b. \tag{2.11}$$

We also have the same treatments for particles across the boundaries at $y = \pm L/2$ and $z = \pm L/2$.

We introduce the constant strain rate at the boundaries for scaleless discussion. However, the initial aggregate is not moving. As the simulation starts, if all the particles in the aggregate are not moving, only the particles close to the boundaries have initial velocity. This is not a constant strain rate. To reproduce the scaleless constant strain rate initially, therefore, we first give all monomers the velocity smoothly connected to the boundary speed. The initial velocity is expressed as

$$\boldsymbol{v}(\boldsymbol{r}) = v_\mathrm{b} \times \frac{\boldsymbol{r}}{L_0/2}, \tag{2.12}$$

where $\boldsymbol{r}$ is the position vector of the monomers.

2.2.4 Pressure measurement

In previous studies, a dust aggregate is enclosed by walls, and the pressure is calculated by measuring the force exerted on the walls by the dust aggregate. In this work, a dust aggregate is compressed by themselves because of the periodic boundary condition. Therefore, we introduce another method of measuring the pressure on the aggregate. We calculate the pressure of the dust aggregate in the standard way in molecular dynamics simulations using the virial theorem as follows (e.g., Haile, 1992).

We consider a virtual box that encloses the aggregate under consideration. We define the force acting from the walls of the virtual box on the particle i as $\boldsymbol{W}_i$, and the sum of the forces from other particles on the particle i as $\boldsymbol{F}_i$. The equation of motion of the particle i is given by

$$m\frac{d^2\boldsymbol{r}_i}{dt^2} = \boldsymbol{W}_i + \boldsymbol{F}_i. \tag{2.13}$$

We take a scalar product of both sides of the equation with $\boldsymbol{r}_i$ and take a long time average of both sides with time interval τ. The lefthand side becomes

$$m\frac{1}{\tau}\int_0^\tau \boldsymbol{r}_i \cdot \frac{d^2\boldsymbol{r}_i}{dt^2} = m\frac{1}{\tau}\left[\boldsymbol{r}_i \cdot \frac{d\boldsymbol{r}_i}{dt}\right]_0^\tau - m\frac{1}{\tau}\int_0^\tau \frac{d\boldsymbol{r}_i}{dt}\cdot\frac{d\boldsymbol{r}_i}{dt}dt. \tag{2.14}$$

The first term on the righthand side vanishes in the limit of $\tau \to \infty$. We define the taking-a-long-time average in t as $\langle\rangle_t$. Taking a summation of all particles and a long time average of Equation (2.13), we obtain

$$\left\langle \sum_{i=1}^{N} \frac{1}{2} m\left(\frac{d\boldsymbol{r}_i}{dt}\right)^2 \right\rangle_t = -\frac{1}{2}\left\langle \sum_{i=1}^{N} \boldsymbol{r}_i \cdot (\boldsymbol{W}_i + \boldsymbol{F}_i) \right\rangle_t. \tag{2.15}$$

We define the average of the stress in three directions as pressure P. Thus, the first term on the righthand side is related to P. The pressure is an average of all forces acting on the wall from all particles. Using the normal vector $\boldsymbol{n}$ of the wall surface directed outward, the force received by the wall that has an area dS is $P\boldsymbol{n}dS$. Therefore,

$$\left\langle \sum_i \boldsymbol{r}_i \cdot \boldsymbol{W}_i \right\rangle_t = -\int_S P\boldsymbol{n}\cdot\boldsymbol{r}dS = -3PV. \tag{2.16}$$

This equation is obtained by taking surface integral as

$$\int_S \boldsymbol{n}\cdot\boldsymbol{r}dS = \int_V \mathrm{div}\ \boldsymbol{r}dV = \int_V \left(\frac{\partial x}{\partial x} + \frac{\partial y}{\partial y} + \frac{\partial z}{\partial z}\right)dV = 3V. \tag{2.17}$$

The translational kinetic energy K, averaged over a long time, is given by

$$K = \left\langle \sum_{i=1}^{N} \frac{1}{2} m \left(\frac{d\boldsymbol{r}_i}{dt} \right)^2 \right\rangle_t . \tag{2.18}$$

Using K and P, Equation (2.15) gives an expression of P as

$$P = \frac{2}{3} K/V + \frac{1}{3} \left\langle \sum_i \boldsymbol{r}_i \cdot \boldsymbol{F}_i \right\rangle_t /V. \tag{2.19}$$

We define the force from particle j on particle i as $\boldsymbol{f}_{i,j}$. Force $\boldsymbol{F}_i$ can be written as a summation of the force from another particle as

$$\boldsymbol{F}_i = \sum_{j \neq i} \boldsymbol{f}_{i,j}. \tag{2.20}$$

Using $\boldsymbol{f}_{i,j} = -\boldsymbol{f}_{j,i}$, we finally obtain the pressure measuring formula as

$$P = \frac{2}{3} K/V + \frac{1}{3} \left\langle \sum_{i<j} (\boldsymbol{r}_i - \boldsymbol{r}_j) \cdot \boldsymbol{f}_{i,j} \right\rangle_t /V. \tag{2.21}$$

The first term on the righthand side of the equation represents the translational kinetic energy per unit volume, and the second term represents the summation of the force acting at all connections per unit volume. This expression is useful for measuring the pressure of a dust aggregate under compression. We do not need to put any artificial object, such as walls, in simulations because Equation (2.21) is totally expressed in terms of the summation of the physical quantities of each particle, which are the mass, the position, the velocity, and the force acting on the particle. In our calculations, we take an average of pressure for every 10,000 time steps, corresponding to 1000 t_0 because we set 0.1 t_0 as one time step in our simulation.

As mentioned in Section 2.2.2, the adopted damping force corresponds to rapid damping of normal oscillations. Thus, the kinetic energy of random motion rapidly dissipates. This corresponds to the static compression, and thus the compressive strength is determined by the second term of Equation (2.21). We note that this process corresponds to the isothermal compression. In addition, this process is not applicable to the rapid compression.

2.3 Results

The top three panels of Figure 2.3 show snapshots of the evolution of an aggregate under compression in the case where $N = 16384$, $C_v = 3 \times 10^{-7}$, $k_n = 0$, and $\xi_{crit} = 8$ Å. The top three panels have the same scale but different time epochs, which are $t = 0$, $1 \times 10^6 t_0$, and $2 \times 10^6 t_0$. The white particles are inside the computational region enclosed by the periodic boundaries, while the yellow particles are in the neighboring copy regions. (For visualization, we do not draw particles on the front and backsides copy regions.) The bottom three panels represent the projected positions onto the two-dimensional plane for the correspondent top three figures. We confirm that the dust aggregate is compressed by their copies from all directions. As the compression proceeds, the aggregate of white particles is compressed by the neighboring aggregate of yellow particles. We focus on how high pressure is

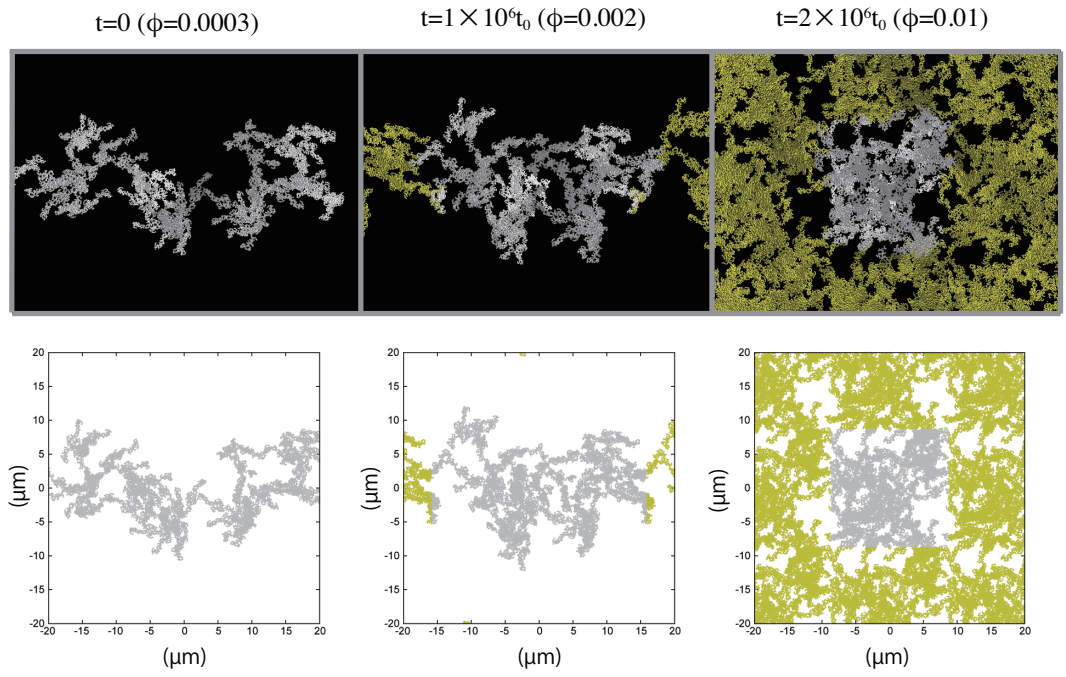

Fig. 2.3 Snapshots of the evolution of an aggregate under compression in the case of $N = 16384$. The top three figures are 3D visualizations. They have the same scale with different time epochs. The white particles are inside a box enclosed by the periodic boundaries. The yellow particles are in neighboring boxes to the box of white particles. For visualization, we do not draw the copies on the back and front sides of the boundaries but only 8 copies of the white particles across the boundaries. Each bottom figure represents projected positions onto 2D plane of all particles in each corresponding top figure. The gray points in the bottom figures correspond to the positions of the white particles in the top figures, and the yellow points correspond to those of the yellow particles in the top figures. Scales are in μm.

generated by quasi-static compression in numerical simulations. Our numerical simulations have several parameters: the size of the initial BCCA cluster, the compression rate, the normal damping force, and the critical displacement (corresponds to the rolling energy). We investigate the dependence of the pressure on these parameters, by performing several runs with different parameter sets. Although we assume ice aggregates in most runs, we also investigate cases of silicate aggregates to compare them with previous studies.

2.3.1 Fiducial run: obtaining the compressive strength

We put a BCCA cluster as the initial aggregate. For each set of parameters, we randomly create ten BCCA clusters following Okuzumi et al. (2009), and take arithmetic averages of the ten simulations of the different initial clusters. The pressure is measured using Equation (2.21) at each run. We define the filling factor of an aggregate as

$$\phi = \frac{V_0 N}{V}, \tag{2.22}$$

where V_0 is the monomer volume, N the number of monomers of the aggregate, and V the volume enclosed by the boundaries, which has a length of L. The filling factor also can be written as $\phi = \rho/\rho_0$. Figure 2.4 shows that the measured pressure as a function of the filling factor $\phi(t)$. The parameters of the simulations are $N = 16384$, $C_\mathrm{v} = 3\times10^{-7}$, $k_\mathrm{n} = 0.01$, and $\xi_\mathrm{crit} = 8$ Å. The corresponding E_roll is 4.74×10^{-9}erg for $\xi_\mathrm{crit} = 8$ Å. Each colored line in Figure 2.4(a) shows each simulation with the different initial shape of the aggregate. Figure 2.4(b) shows the arithmetic average of the pressure measured in ten different runs. Each line shows in different ranges of ϕ. The lowest ϕ is determined with the largest size of the initial boundary boxes of the ten runs. We find that the compressive strength is reproduced well by

$$P = P_0\phi^3, \tag{2.23}$$

where $P_0 = 4.74\times10^5$ Pa. We analytically discuss why the compressive strength is proportional to ϕ^3 in Section 2.4. In the high-density region ($\phi \gtrsim 10^{-1}$), the measured strength deviates from the line of $P = P_0\phi^3$. This is because the dissipation mechanism changes in the high-density region (see Section 2.3.4). The deviation in the low-density region ($\phi \lesssim 3\times10^{-3}$) is partly caused by a finite boundary speed (or compression rate) as discussed in the next section. Another reason for the deviation in the low-density region is related to

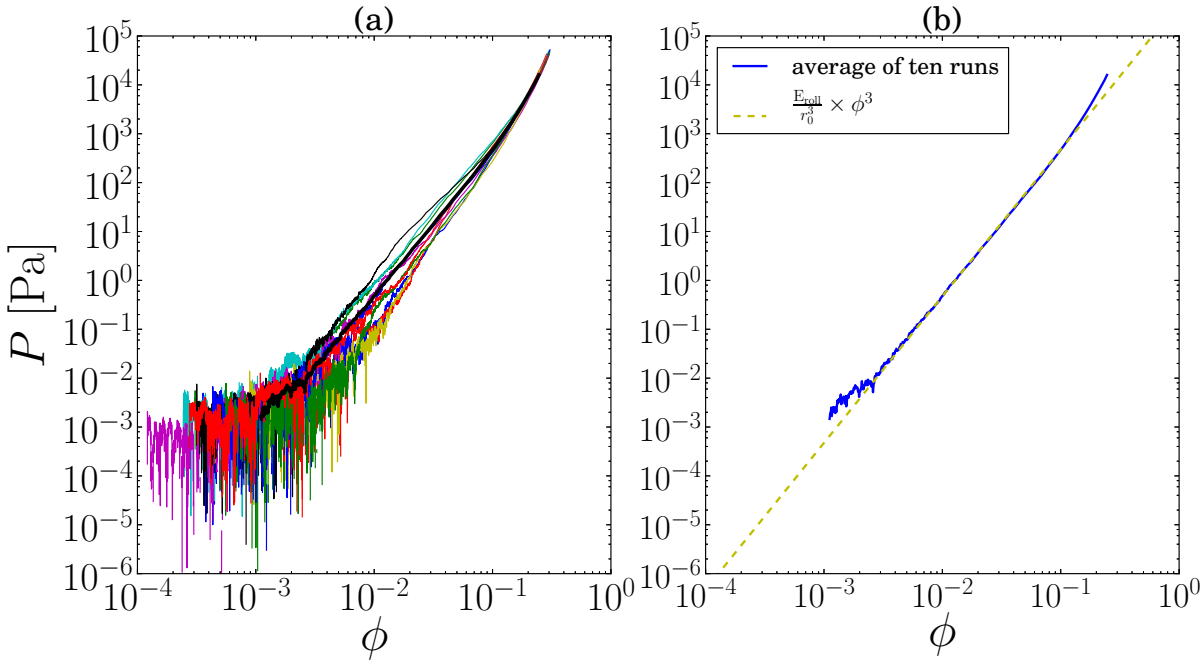

Fig. 2.4 (a) Pressure P in [Pa] against filling factor ϕ. The ten thin solid lines show the results for the initial BCCA clusters with different initial random numbers and thick solid line shows the arithmetic average of the ten runs. (b) Pressure P in [Pa] against filling factor ϕ. Same as the thick solid line in (a) plotted with a dotted line of Equation (2.25). The parameters are $N = 16384$, $C_{\rm v} = 3 \times 10^{-7}$, $k_n = 0.01$, and $\xi_{\rm crit} = 8$ Å.

the density of the initial BCCA cluster. The filling factor of BCCA $\phi_{\rm BCCA}$ is estimated as

$$\phi_{\rm BCCA} = \frac{V_0 N}{V_{BCCA}} = \left(\frac{3}{5}\right)^{3/2} N^{-1/2}, \tag{2.24}$$

where we use the radius and the volume of a BCCA cluster, $r_{\rm BCCA} = \sqrt{5/3} N^{1/2} r_0$ and $V_{\rm BCCA} = (4\pi/3) r_{\rm BCCA}^3$, respectively (e.g., Suyama et al., 2008). For $N = 16384$, we obtain $\phi_{\rm BCCA} \sim 3 \times 10^{-3}$. In the early stage of compression, ϕ is lower than $\phi_{\rm BCCA}$ because the initial BCCA clusters are apart from each other. This space between BCCA clusters would also cause the deviation from the line of $P = P_0 \phi^3$.

We now discuss the coefficient P_0 of the compressive strength. Wada et al. (2008) show that $E_{\rm roll}$ is important in the collisional compressive strength. Thus, $E_{\rm roll}$ is expected to also be important in the static compressive strength. Considering that the characteristic volume is the monomer's volume $\sim r_0^3$, we suppose $P_0 = E_{\rm roll}/r_0^3$, based on dimension analysis. Therefore, the compressive strength can be written as

$$P = \frac{E_{\rm roll}}{r_0^3} \phi^3. \tag{2.25}$$

We analytically discuss and confirm this equation in Section 2.4. We also plot this equation in Figure 2.4(b). This figure clearly shows that the result is well fit by Equation (2.25).

We show that compressive strength is proportional to $\xi_{\rm crit}$, which is proportional to the rolling energy $E_{\rm roll}$ in Section 2.3.5. We also confirm that Equation (2.25) is applicable to the case of different r_0 in the silicate case.

2.3.2 Dependence on the boundary speed

To statically compress the aggregate, we should move the boundary at a low enough velocity not to create inhomogeneous structure. Figure 2.5 shows the dependency on the strain rate parameter. Each line shows the average of ten runs. The fixed parameters are $N = 16384$, $k_n = 0.01$, and $\xi_{\rm crit} = 8$ Å. The strain rate parameter $C_{\rm v}$ is equal to 1×10^{-7}, 3×10^{-7}, 1×10^{-6}, 3×10^{-6}, and 1×10^{-5}. The higher $C_{\rm v}$, the higher pressure in the low density region is required for compression. This is mainly caused by the ram pressure from the boundaries with high speed.

When the compression proceeds and the density becomes higher to reach the line of Equation (2.25), the pressure follows the equation. From Figure 2.5, $C_{\rm v} = 3 \times 10^{-7}$ creates a sufficiently low boundary speed. The boundary speed can be calculated as a function of

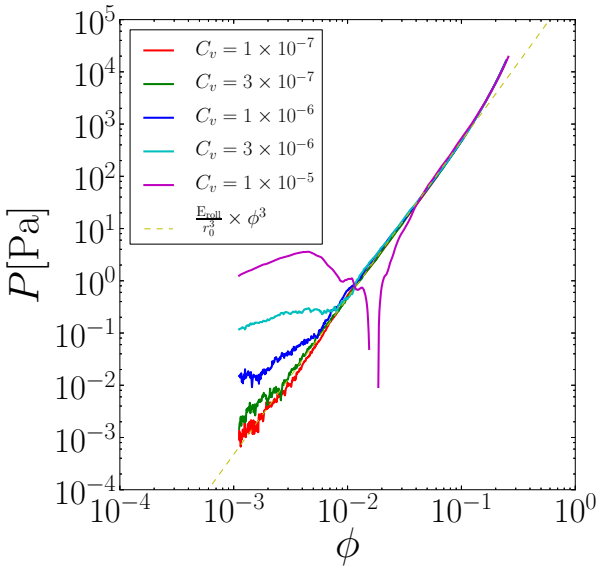

Fig. 2.5 Pressure P in [Pa] against filling factor ϕ with different strain rate parameter $C_{\rm v}$. Each line shows the average of ten runs of the fixed strain rate: $C_{\rm v} = 1\times10^{-7}, 3\times10^{-7}, 1\times10^{-6}, 3\times10^{-6}, 1\times10^{-5}$. The other parameters are the same for every ten runs : $N = 16384$, $k_n = 0.01$, and $\xi_{\rm crit} = 8$ Å. The dashed line is Equation (2.25).

ϕ. Using Equation (2.6) and $\phi = (4/3)\pi r_0^3 N/L^3$, the velocity difference between a boundary and the next boundary, $v_{\rm d}$, can be written as

$$v_{\rm d} = |2v_{\rm b}| = 2\frac{C_{\rm v}}{t_0}\left(\frac{\frac{4}{3}\pi r_0^3 N}{\phi}\right)^{1/3}. \tag{2.26}$$

In the case of $C_{\rm v} = 3\times10^{-7}$, $v_{\rm d}$ = 12.7, 5.9, and 2.7 cm/s for $\phi = 10^{-3}$, 10^{-2}, and 10^{-1}, respectively.

Here, we discuss the velocity difference of boundaries, comparing with the effective sound speed of the aggregates. The effective sound speed can be estimated as

$$c_{\rm s,eff} \sim \sqrt{\frac{P}{\rho}} \sim \sqrt{\frac{E_{\rm roll}}{\rho_0 r_0^3}\frac{\rho}{\rho_0}} \sim \sqrt{\frac{E_{\rm roll}}{m_0}\phi}. \tag{2.27}$$

where we use Equation (2.25). Using the rolling energy of ice particles, $c_{\rm s,eff}$ is given by

$$c_{\rm s,eff} \sim 1.1\times10^3\phi \ {\rm cm/s}. \tag{2.28}$$

Therefore, in the case of $C_{\rm v} = 3\times10^{-7}$, v_d is not low enough in the beginning of the simula-

tion, where the aggregate has a low filling factor. However, the boundary velocity difference reaches lower than the effective sound speed when $\phi \gtrsim 10^{-2}$.

2.3.3 Dependence on the size of the initial BCCA cluster

To confirm that Equation (2.25) is valid in the lower density region, we perform the simulations with the different number of particles, which is equivalent to the different sizes of the initial dust aggregates. Figure 2.6 shows dependence on the number of particles of the initial BCCA cluster. The initial numbers of particles are 1024, 4096, and 16384. The

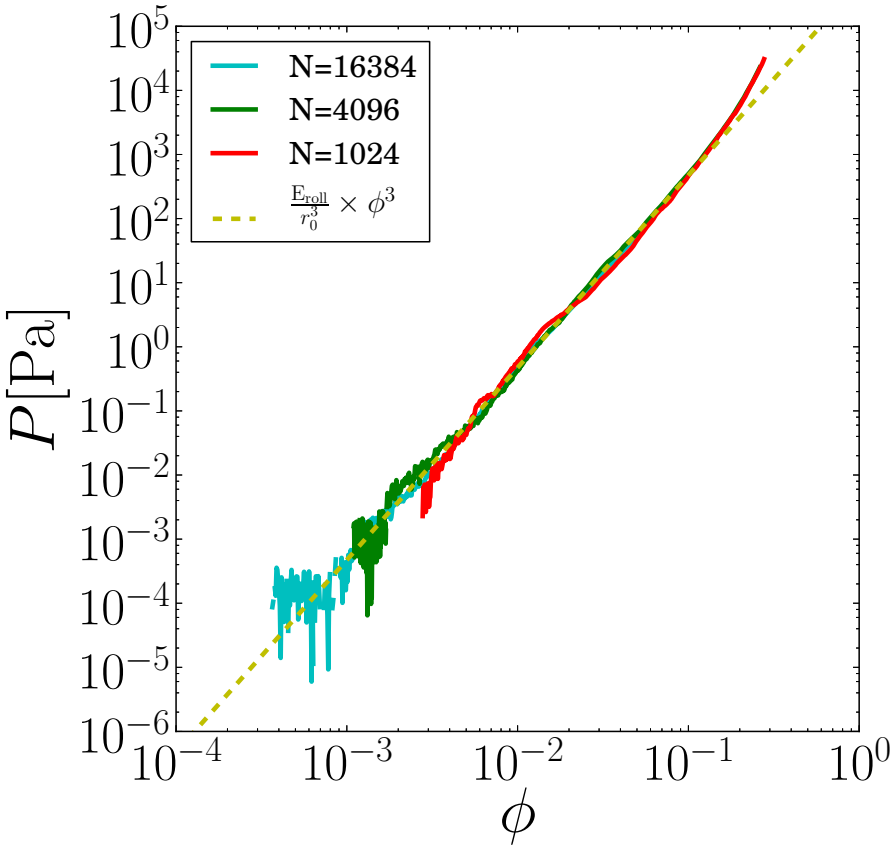

Fig. 2.6 Pressure P in [Pa] against filling factor ϕ with a different number of particles N. Each line shows the average of ten runs of the fixed number of particles: $N = 1024, 4096$, and 16384. The other parameters are $C_v = 3 \times 10^{-7}$, $k_n = 0.01$, and $\xi_{crit} = 8$ Å in the case of $N = 1024, 4096$, and $C_v = 1 \times 10^{-7}$, $k_n = 0.01$, and $\xi_{crit} = 8$ Å in the case of $N = 16384$. The dashed line is Equation (2.25).

other parameters are $C_v = 3 \times 10^{-7}$, $k_n = 0.01$, and $\xi_{crit} = 8$ Å in the case of $N = 1024$ and $N = 4096$, and $C_v = 1 \times 10^{-7}$, $k_n = 0.01$, and $\xi_{crit} = 8$ Å in the case of $N = 16384$. We chose

lower C_v in the case of $N = 16384$ to investigate the strength in lower ϕ region. Each line represents the average of ten runs for each simulation as in Figures 2.4(b) and 2.5. We draw the averaged line from lower ϕ than in Figure 2.5. In such a low ϕ region, we consider that the pressure is zero for some runs because the aggregate is isolated from the copies of the aggregate over the periodic boundaries. Except for the initial deviation in low ϕ, all lines show good agreement with Equation (2.25) where $\phi \lesssim 0.1$. The result agrees in lower ϕ for runs with larger N. Therefore, we conclude that the formula Equation (2.25) is valid for $\phi \lesssim 0.1$.

2.3.4 Dependence on the normal damping force

As described in Section 2.2.2, we adopt the normal damping force to reduce the normal oscillations in addition to Wada et al. (2007). To confirm that this damping factor does not affect the simulation results, we set the damping factor k_n as a parameter. Figure 2.7 shows dependence of pressure on the normal damping factor k_n. The fixed parameters are $N = 16384$ $C_v = 3 \times 10^{-7}$, and $\xi_{crit} = 8$ Å. Each line represents the result of one run for $k_n = 0, 10^{-2}$, and 10^{1}, respectively. This figure clearly shows that the normal damping force does not affect the simulation results.

As mentioned in Section 2.3.1, the compressive strength in the low-density region ($\phi \lesssim 0.1$) is expected to be determined by the rolling motion. To confirm this, we calculate the total energy dissipations of all motions, which are normal damping, rolling, sliding, and twisting. Figure 2.8 shows the dissipated energy for each mechanism, the dissipated energies in the case without the normal damping and those in the case of $k_n = 0.01$.

The dissipated energy in the case of $k_n = 10$ is indistinguishable from those in the case of $k_n = 0.01$, and thus we do not plot them. The dissipation energy of the sliding force is less than 10^{-9} erg, so it is not depicted in this figure. The dissipation by the rolling and twisting is almost the same in the cases with and without the normal damping. Thus, we confirm that the normal damping does not affect the compressive strength, although it dissipates the energy of the normal oscillations. Aside from the normal dissipation, the dominant dissipation mechanism is the rolling motion. This clearly shows that the static compression is determined by the rolling motion of each connection, as mentioned in Section 2.3.1. Where $\phi \gtrsim 0.1$, the energy dissipation by twisting motion occurs. This is why Equation (2.25) is valid until the filling factor reaches 0.1 as mentioned in Section 2.3.1. In the high-density region, where $\phi \gtrsim 0.1$, another formulation is required but that is beyond the scope of this paper.

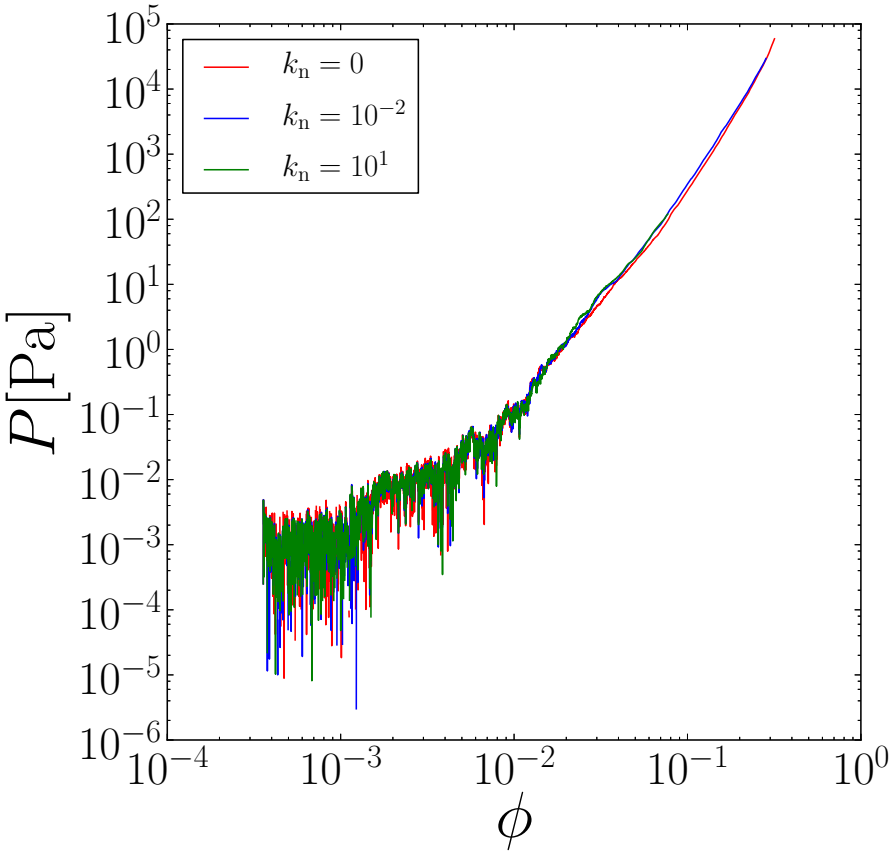

Fig. 2.7 Pressure P in [Pa] against filling factor ϕ with different normal damping force. We put the same ten initial conditions varying the normal damping force with $k_n = 0$, $k_n = 10^{-2}$, and $k_n = 10^{1}$. Each line shows the result of one run. The other parameters are $N = 16384$, $C_v = 3 \times 10^{-7}$, and $\xi_{crit} = 8$ Å.

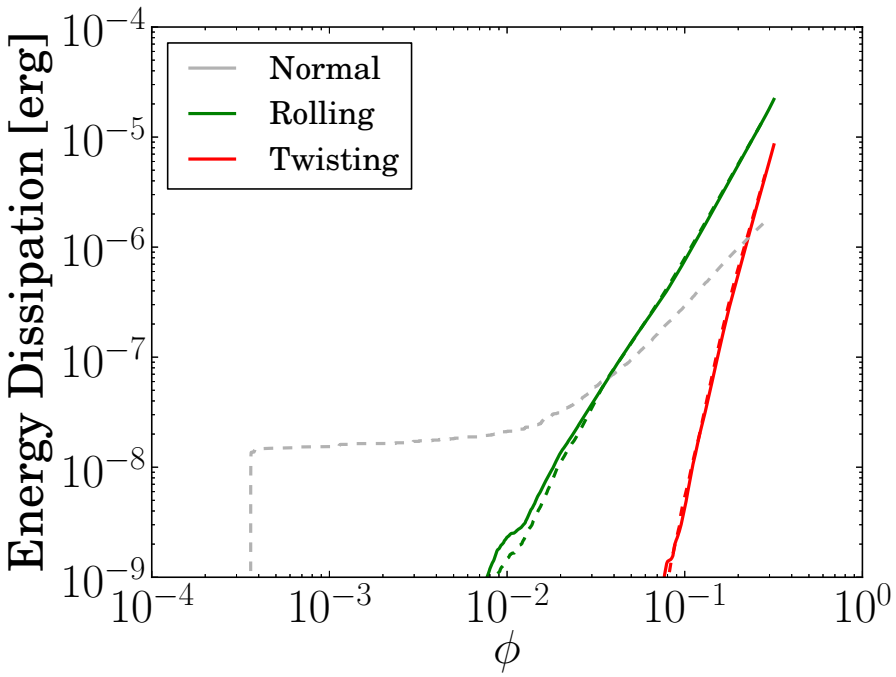

Fig. 2.8 Energy dissipation of each dissipation mechanism in [erg] against filling factor ϕ. The solid lines show the result in the case without the normal damping and the dashed lines in the case of $k_{\rm n} = 0.01$ The other parameters are the same as the fiducial run. The results in the case of $k_{\rm n} = 10$ are not plotted because they are the same as those in the case of $k_{\rm n} = 0.01$ and indistinguishable. The dissipation mechanisms are normal damping, rolling, sliding, and twisting. The dissipation energy by sliding motion is less than 10^{-9} erg,

2.3.5 Dependence on the rolling energy

We also investigate the dependence of the compressive strength on ξ_{crit}. Since E_{roll} is proportional to ξ_{crit}, we investigate the dependence on the rolling energy in this section. Figure 2.9 shows the dependency on ξ_{crit}. We vary ξ_{crit} with 32, 16, 8, 4, and 2 Å. The fixed param-

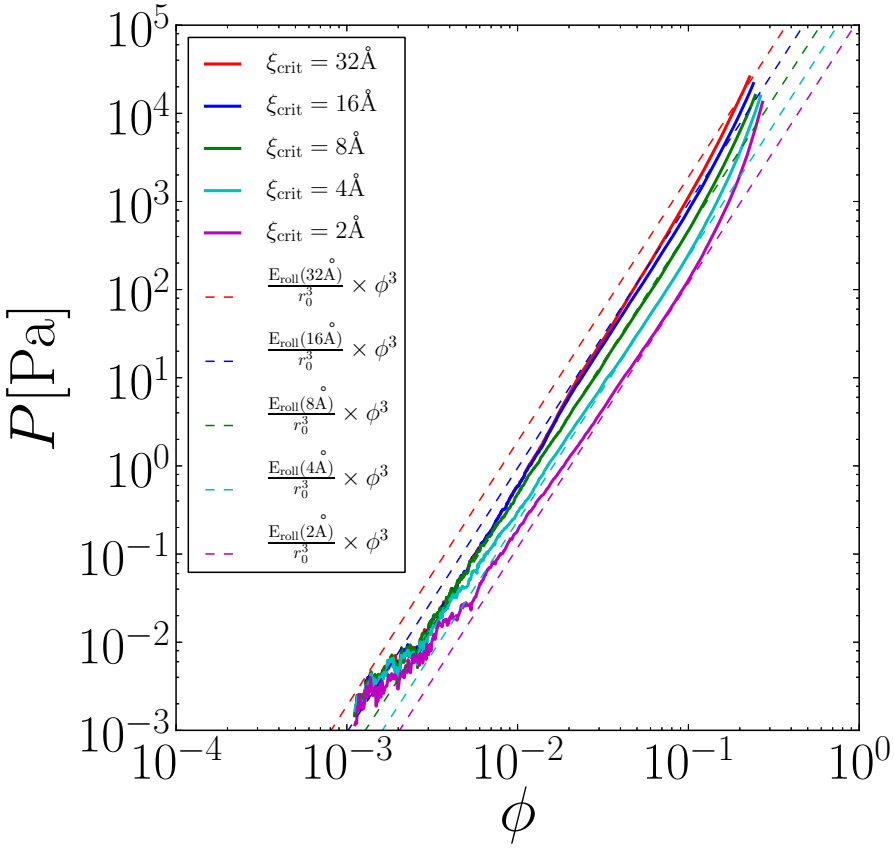

Fig. 2.9 Pressure P in [Pa] against filling factor ϕ with different critical displacement, ξ_{crit}. We put the same ten initial conditions varying ξ_{crit} with $\xi_{\mathrm{crit}} = 32, 16, 8, 4$, and 2 Å, respectively. Each line shows the average of ten runs. The other parameters are $N = 16384$ $C_{\mathrm{v}} = 3 \times 10^{-7}$, and $k_{\mathrm{n}} = 10^{-2}$.

eters are $N = 16384$, $C_{\mathrm{v}} = 3 \times 10^{-7}$, and $k_{\mathrm{n}} = 10^{-2}$. This result shows that the compressive strength is almost the same in the low-density region. This is because the periodic boundary creates the additional voids as discussed in Section 2.3.1, so we should not focus on the low-density region. The lines in the case of $\xi_{\mathrm{crit}} = 2, 4$, and 8 Å are on the corresponding lines of Equation (2.25) where $\phi \lesssim 0.1$. The line in the case of $\xi_{\mathrm{crit}} = 16$ Å has a little deviation, and in the case of $\xi_{\mathrm{crit}} = 32$ Å it has a deviation from their corresponding lines of Equation (2.25). The reason the lines in the case of $\xi_{\mathrm{crit}} = 16, 32$ Å deviate from the corresponding

lines of Equation (2.25) is that the dissipation energy is dominated not by rolling motion but by a twisting motion as indicated in Figure 2.10. This figure shows that dissipated energy of each dissipation mechanism. We show the results of the cases with $\xi_{\rm crit}$ = 8, 16, and 32 Å. The normal damping is not contribute to the compressive strength as discussed in Section 2.3.4, and thus we focus on the rolling and twisting motions.

When $\xi_{\rm crit} \leq 8$Å, the dissipation energy is dominated by rolling motion. For $\xi_{\rm crit} = 32$Å, on the other hand, the dissipation energy is dominated by a twisting motion. For $\xi_{\rm crit} = 16$Å, the dissipation energy of rolling and twisting motion is comparable, and making it the marginal case. Thus, the reason Equation (2.25) is not valid when $\xi_{\rm crit} \geq 16$Å is that the twisting motion is the dominant mechanism for determining the compressive strength. Therefore, we conclude that Equation (2.25) is valid when $\xi_{\rm crit} \leq 8$Å.

2.3.6 Fractal structure

We also investigate how the fractal structure of the dust aggregate changes. Figure 2.11 shows how many particles are inside the distance $r_{\rm in}$ for four snapshots. We select one run from the case with $N = 16384$, $C_{\rm v} = 3 \times 10^{-7}$, $k_{\rm n} = 10^{-2}$, and $\xi_{\rm crit} = 8$ Å. Each snapshot is when $\phi = 0.003, 0.01, 0.03$ and 0.1, respectively. We take a particle as an origin and count the number of particles inside $r < r_{\rm in}$, where r is the length from the origin. Then we set the computational region as an origin for all the other particles inside and take an average of them. We obtain the same trend in several runs in the cases of different shapes of initial aggregates.

We also count particles beyond the periodic boundaries. In high $r_{\rm in}$, $N \propto r_{\rm in}^3$ because of copies over the periodic boundary distributed as a fractal dimension of three. Therefore, where $N(r < r_{\rm in}) \gtrsim 16384$, N must be $N \propto r_{\rm in}^3$. However, it is almost out of the range of Figure 2.11. Figure 2.11 shows the number of particles in calculation, which is $N = 16384$. The results over this line are affected by the periodic boundary condition and those below this line is in computational region. Thus, the results below the line represents the fractal structure inside the computational region and are not the artificial effect of the periodic boundary condition.

Since the initial aggregate is a BCCA cluster, N is proportional to $r_{\rm in}^2$. In the case of $\phi = 0.003$, which is equivalent to ϕ of the initial BCCA cluster, $N \propto r_{\rm in}^2$ as shown in Figure 2.11. When the fractal dimension is three, N can be written as

$$N(r < r_{\rm in}) = \frac{\phi V(r < r_{\rm in})}{V_0} = \phi \left(\frac{r_{\rm in}}{r_0} \right)^3 , \tag{2.29}$$

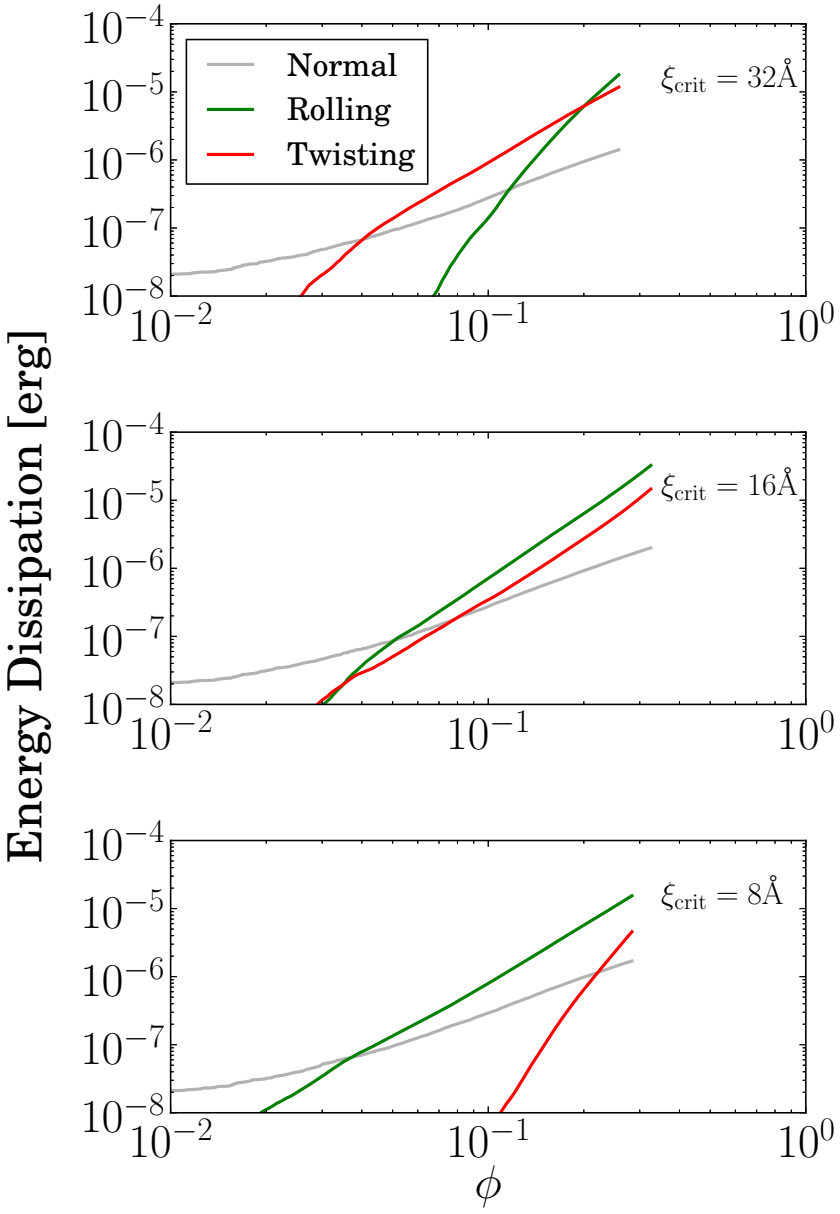

Fig. 2.10 Energy dissipation of each dissipation mechanism in [erg] against filling factor ϕ. Each panel represents the case of different ξ_{crit}, which are 32, 16, and 8 Å, corresponding to Figure 2.9.

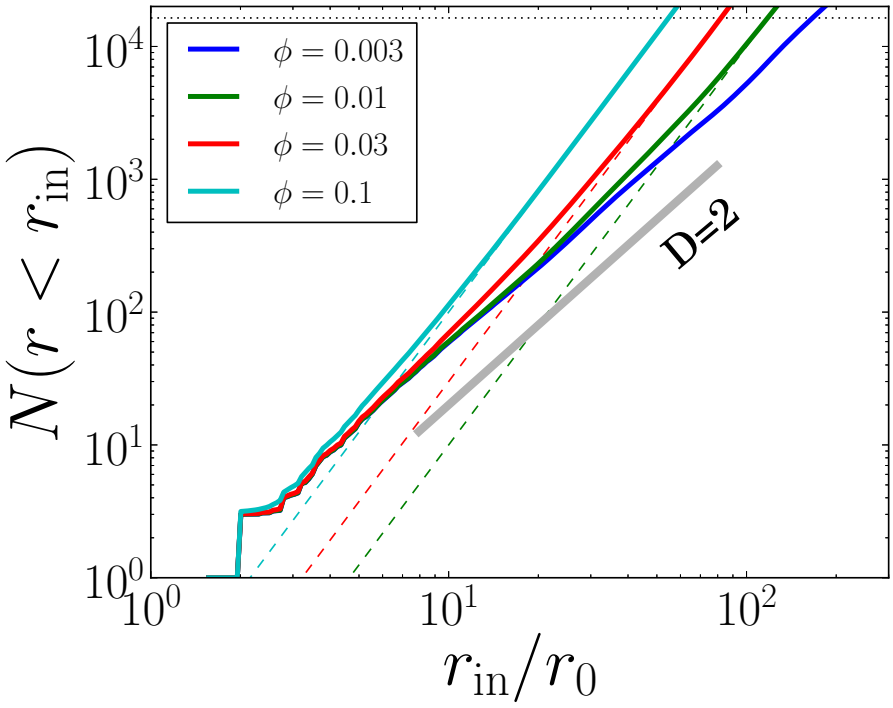

Fig. 2.11 Number of particles inside the radius $r_{\rm in}$ against normalized radius $r_{\rm in}/r_0$. This figure represents the fractal structure of the compressed aggregates in our simulation for various ϕ. We set a particle as an origin and count the number of particles inside $r < r_{\rm in}$, where r is the distance from the origin to each particle's center. Then we count the same correlation of all particles as an origin and take their average (similar figure of Figure.7 in the paper of Wada et al. (2008)). Each line shows the result at the different time steps. The solid thick lines represents the structure of fractal dimension $D = 2$, and dashed lines represent $D = 3$ for each corresponding ϕ. The dotted line shows the number of particles in calculation. The region below this line corresponds to inside the periodic boundaries.

where $V(r < r_{\rm in}) = (4/3)\pi r_{\rm in}^3$. We also plot this equation for each ϕ in Figure 2.11, with good agreement on a large scale, while maintaining $N \propto r_{\rm in}^2$ on a small scale.

Therefore, the structure evolution in the static compression is as follows. Initially, $N \propto r_{\rm in}^2$ because the aggregate is a BCCA cluster. As compression proceeds, the fractal dimension D becomes three on a large scale, while it is two on a small scale. The transit scale from $D = 2$ to $D = 3$ becomes smaller as compression proceeds until $D = 3$ on any scale. This structure evolution means that the static compression reconstructs the aggregate first on a large scale when keeping the small-scale BCCA structure. This is the reason the rolling motion determines the compressive strength, as discussed in Section 2.4.

2.3.7 Silicate case : Comparison with previous studies

The compressive strength has been investigated in the previous study (Seizinger et al., 2012). To investigate the connection of compressive strength from the low-density to the high-density regions, we perform simulations in the case of silicate with the same parameters of Seizinger et al. (2012). Figure 2.12 shows compression in the case of silicate whose monomer size is 0.6 μm. The parameters are $N = 16384$, $C_{\rm v} = 3 \times 10^{-7}$, and $k_{\rm n} = 0.01$.

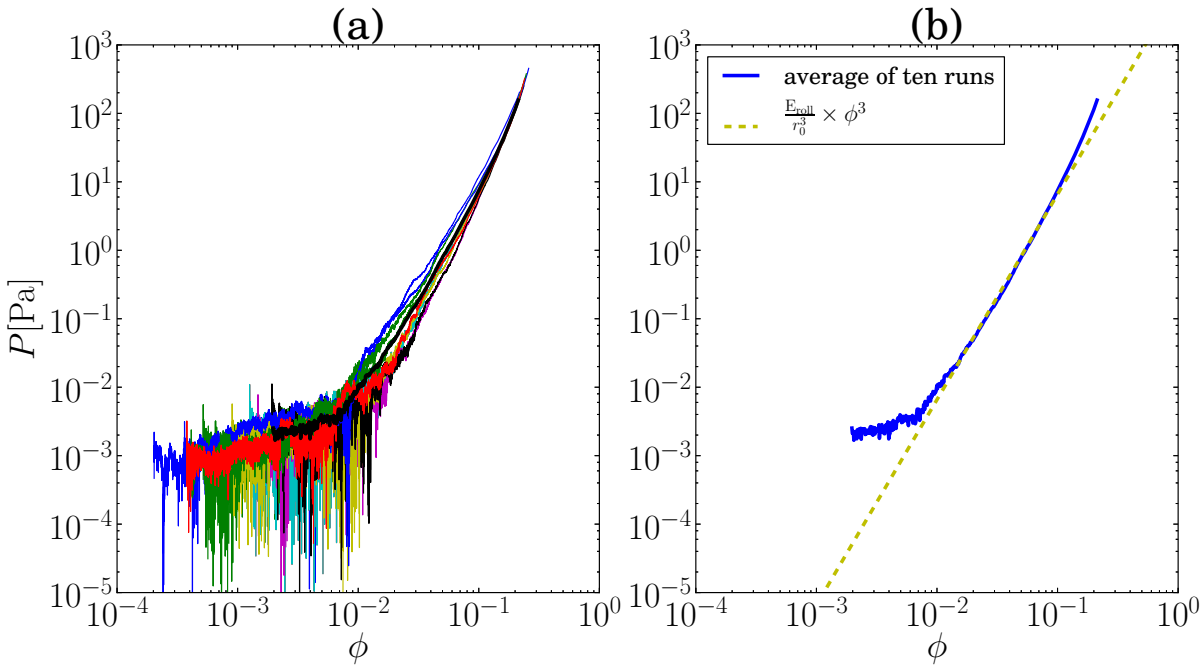

Fig. 2.12 Pressure P in [Pa] against filling factor ϕ. This figure is same as Figure 2.4 but for the case of silicate particles ($r_0 = 0.6\mu$m).

Figure 2.12(a) shows the results of ten runs with different initial aggregates and Figure 2.12(b) shows their average. Using the rolling energy of silicate, which is $E_{\rm roll} = 1.42 \times 10^{-8}$ erg, we also plot the line of Equation (2.25) in Figure 2.12(b). Since t_0 is given by 1.71×10^{-9} sec for silicate aggregates, $v_{\rm d}$ becomes 4.01 cm/s for $\phi = 10^{-2}$ with $C_{\rm v}$=3×10^{-7}. This $v_{\rm d}$ is larger than $c_{\rm s,eff}$ (= 0.77 cm/s when $\phi = 0.01$) for silicate aggregates, allowing the numerical results shown in Figure 2.12 to deviate from the line of Equation (2.25) in the low ϕ region. When $v_{\rm d} = c_{\rm s,eff}$, $\phi = 3.4 \times 10^{-2}$, the compressive strength should obey Equation (2.25) when $\phi \gtrsim 3.4 \times 10^{-2}$. In the case of silicate, computational time is huge compared with ice particles. We take a relatively high value of the boundary speed to save on computational time. Therefore, the result deviates from Equation (2.25) in the low-density region because of the high velocity. In other words, the compression is not static in the low density region. In the high-density region, on the other hand, the result is in good agreement with Equation (2.25), suggesting that Equation (2.25) is applicable to aggregates consisting of silicate particles with different r_0.

Figure 2.13 compares our simulation results and Equation (2.25) in the low-density region ($\phi < 0.1$) with the results of Seizinger et al. (2012) and the fitting formula to experiments (Güttler et al., 2009). This figure corresponds to Figure 4 in Seizinger et al. (2012). They performed similar N-body simulations to ours but using a BPCA aggregate composed of silicate particles as an initial condition. The compressive strength of our simulations shows good agreement with the same interaction model in Seizinger et al. (2012) with a little discrepancy: $\phi = 0.24$ at $P = 300$ Pa in our simulations and $\phi = 0.21$ at $P = 300$ Pa in Seizinger et al. (2012). The discrepancy, 13% in ϕ, may be caused by the difference in the initial aggregate or the pressure measurement method. The fitting formula of Güttler et al. (2009) suggests $\phi = 0.17$ at $P = 300$ in the experiments. The discrepancy from our simulations is 29 % in ϕ. In applicable uses of the static compression formula, we focus on obtaining ϕ with a given P.

2.4 Understanding the compressive strength formula

In this section, we analytically derive the compressive strength and confirm Equation (2.25). First, we consider the structure of a fluffy aggregate in static compression in our simulations. As described in Section 2.2.3, we adopt the periodic boundary condition and put a BCCA cluster as the initial condition. This corresponds to a large aggregate that filled up with BCCA clusters three dimensionally. As compression proceeds, the initial BCCA cluster is compressed but the aggregate keeps smaller BCCA structure as confirmed in Section 2.3.6.

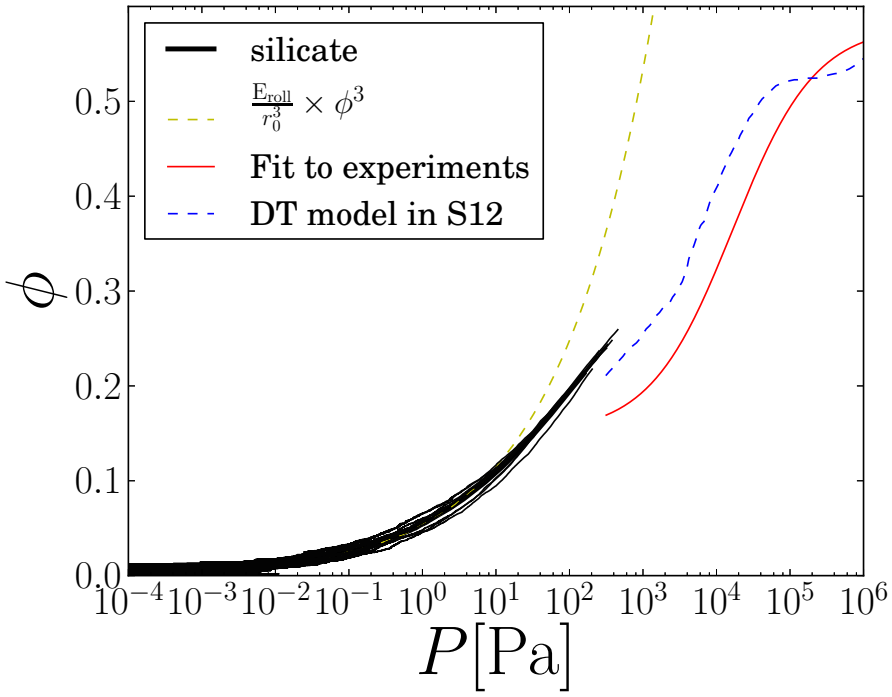

Fig. 2.13 The filling factor ϕ against pressure P in [Pa]. This figure is same as Figure 2.12, but plotted with a linear scale of ϕ and reversal of xy axis to compare with previous studies (see Figure 4 in Seizinger et al. (2012)). The dotted line is the result of numerical simulations in the high-density region ($\phi \gtrsim 0.1$) in Seizinger et al. (2012) and the thin solid line is the fitting formula proposed by Güttler et al. (2009). Our results consistently connect to the previous simulations in the high-density region.

Therefore, the aggregate in static compression always consists of BCCA clusters on some scale and filled up with them. Figure 2.14 illustrates the aggregate in static compression. The enclosed lines depict BCCA clusters on a small scale.

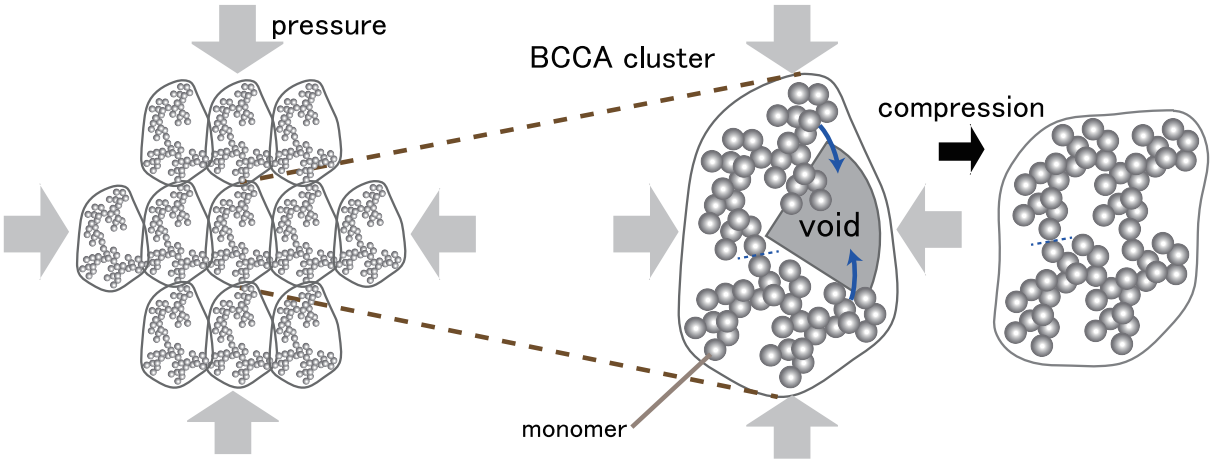

Fig. 2.14 Schematic drawing of compression of a dust aggregate consisting of a number of BCCA clusters. The left figure shows a dust aggregate consisting of many BCCA clusters and the BCCA clusters are distributed three dimensionally. Each enclosed line represents each region dominated by the BCCA clusters. The central figure is a BCCA cluster, receiving pressure from the next clusters. The BCCA cluster has a large void depicted in the central figure, and thus the void would be compressed, as expressed in the right figure. The required energy to compress the void is the energy to rotate the connection of monomers in contact. Therefore, the compression can be determined by the rolling motion of monomer connection on the connecting point of the subclusters.

Next, we consider why the compressive strength can be determined by the rolling energy. The internal mass density and the volume filling factor of the aggregate are equal to those of the BCCA clusters. Compression of the whole aggregate proceeds by compression of each cluster. Therefore, the compressive strength of the whole aggregate would be determined by BCCA clusters. The righthand panel of Figure 2.14 illustrates compression of one of BCCA clusters. The pressure on the BCCA cluster is exerted by neighbor clusters, which causes the compression of the BCCA cluster. The BCCA cluster can be divided further into two smaller subclusters because BCCA clusters are created by cluster-cluster aggregation. A large void exists between the two smaller clusters, and they are connected with one connection of monomers in contact. The compression of the BCCA cluster occurs by crashing the large void, which only requires rolling the monomers at the connection.

We now estimate the compressive strength. In static compression, the aggregate is compressed by external pressure. Each BCCA cluster feels a similar pressure, P. Using the

pressure, the force on the BCCA cluster is approximately given by

$$F \sim P \cdot r_{\mathrm{BCCA}}^2. \tag{2.30}$$

Since the crashing of the large void is accompanied by the rolling of a pair of monomers in contact, the work required for the crashing is given by so-called the rolling energy of monomers, E_{roll} (Dominik & Tielens (1997) or see Equation (2.1) for its definition). Therefore, the required force to compress the aggregate satisfies

$$F \cdot r_{\mathrm{BCCA}} \sim E_{\mathrm{roll}}. \tag{2.31}$$

Substituting Equation (2.30), we further obtain the required pressure to compress the aggregate as

$$P \sim \frac{E_{\mathrm{roll}}}{r_{\mathrm{BCCA}}^3}. \tag{2.32}$$

The radius of the BCCA clusters can be written by using the physical values of the whole aggregate. The internal density of the BCCA cluster is dependent on its radius. The BCCA cluster has the fractal dimension of two, and its radius is approximately given by $r_{\mathrm{BCCA}} = N^{1/2} r_0$, where N is the number of constituent monomers in the BCCA subcluster. The internal density of the BCCA cluster is evaluated as

$$\rho \sim \frac{N m_0}{r_{\mathrm{BCCA}}^3} \sim \left(\frac{r_{\mathrm{BCCA}}}{r_0} \right)^{-1} \rho_0. \tag{2.33}$$

Using equations (2.32) and (2.33), we finally obtain the required pressure (or the compressive strength) as

$$P \sim \frac{E_{\mathrm{roll}}}{r_0^3} \left(\frac{\rho}{\rho_0} \right)^3. \tag{2.34}$$

This is the same as Equation (2.25) obtained from our numerical simulations.

In addition, the discussion above is applicable to the case that the constituent cluster is not BCCA but sub-clusters which have a fractal dimension of D_f. In this case, the subcluster radius is described as $r_{\mathrm{cluster}} = N^{1/D_f} r_0$. Thus, the internal density is

$$\rho \sim N^{1-3/D_f} \rho_0 \sim \left(\frac{r_{\mathrm{cluster}}}{r_0} \right)^{D_f(1-3/D_f)} \rho_0. \tag{2.35}$$

Therefore, the compressive strength in the case that the sub-cluster has a fractal dimension

of D_f is written as

$$P \sim \frac{E_{\rm roll}}{r_0^3}\left(\frac{\rho}{\rho_0}\right)^{-3/D_f(1-3/D_f)}. \tag{2.36}$$

2.5 Summary

We investigated the static compressive strength of highly porous dust aggregates, whose filling factor ϕ is lower than 0.1. We performed numerical N-body simulations of static compression of highly porous dust aggregates. The initial dust aggregate is assumed to be a BCCA cluster. The particle-particle interaction model is based on Dominik & Tielens (1997) and Wada et al. (2007). We introduced a new method for compression and adopted the periodic boundary condition in order to compress the dust aggregate uniformly and naturally. Because of the periodic boundary condition, the dust aggregate in the computational region represents one part of a large aggregate, and thus we could investigate the compression of a large aggregate. The periodic boundaries move toward the center, and the distance between the boundaries becomes small. To measure the pressure of the aggregate, we adopted a similar manner to the one used in molecular-dynamics simulations. As a result of the numerical simulations, our main findings are as follows.

- The relation between the compression pressure P and the filling factor ϕ can be written as

$$P = \frac{E_{\rm roll}}{r_0^3}\phi^3, \tag{2.37}$$

  where $E_{\rm roll}$ is the rolling energy of monomer particles and r_0 the monomer radius. We defined the filling factor as $\phi = \rho/\rho_0$, where ρ is the mass density of the whole aggregate, and ρ_0 is the material mass density. Equation (2.37) is independent of the numerical parameters: the number of particles, the size of the initial BCCA cluster, the boundary speed, and the normal damping force. We confirmed that Equation (2.37) is applicable in different $E_{\rm roll}$ and r_0. We also analytically confirmed Equation (2.37).

- Equation (2.37) is valid where $\phi \lesssim 0.1$ in the high-density region. In the low-density region, we confirmed that Equation (2.37) is valid for $\phi \gtrsim 10^{-3}$ in the case of $N = 16384$. From the results of different initial sizes of the aggregates, Equation (2.37) is valid in the lower density region in the case of the larger aggregates.

- The initial BCCA cluster has a fractal dimension of two in the radius of the cluster, although the whole aggregate has a fractal dimension of three because of the periodic

boundary. As compression proceeds, the fractal dimension inside the radius of the initial BCCA cluster becomes three, while the fractal dimension on a smaller scale keeps being two. This means that the initial set up, which is that the fractal dimension on a large scale is three and that on a small scale is two, reproduce the structure of a dust aggregate well in static compression as a consequence. This also supports the compressive strength being determined by BCCA structure on a small scale.

- The static compression in the high-density region ($\phi \gtrsim 0.1$) has been investigated in the silicate case in previous studies (Seizinger et al., 2012). We performed the numerical simulations in the silicate case and confirmed that our results are consistent with those of previous studies in the high density region.

The compressive strength formula allowed us to study how static compression affects the porosity evolution of dust aggregates in protoplanetary disks. In applications to dust compression in protoplanetary disks, we use the compressive strength formula to obtain ϕ with a given P. Moreover, the obtained compressive strength would be applicable to SPH simulations of dust collisions. This application of the static compression process is important future work. In this work, we did not study shear or tensile strengths, but they are also worth investigating in future work.

Chapter 3

Planetesimal formation via fluffy aggregates

A part of this chapter has been published as Kataoka, A., Tanaka, H., Okuzumi, S., & Wada, K. 2013b, A&A, 557, L4 (Kataoka et al., 2013b).

Several barriers have been proposed in planetesimal formation theory: bouncing, fragmentation, and radial drift problems. Understanding the structure evolution of dust aggregates is a key in planetesimal formation. Dust grains become fluffy by coagulation in protoplanetary disks. However, once they are fluffy, they are not sufficiently compressed by collisional compression to form compact planetesimals. We aim to reveal the pathway of dust structure evolution from dust grains to compact planetesimals. Using the compressive strength formula, we analytically investigate how fluffy dust aggregates are compressed by static compression due to ram pressure of the disk gas and self gravity of the aggregates in protoplanetary disks. We reveal the pathway of the porosity evolution from dust grains via fluffy aggregates to form planetesimals, circumventing the barriers in planetesimal formation. The aggregates are compressed by the disk gas to a density of $10^{-3}\mathrm{g/cm^3}$ in coagulation, which is more compact than is the case with collisional compression. Then, they are compressed more by self-gravity to $10^{-1}\mathrm{g/cm^3}$ when the radius is 10 km. Although the gas compression decelerates the growth, the aggregates grow rapidly enough to avoid the radial drift barrier when the orbital radius is $\lesssim 6$ AU in a typical disk. We propose a fluffy dust growth scenario from grains to planetesimals. It enables icy planetesimal formation in a wide range beyond the snowline in protoplanetary disks. This result proposes a concrete initial condition of planetesimals for the later stages of the planet formation.

3.1 Introduction

Planetesimals, the seeds of planets, are believed to form by coagulation of dust grains in protoplanetary disks. How micron-sized dust grains grow to kilometer-sized planetesimals has been an unsolved problem in the complete planet formation theory; the intermediate-sized bodies are believed to be poorly sticky (Zsom et al., 2010), easily disrupted by collisions (Blum & Wurm, 2008), or liable to fall quickly onto the central star (Adachi et al., 1976; Weidenschilling, 1977).

Several possibilities have been proposed to overcome these barriers (Garaud et al., 2013; Johansen et al., 2007; Lambrechts & Johansen, 2012; Pinilla et al., 2012; Ros & Johansen, 2013; Windmark et al., 2012a). However, there has not yet been any coherent scenario explaining planetesimal formation from dust grains that avoids all of the barriers.

The internal structure evolution is a key to understanding how dust coagulation forms planetesimals. Figure 3.1(a) and (b) show the schematic diagram of the structure evolution previously considered. Dust grains become porous aggregates composed of sub-micron monomer particles by coagulation in protoplanetary disks, as illustrated in Fig.3.1(a) (Blum & Wurm, 2000; Kempf et al., 1999; Krause & Blum, 2004; Meakin, 1991; Paszun & Dominik, 2006; Smirnov, 1990). When the dust aggregates become massive, they are gradually compacted or disrupted in dust-dust collisions because of the increase in the impact energy, as illustrated in Fig.3.1(b)(Dominik & Tielens, 1997; Okuzumi et al., 2012; Paszun & Dominik, 2008, 2009; Suyama et al., 2008, 2012; Wada et al., 2007, 2008, 2009).

Growth via fluffy aggregates has been proposed to be one possible scenario to overcome the barriers in Okuzumi et al. (2012). They have shown that fluffy aggregates rapidly coagulate to avoid the radial drift problem. On the other hand, although the aggregates are compressed by dust-dust collisions, their internal density remains $\rho \sim 10^{-5}\mathrm{g/cm^3}$ (Okuzumi et al., 2012; Suyama et al., 2008). This is not consistent with the fact that planetesimals are believed to have $\rho \sim 0.1\mathrm{g/cm^3}$ as well as comets, the remnants of planetesimals (A'Hearn, 2011). Therefore other mechanisms to compress the fluffy aggregates are required.

In this paper, we introduce the static compression of aggregates due to ram pressure of the disk gas and self-gravity in protoplanetary disks, as illustrated in Fig.3.1(c) and (d). We use the compressive strength of porous aggregates numerically derived by Kataoka et al. (2013a) to obtain the porosity (equivalent to the internal density) of dust aggregates. We show how much the dust aggregates are compressed by the disk gas and by self-gravitational compression in their growth. Moreover, we investigate whether the growth is rapid enough to avoid the radial drift barrier by comparing the dust growth and radial drift timescale.

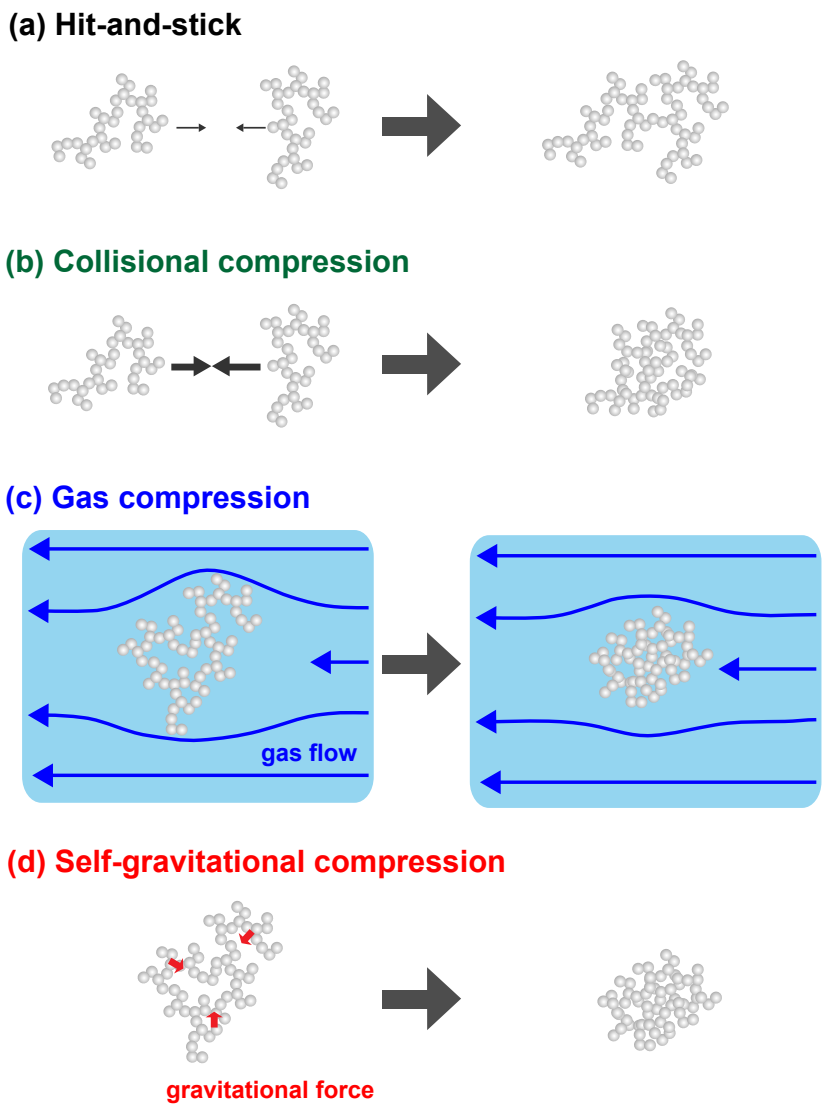

Fig. 3.1 Schematic drawing to illustrate dust growth via fluffy aggregates. (a) The dust aggregate hits another aggregate to be stick. This reduces dust density and occurs in a very early stage of dust growth. (b) When the collisional speed is high enough to disrupt the dust aggregates, they are compressed. (c) Dust aggregates have a velocity difference against gas, and they feel the ram pressure by the gas. The ram pressure statically compresses the dust aggregates. (d) When the dust aggregates become so massive that they do not support their structure, they are compressed by their own self-gravity.

3.2 Method: introducing static compression to planetesimal formation

The compressive strength of a highly porous dust aggregate, P, is given by (Kataoka et al., 2013a)

$$P = \frac{E_{\rm roll}}{r_0^3}\left(\frac{\rho}{\rho_0}\right)^3, \tag{3.1}$$

where ρ is the mean internal density of the dust aggregate, r_0 the monomer radius, ρ_0 the material density, and $E_{\rm roll}$ the rolling energy, which is the energy for rolling a particle over a quarter of the circumference of another particle (Dominik & Tielens, 1997; Wada et al., 2007). In this paper, we adopt $\rho_0 = 1.0$ g/cm^3, $r_0 = 0.1$ μm, and $E_{\rm roll} = 4.74 \times 10^{-9}$ erg , which correspond to icy particles. $E_{\rm roll}$ is proportional to the critical displacement, which has an uncertainty from 2 Å to 30 Å (Dominik & Tielens, 1997; Heim et al., 1999). For later discussion, we note that the dust density is proportional to $E_{\rm roll}^{1/3}$ and thus the uncertainty little affects the resulting dust density.

When a dust aggregate feels a pressure that is higher than its compressive strength, the aggregate is quasi-statically compressed until its strength equals the pressure. We define the dust internal density where the compressive strength equals a given pressure as an equilibrium density $\rho_{\rm eq}$. Using Eq.(3.1), we obtain $\rho_{\rm eq}$ as

$$\rho_{\rm eq} = \left(\frac{r_0^3}{E_{\rm roll}}P\right)^{1/3}\rho_0. \tag{3.2}$$

We consider a source of the pressure to be ram pressure of the disk gas or self-gravity of the aggregate.

We obtain ram pressure of the disk gas as follows. We consider a dust aggregate of mass m and radius r, which is moving in the disk gas with velocity v against the gas. The pressure $P_{\rm gas}$ against the aggregate can be defined as the gas drag force divided by the geometrical cross section: $P_{\rm gas} \equiv F_{\rm drag}/A$, where $F_{\rm drag} = mv/t_{\rm s}$, $A = \pi r^2$, and $t_{\rm s}$ is the stopping time of the aggregate. While the pressure has both compressive and tensile components, we assume that the pressure is compressive. Thus, we obtain the pressure as

$$P_{\rm gas} = \frac{mv}{\pi r^2}\frac{1}{t_{\rm s}}. \tag{3.3}$$

The typical gas drag law is adopted to obtain $t_{\rm s}$ and v. The gas drag law is the Epstein regime, when the dust radius is less than 4/9 times the mean free path of gas. On the

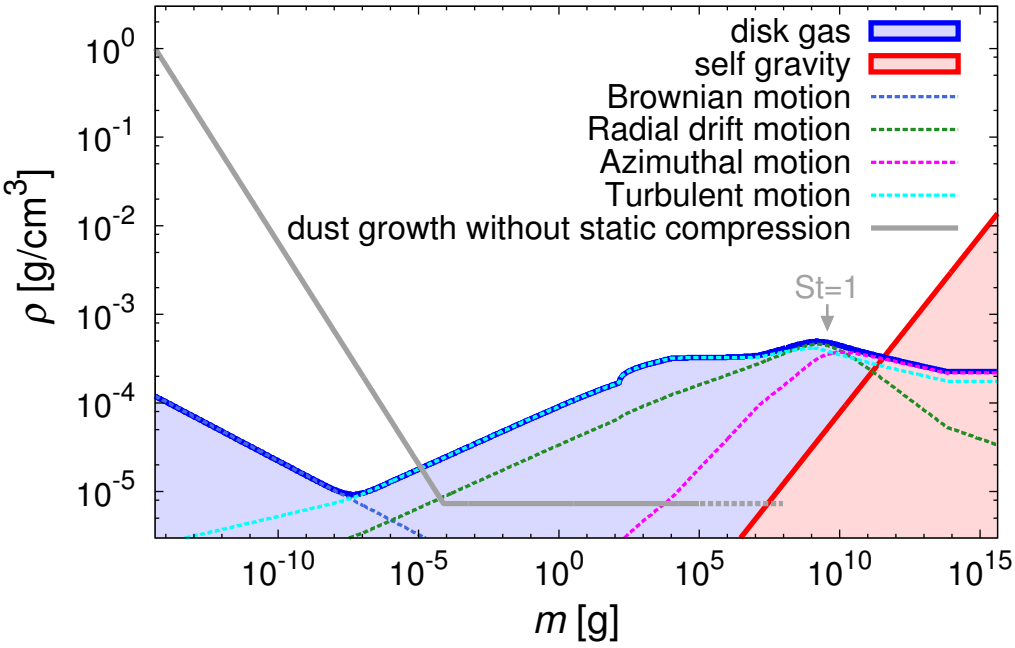

Fig. 3.2 Equilibrium dust density at 5AU in an MMSN disk. The blue thick solid line represents the equilibrium density of gas pressure, where the ram pressure of gas is equal to the compressive strength of the dust aggregate. The thin dotted lines represent the component of gas ram pressure, which is induced by the velocity difference between gas and dust, such as Brownian motion, radial drift motion, azimuthal motion, and turbulent motion. The red solid line represents the equilibrium density of self-gravity. The blue and red shaded region represents where the compressive strength of the dust aggregate is lower than the pressure of gas or self-gravity, so these aggregates are compressed until their density becomes the equilibrium density. We also plot the dust growth path without static compression (Okuzumi et al., 2012).

other hand, it is the Stokes regime if the Reynolds number is less than unity (see Eq.(4) in Okuzumi et al. (2012), for example). When the Reynolds number exceeds unity, the gas drag law changes as a function of Reynolds number (see Eq.(8a) to Eq.(8c) in Weidenschilling (1977)). The drag force is determined by the relative velocity of the gas and dust. The relative velocity is induced by Brownian motion, radial drift, azimuthal drift, and turbulence. We use the closed formula of the turbulence model (Ormel & Cuzzi, 2007) and assume the turbulent parameter $\alpha_{\rm D} = 10^{-3}$, except for the strong turbulence case, where $\alpha_{\rm D} = 10^{-2}$.

We assume the minimum mass solar nebula (MMSN), which was constructed based on our solar system (Hayashi, 1981). At a radial distance R from the central star, the gas-surface density profile is $1700\ {\rm g/cm^2} \times (R/1{\rm AU})^{-1.5}$ and the dust-to-gas mass ratio is 0.01. The temperature profile adopted is $137\ {\rm K} \times (R/1{\rm AU})^{-3/7}$, which corresponds to midplane temperature (Chiang et al., 2001). This is cooler than optically thin disk models to focus on the dust coagulation in the midplane.

We also calculate the self-gravitational pressure as follows. Although the gravitational pressure has distribution in the aggregates, we simply assume a uniform pressure inside the aggregates. We define the force on the dust aggregates as $F = Gm^2/r^2$, and the area $A = \pi r^2$. Thus, the self-gravitational pressure is

$$P_{\rm grav} = \frac{Gm^2}{\pi r^4}. \tag{3.4}$$

We note that the equilibrium density of self-gravitational compression depends only on dust mass and internal density and not on the disk properties.

3.3 Results: planetesimal formation via fluffy aggregates

First, we calculate the equilibrium density of dust aggregates in a wide range in mass, where their compressive strength is equal to the gas or self-gravitational pressure. Figure 3.2 shows the equilibrium dust density against dust mass at 5 AU in the disk. If the gas or self-gravitational pressure is higher than the compressive strength, the dust aggregate is compressed to achieve the equilibrium density because the strength is higher in denser dust aggregates. In other words, the equilibrium density represents a lower limit of the dust density in the disk. We also plot the collisional growth path without static compression (Okuzumi et al., 2012); the dust aggregates initially grow with a fractal dimension of 2, and when the impact energy of dust-dust collisions reaches the rolling energy, the internal density becomes almost constant. The evolutional track should trace the higher density of

the growth with collisional compression and the equilibrium density of static compression. Therefore, we conclude that dust growth is initially fractal, and then the gas compression becomes effective before collisional compression occurs at 5 AU in the disk.

Figure 3.3 shows the pathways of the dust growth in mass-density space at 5 and 8 AU from the central star. Here, we assume that the dust aggregates have no mass or volume distribution. The first growth mode is hit-and-stick, where the fractal dimension is 2. As dust aggregates become massive, the gas compression becomes effective. Once gas compression occurs, the equilibrium density is higher in more massive aggregates until the Stokes number (i.e., the stopping time normalized by the orbital timescale) becomes unity; consequently, the aggregates always keep the equilibrium density in coagulation. The gas compression remains effective until the dust aggregates grow so massive that self-gravitational compression is more effective than gas compression. The self-gravitational compression is effective when the mass is $\sim 10^{11}$ g. Once the gravitational compression is effective, the density increases with the mass of the power of 2/5. However, the gas compression makes the dust density almost constant because of the constant velocity difference of the gas and dust of the head wind in azimuthal direction. Therefore, the final stage is determined by self-gravitational compression. We find that the dust aggregates should be compressed to a density of 0.1 g/cm^3 when their mass is $\sim 10^{18}$ g.

The density and mass of the final product are close to comets, which are considered to be the remnants of planetesimals. We also plot the properties of several comets that are well known in the density and mass in Fig. 3.3 (A'Hearn, 2011). The comets have a mass of $\sim 10^{16}$ g and an internal mass density of ~ 0.1 g/cm^3. There is a two-orders-of-magnitude discrepancy in mass between the final product of our calculation and the comets. The mass of comets would be finally determined by collisional fragmentation or melting of planetesimals.

We estimate the dust growth timescale by coagulation and the radial drift timescale. Assuming that aggregates have no mass or volume distribution, the growth time is defined as $m/\rho_{\rm d}\pi r^2\Delta v$, where $\rho_{\rm d}$ is the spatial mass density of dust aggregates and Δv is the velocity difference between the dust aggregates, which is assumed be the root mean square of Brownian motion and turbulent motion (see Eq. (32) in Okuzumi et al. (2012)). For the velocity induced by turbulence, we use the velocity difference of dust and gas as dust-dust velocity for simplicity. We include the dust sedimentation by considering the dust scaleheight (Brauer et al., 2008). The drift timescale is defined as the orbital radius divided by the radial drift velocity. We define the dust aggregates as where the drift timescale is less than 30 times the growth timescale drift to the central star (Okuzumi et al., 2012).

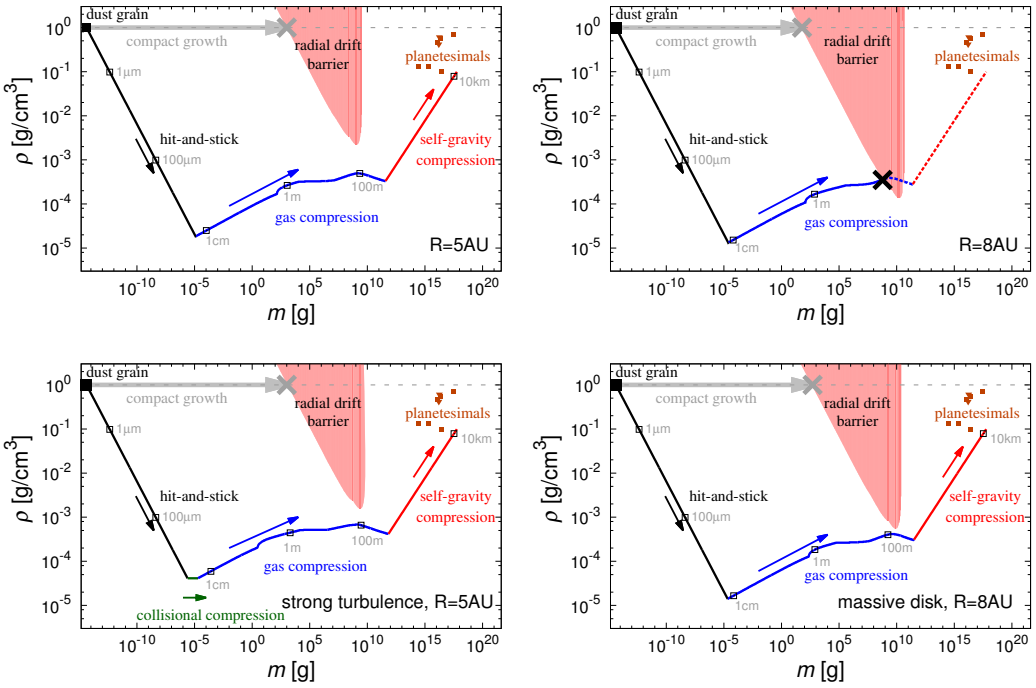

Fig. 3.3 Pathways in the planetesimal formation in the minimum mass solar nebula model. The gray line shows the constant density evolutional track, which corresponds to the compact growth. The black, green, blue, and red lines are the evolutional track through dust coagulation via fluffy aggregates. Each line represents different mechanisms of dust coagulation, which are hit-and-stick, collisional compression, gas compression, and self-gravity compression. The red shaded region represents where the radial drift timescale is less than the growth timescale, which is equivalent to radial-drift region. The brown squares indicate the properties of comets, and the triangles represent their upper limit. The radii of dust aggregates for 1 μm, 1 cm, 1 m, 100 m, and 10 km are also written. (Top left): for 5 AU in orbital radius. (Top right): for 8 AU in orbital radius. The cross point represents where the dust falls onto the central star. (Bottom left): for 5 AU in strong turbulence model where $\alpha_{\rm D} = 10^{-2}$. (Bottom right): for 8 AU in two times as massive as MMSN model.

We show that the revealed pathway still overcomes the radial drift problem. Figure 3.3 also illustrates the region where the dust aggregates radially drift inward before they grow. Even when the dust aggregates become massive and their Stokes number is unity, the dust growth time is still shorter than the drift at 5 AU. In the outer radius of the disk (e.g., at 8 AU), the dust aggregates drift inward before growth (top right of Fig. 3.3). However, if the disk is two times as massive as MMSN, the dust aggregates successfully break the radial drift problem (bottom right of Fig. 3.3). Therefore, the fluffy dust can grow to planetesimals more inside in protoplanetary disks.

Fluffy dust also breaks through the bouncing barrier. Solid bodies have been shown to bounce in some situations (Güttler et al., 2010). However, both numerical simulations and experiments have shown that highly porous aggregates do not bounce when $\phi \lesssim 0.15$ (Kothe et al., 2013; Langkowski et al., 2008; Seizinger & Kley, 2013; Wada et al., 2011). Thus, the bouncing is not a major difficulty for the growth of highly porous aggregates.

The fragmentation barrier is not a serious problem when considering icy particles. The dust aggregates are not significantly fragmented and grow through collisions as long as their collision velocity is < 60 m/s (Wada et al., 2009). The collisional velocity becomes maximum when the Stokes number is unity. It is the square root of $\alpha_{\rm D}$ times the sound speed of gas. In the case of $\alpha_{\rm D} = 10^{-3}$, the maximum velocity is ~ 17 m/s at 5AU, so the dust aggregates can avoid significant disruption. In the case of $\alpha_{\rm D} = 10^{-2}$, on the other hand, the velocity reaches ~ 54 m/s, comparable to the critical velocity. Thus, we should carefully discuss the fragmentation in strong turbulent disks. We note that the turbulent velocity is lower than the original MMSN model, where the temperature is determined by the balance between the stellar radiation and the reemission for each position. This is because we focus on the midplane, where the temperature is lower; thus the velocity is also lower than the irradiated surface.

However, when considering silicate particles, it is difficult to break through the fragmentation barrier. Inside the snowline, the ice is sublimated and the dominant material is silicate particles. The critical velocity of fragmentation of silicate is ~ 6 m/s (Wada et al., 2009). Thus, the silicate planetesimal formation is still an open question.

In the final stage of coagulation, the runaway growth begins. We estimate the dust mass where the dust-dust collision velocity induced by turbulence exceeds the escape velocity of the dust. When the dust becomes as massive as $\sim 10^{15}$ g, the runaway growth starts. The dust internal density is still as small as $\sim 10^{-2}$, which means that the geometrical cross section is larger than the compact case. This will make the runaway growth faster, but the whole scenario does not change, as shown in the N-body simulations (Kokubo & Ida, 1996).

3.4 Planetesimal-forming region

We have shown that the dust aggregates grow before falling onto the central star by comparing the growth and drift timescales at 5 AU and 8 AU. Here, we discuss overall picture of the coagulation and the radial drift of dust aggregates in a protoplantary disk. At the inner orbital radius such as 5 AU, dust aggregates can grow at almost the same orbital radius. At the outer orbital radius such as 8 AU, however, dust aggregates radially migrate when they grow as large as $m \sim 10^9$ g as shown in Fig. 3.3. Because the growth timescale is shorter than the drift timescale at smaller orbital radius, the aggregates can grow before falling onto the central star when the orbital radius becomes small enough to avoid the radial drift barrier.

Here, we define the critical orbital radius such that the growth timescale is shorter than the drift timescale for all mass range of dust aggregates. The overall picture is as follows. Dust grains that locate inside the critical orbital radius and outside the snowline form planetesimals with direct coagulation via fluffy dust aggregates. Dust grains outside the critical orbital radius start coagulation until their radial drift timescale becomes shorter than the growth timescale. Then, they radially migrate until the orbital radius becomes shorter than the critical orbital radius. Once they reach inside the critical radius, they grow again to form planetesimals. In the proposed scenario, therefore, planetesimal can form between the snowline and the critical radius.

The location of the snowline and the critical orbital radius depends on the disk model. In the adopted model in this paper, when the condensation temperature is set to be 170 K, the snowline locates at 0.65 AU, and the critical orbital radius is located at ~ 7 AU from Fig. 3.3. The parameter which determines the snowline is the temperature: the higher temperature of the disk, the larger orbital radius of the snowline. On the other hand, the main parameters which determine the location of critical orbital radius are the temperature and the disk mass: more massive and cooler disk is expected to have larger critical radius. The dependence of the planetesimal forming region on the disk parameters should be tested in future work.

The planetesimal distribution strongly affects the final locations of planets. In the proposed scenario, the orbital distribution of planetesimals is between the snowline and the critical orbital radius, which depends on the properties of the protoplanetary disk. Combining the proposed scenario and the planet formation theories from planetesimals, we will be able to reveal the formation process of our solar system and exoplanets.

3.5 Conclusions

Our main findings of this chapter are as follows:

- We introduced static compression of dust aggregates in protoplanetary disks. As sources of the compression, we considered gas-drag compression and self-gravity compression. By equalizing the compressive strength (Kataoka et al., 2013a) and pressure of the gas-drag and the self-gravity, we derived the equilibrium internal density of dust aggregates.

- Combining the initial fractal growth and the collisional compression model (Okuzumi et al., 2012), we revealed the overall filling factor evolution in dust coagulation in protoplanetary disks as follows. After the initial fractal growth, where the dust aggregates have the filling factor $\phi \sim 10^{-4}$, dust aggregates are compressed by the gas-drag pressure before the onset of the collisional compression. The aggregates coagulate further keeping the equilibrium filling factor with gas-drag pressure. When the aggregates obtain a mass of $\sim 10^{12}$ g, the self-gravity compression becomes effective and the aggregates form relatively compact ($\phi \sim 0.1$) objects. The filling factor and the mass of the final objects are similar to the expected properties of planetesimals.

- We have shown that on the pathway of the planetesimal formation, the dust aggregates avoid the radial drift barrier at a certain orbital radius. This is because the growth timescale is always shorter than the drift timescale. The region where the aggregates are free from the radial drift barrier is inside the critical orbital radius, which is the maximum radius where the growth timescale is always shorter than the drift timescale. The critical orbital radius is ~ 7 AU in the adopted model.

- The aggregates overcome the fragmentation barrier outside snowline because of the high critical velocity of catastrophic disruption of ice particles (Wada et al., 2013, 2009). The snowline in this paper located at 0.65 AU. The planetesimal formation inside the snowline is still an open question because of the fragmentation barrier of silicate particles. In addition, the aggregates do not face the bouncing barrier because of their fluffiness (Wada et al., 2008)

In conclusion, we revealed a pathway of the porosity evolution of dust aggregates to form planetesimals by introducing the static compression. We also showed that icy aggregate growth on the pathway is free from the radial drift, the fragmentation, and the bouncing barriers. The region of planetesimal formation is between the snowline and the critical

orbital radius, which are 0.65 AU and 7 AU in the adopted disk model. This scenario can provide the orbital distribution of planetesimals as a concrete initial condition of the later stages of planet formation.

Chapter 4

Opacity of fluffy dust aggregates

A part of this chapter has been published as Kataoka, A., Okuzumi, S., Tanaka, H., & Nomura, H., 2014, A & A, 568, A42 (Kataoka et al., 2014).

Dust grains coagulate to form dust aggregates in protoplanetary disks. Their porosity can be extremely high in the disks Although disk emission may come from fluffy dust aggregates, the emission has been modeled with compact grains, We aim to reveal the mass opacity of fluffy aggregates from infrared to millimeter wavelengths with the filling factor ranging from 1 down to 10^{-4}. We use Mie calculations with an effective medium theory. The monomers are assumed to be 0.1 μm sized grains, which is much shorter than the wavelengths that we focus on. We find that the absorption mass opacity of fluffy aggregates are characterized by the product $a \times f$, where a is the dust radius and f is the filling factor, except for the interference structure. The scattering mass opacity is also characterized by af at short wavelengths while it is higher in more fluffy aggregates at long wavelengths. We also derive the analytic formula of the mass opacity and find that it reproduces the Mie calculations. We also calculate the expected difference of the emission between compact and fluffy aggregates in protoplanetary disks with a simple dust growth and drift model. We find that compact grains and fluffy aggregates can be distinguished by the radial distribution of the opacity index β. The previous observation of the radial distribution of β is consistent with the fluffy case, but more observations are required to distinguish between fluffy or compact. In addition, we find that the scattered light would be another way to distinguish between compact grains and fluffy aggregates.

4.1 Introduction

Optical properties of dust grains have been investigated by many authors to understand the emission from various kinds of astronomical objects. In protoplanetary disks, dust grains are important not only as the emitter of radiation, but also as the seeds of planets. The size of dust grains increases by coagulation from submicron size to millimeter size or larger. A number of radio observations suggest that dust grains have been grown to millimeter-sized grains in protoplanetary disks (Andrews & Williams, 2005; Guilloteau et al., 2011; Isella et al., 2009; Ricci et al., 2010a,b; van der Marel et al., 2013).

The silicate feature at 10 μm is evidence of grain growth (e.g., van Boekel et al., 2005). The infrared observations suggest that the size of silicate dust grains is spreading from 0.1 μm to a few μm. The infrared emission is expected to come from the surface region of protoplanetary disks. Tiny grains are kinematically well coupled to the disk gas and thus stirred up to the disk surface. Thus, we do not obtain information of dust grains larger than the micron size from infrared observations. In addition, infrared scattered light images of protoplanetary disks are less luminous than expected from other observations. This may infer the presence of large compact grains or porous aggregates at the disk surface (Mulders et al., 2013).

The opacity index at submillimeter wavelengths is used as another clue of grain growth (Beckwith & Sargent, 1991; Beckwith et al., 1990; Miyake & Nakagawa, 1993). The most striking evidence of dust growth is the opacity index β, where $\kappa_\nu \propto \nu^\beta$; β is estimated from observed flux slope α, where $F_\nu \propto \nu^\alpha$. If the dust emission is optically thin, the dust slope has a relation of $\beta = \alpha - 2$. The index β is typically from 1 to 0 in protoplanetary disks, which means grain growth in protoplanetary disks (Andrews & Williams, 2005; Lommen et al., 2010; Pérez et al., 2012). The recent observations using radio interferometers have revealed the radial profile of β. Pérez et al. (2012) made a model fit of β and suggested that β is different between in the inner and outer part of the disk. Thus, the dust grains in the inner part of the disk are expected to grow to a larger size.

Although the protoplanetary disk emissions are usually modeled with compact dust grains, recent numerical simulations have shown that dust grains coagulate to form fluffy structure, especially in the case of icy dust aggregates. With low speed collisions, dust grains form fluffy aggregates. However, it has been shown that fluffy dust aggregate are not easy to be compressed. Wada et al. (2008) and Suyama et al. (2008, 2012) investigated collisional compression of icy dust aggregates, and Okuzumi et al. (2012) performed coagulation simulations including the collisional compression. They revealed that the initial

fractal growth stops when the collisional energy exceeds the rolling energy. They derived that the achievable lowest filling factor is $\sim 10^{-5}(m_{\rm roll}/10^{-4}\ {\rm g})$, where $m_{\rm roll}$ is the aggregate mass when the impact energy is equal to the rolling energy. Moreover, Kataoka et al. (2013a,b) introduced the static compression of dust aggregates. They showed that the filling factor decreases to as low as 10^{-4} even when considering the effects of the static compression. However, the porosity evolution of icy dust aggregates has not been confirmed by laboratory experiments yet.

The icy and fluffy aggregates are expected to overcome theoretical problems in planetesimal formation. Fluffy aggregates are expected to overcome the radial drift barrier (Kataoka et al., 2013b; Okuzumi et al., 2012) and the bouncing barrier (Wada et al., 2011). Moreover, if particles are composed of ice, the dust aggregates overcome the fragmentation barrier because they are sticky (Wada et al., 2013, 2009).

Dust coagulation has also been investigated in laboratory experiments. As an analog to silicate dust grains, which are expected to be dominated inside the snowline in protoplanetary disks, silica particles have been used in laboratory experiments. Conditions for bouncing and fragmentation have been studied in laboratory experiments (Blum & Wurm, 2008; Zsom et al., 2010) and some scenarios for planetesimal formation breaking through the bouncing barrier have been proposed (Drążkowska et al., 2013; Windmark et al., 2012a). From the viewpoint of porosity evolution, silicate dust aggregates are expected to be less fluffy than icy dust aggregates because the surface energy of silicate is lower than ice. Microgravity experiments have confirmed the hit-and-stick process of forming fluffy dust aggregates (Kothe et al., 2013). However, further growth concerning compression is still uncertain in laboratory experiments. Zsom et al. (2011) performed numerical simulations of dust coagulation of silicate particles, using the hit-and-stick model proposed by Okuzumi et al. (2009). They showed that the filling factor of dust aggregates can reach 10^{-3} before the onset of compaction. [1]

Observational constraints of porosity of dust aggregates in protoplanetary disks are important. However, studies of interpreting disk observations have assumed $f \geq 0.1$ (e.g., Birnstiel et al., 2010b), which is relatively compact compared with the extremely porous aggregates, whose filling factor is 10^{-4}, as discussed above. In this paper, as a first step to constrain the porosity of dust aggregates in protoplanetary disks, we investigate optical properties of dust aggregates including the extremely porous aggregates.

Opacity of porous aggregates has been investigated by several theoretical methods. In

[1] Zsom et al. (2010) obtained less fluffy aggregates than Zsom et al. (2011) because Zsom et al. (2010) adopted the porosity model proposed by Ormel et al. (2007), which is not as accurate as the model of Okuzumi et al. (2009).

the context of explaining cometary dust, scattering properties of BPCA and BCCA aggregates have been studied (Kimura et al., 2003, 2006; Kolokolova et al., 2007). The number of constituent particles was limited to ~ 60000 ($\sim 10^{-10}$ g in mass if the particle size is 0.1 μm), and the opacity was only studied at infrared wavelengths. In the context of explaining the interstellar silicate feature, in addition, the effects of monomer shapes on optical properties at infrared wavelength have been also studied (Min et al., 2003, 2005, 2007). In this paper, we examine the absorption and scattering mass opacities of dust aggregates at wavelengths ranging from 1 μm to 10 cm. The aggregates have a size ranging from micron to kilometer and a filling factor ranging from 1 to 10^{-4}.

One of the popular methods for calculating the mass opacity of porous aggregates is the discrete dipole approximation (DDA) (Draine & Flatau, 1994; Min et al., 2006). This calculation takes a huge computational time for large aggregates. To investigate the opacities of highly porous aggregates for a wide size range, the method would not be suitable. In this paper, we aim to reveal the mass opacity of fluffy aggregates from infrared to millimeter wavelengths with the filling factor ranging from 1 down to 10^{-4}. Thus, we use the effective medium theory (EMT). This method is fast in calculation but inaccurate in some parameters. Kozasa et al. (1992) have shown that EMT reproduces the absorption opacity of BCCA and BPCA clusters, whose constituent monomers are up to 1024, within a error of a factor of two. The EMT is also known to be accurate for porous aggregates whose constituent particles are small compared with the wavelength of incident radiation (Shen et al., 2008; Voshchinnikov et al., 2005). Because the dust aggregates considered in this paper are highly porous aggregates consisting of submicron-sized monomers, EMT would be a good approximation for calculations in this paper. We note that the scattering opacity derived with EMT largely deviates from the actual value in some parameter space (Shen et al., 2009). The accuracy of EMT in a large parameter space should be tested in the future work.

This paper is organized as follows. We describe the composition of dust grains and the calculating method of mass opacities in Section 4.2. We show the results of the absorption and scattering mass opacities of highly porous aggregates by using Mie theory with EMT in Section 4.3. We derive analytic formulae to reproduce the results in Section 4.4. Then, we construct a simple dust growth and drift model in protoplanetary disks and propose a method to distinguish compact and fluffy aggregates in radio observations by using the slope at millimeter wavelengths, the so-called dust β, in Section 4.5. Finally, we summarize and discuss the previous observations with porous aggregates in Section 4.6.

4.2 Method

Here, we briefly summarize the definitions of optical properties following Bohren & Huffman (1983, hereafter BH83) and Miyake & Nakagawa (1993). We consider a particle or an aggregate with radius a and internal mass density ρ. The radius of an aggregate represents the characteristic radius, defined as $a = \sqrt{5/3}a_{\rm g}$, where $a_{\rm g}$ is the gyration radius (Mukai et al., 1992). We define the size parameter x as

$$x = \frac{2\pi a}{\lambda}, \tag{4.1}$$

where λ is the wavelength. We also define the relative refractive index $m_{\rm mat}$ as

$$m_{\rm mat} = n_{\rm mat} + ik_{\rm mat}, \tag{4.2}$$

where $n_{\rm mat}$ and $k_{\rm mat}$ are the real and imaginary parts of the refractive index of the assumed material, respectively.

4.2.1 Dust grains: monomers

We consider a dust aggregate, which consists of a number of monomers. The monomers are assumed to be composed of silicate, organics, and water ice without any void structure. The mass fractional abundance is set to be consistent with Pollack et al. (1994), where $\zeta_{\rm silicate} = 2.64 \times 10^{-3}$, $\zeta_{\rm organics} = 3.53 \times 10^{-3}$, and $\zeta_{\rm ice} = 5.55 \times 10^{-3}$. The grain densities of silicate, organics, and ice are taken to be 3.5 g cm^{-3}, 1.5 g cm^{-3}, and 0.92 g cm^{-3}, respectively. The mean internal density is therefore 1.68 g cm^{-3}. The resultant volume fractions are 8 % of silicate, 26 % of organics, and 66 % of water ice. We use the refractive index of astronomical silicate from Weingartner & Draine (2001), organics from Pollack et al. (1994), and water ice from Warren (1984).

Here, we discuss the structure of a monomer composed of various materials. We assume that the monomer has a core-mantle structure, where silicate components are inside and ice and organics cover the silicate core. This assumption is reasonable because the condensation temperature of silicates is much higher than those of ices and organics. [2] The collisional and static compression and fragmentation velocity are determined by the surface material of monomers, which is expected to be ice or organics. Therefore, the structure and fluffiness of

[2]The material properties of organics, such as surface energy and Young's modulus, are still uncertain, but it is considered to be similar to those of ice (e.g., Kudo et al., 2002).

the aggregates are expected to be similar to icy aggregates (Kataoka et al., 2013b; Okuzumi et al., 2012).

The effective refractive index of the mixture can be derived from dielectric functions. By using Maxwell-Garnett rule without voids, the effective dielectric function is obtained as

$$\epsilon_{\rm mix} = \frac{\Sigma f_j \gamma_j \epsilon_j}{\Sigma f_j \gamma_j}, \tag{4.3}$$

where

$$\gamma_j = \frac{3}{\epsilon_j + 2}, \tag{4.4}$$

and f_j and ϵ_j represent the volume filling factor and the dielectric function of each species. The dielectric function is related to the refractive index as $\epsilon = m^2$.

Figure 4.1 shows the real and imaginary part of the effective refractive index of the mixture. For simplicity, we use n and k for the real and imaginary parts of the effective refractive index, respectively. We use this effective refractive index as the material refractive index in the following discussion.

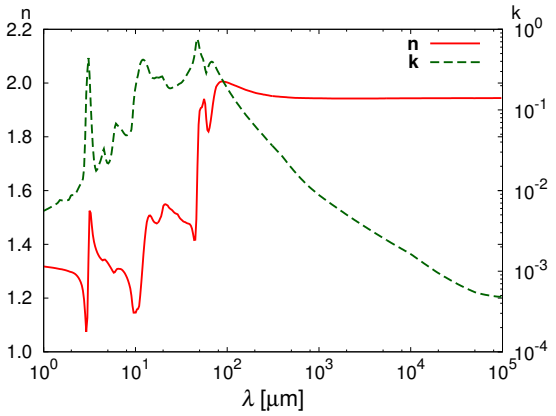

Fig. 4.1 The complex refractive index of the mixture of silicate, organics, and water ice.

The simplified fractional abundance based on Pollack et al. (1994) has been widely used in several papers (e.g., D'Alessio et al., 2001; Isella et al., 2009; Pérez et al., 2012; Ricci et al., 2010a,b; Tanaka et al., 2005). Some recent studies use the dielectric functions of carbonaceous material (Zubko et al., 1996) instead of organics (Li & Greenberg, 1997; Pollack et al., 1994). In protoplanetary disks, the carbonaceous materials would interact with other species to produce organics. Thus, we use the dielectric function of organics based on Pollack et al. (1994) in this paper. However, the optical properties of organics in pro-

toplanetary disks have large uncertainties because astronomical organics may be different from laboratory data.

4.2.2 Aggregates of monomers

To calculate the opacity of fluffy aggregates, we use the effective medium theory again. In the case of the mixture of monomers and voids, Maxwell-Garnett theory is applicable to obtain the effective dielectric function as

$$\epsilon_{\rm eff} = \frac{1+2fF}{1-fF}, \tag{4.5}$$

where

$$F = \frac{\epsilon_{\rm mix}-1}{\epsilon_{\rm mix}+2}, \tag{4.6}$$

$\epsilon_{\rm mix}$ is the effective dielectric function of the mixture, and f is the volume filling factor of the aggregate.

We will investigate the mass opacity of dust aggregates for a wide range of the dust radius a and the filling factor f. We adopt the Mie calculation with the effective medium theory described above. Voshchinnikov et al. (2005) show that the EMT is a good approximation when the inclusions are smaller than the wavelengths of radiation. Here, the monomer size is 0.1 μm while the wavelengths are larger than 1 μm. Thus, the EMT would be a good approximation in the calculations in this paper. The filling factor is expected to decrease to $f \sim 10^{-4}$ and the dust radius grows from micron to kilometer (Kataoka et al., 2013b). Therefore, we will investigate the mass opacity in such parameter space.

We note that we do not choose a set of a and f where both a and f are too small. In the porosity evolution scenario proposed by Kataoka et al. (2013b), the dust aggregates grow as fractals in the very early stage of the coagulation. This stage corresponds to the lower limit of a and f. In this paper, we consider a set of a and f where $af \geq 0.1\mu$m.

4.2.3 Mass opacity

We use the Mie calculation with the effective medium theory to calculate dimensionless absorption and scattering coefficients $Q_{\rm abs}$ and $Q_{\rm sca}$. Then, we obtain absorption and scattering mass opacities defined as

$$\kappa_{\rm abs} = \frac{\pi a^2}{m} Q_{\rm abs}, \tag{4.7}$$

$$\kappa_{\rm sca} = \frac{\pi a^2}{m} Q_{\rm sca}. \tag{4.8}$$

We note that the mass opacities are given per gram of dust. To obtain the mass opacities per gram of gas, one should divide the mass opacities by the dust-to-gas mass ratio.

4.3 Results

4.3.1 Absorption mass opacity

The absorption mass opacity of porous dust aggregates strongly depends on their size and filling factor. In protoplanetary disks, radio emission at millimeter wavelengths provide optically thin emission, in other words, directly reflects the opacity. Therefore, we aim to reveal what properties of dust aggregates determine the mass opacity.

Figure 4.2 shows the dependency of the mass opacities of dust aggregates on the dust radius a and the filling factor f. Figure 4.2 (b) shows the mass opacity of different dust radius while the filling factor is fixed at unity (i.e., compact growth). The absorption mass opacity from optical to infrared wavelengths decreases as the aggregate size increases, and it has an enhancement because of the interference at the millimeter wavelengths depending on the aggregate size. This trend is well-known as the grain-growth effects on the dust opacity. Figure 4.2 (c) shows the mass opacity of different filling factors while the dust radius is fixed at $a = 1$ mm. The mass opacity strongly depends on the filling factor but cannot be characterized by one parameter. Figure 4.2 (d) shows that the mass opacity when both a and f change but af remains constant. The mass opacity is almost the same in this case. This result suggests that the optical properties of fluffy dust aggregates are characterized by af.

Here, we introduce a new parameter af, where a is the dust radius and f is the filling factor. Keeping af constant corresponds to the constant mass-to-area ratio of the dust aggregates because (mass-to-area ratio) $\sim (a^3 f)/(a^2) \sim af$. We already find that the mass opacity is characterized by af in the case of $af = 0.1\,\mu$m in Fig. 4.2 (d). Next, we investigate whether the mass opacity is characterized by one parameter af in the wide range of af.

Figure 4.3 shows the mass opacity where af is fixed for each panel: af has values of 1 μm, 10 μm, 100 μm, 1 mm, and 1 cm. This figure clearly shows that the absorption mass opacity is almost the same in the cases of the same af. For example, dust aggregates that have a size of 10 m and a filling factor of 10^{-4} are optically equivalent to 1 mm compact grains except for the interference structure. We will show the reason why the absorption mass opacity is characterized by af in Section 4.4.

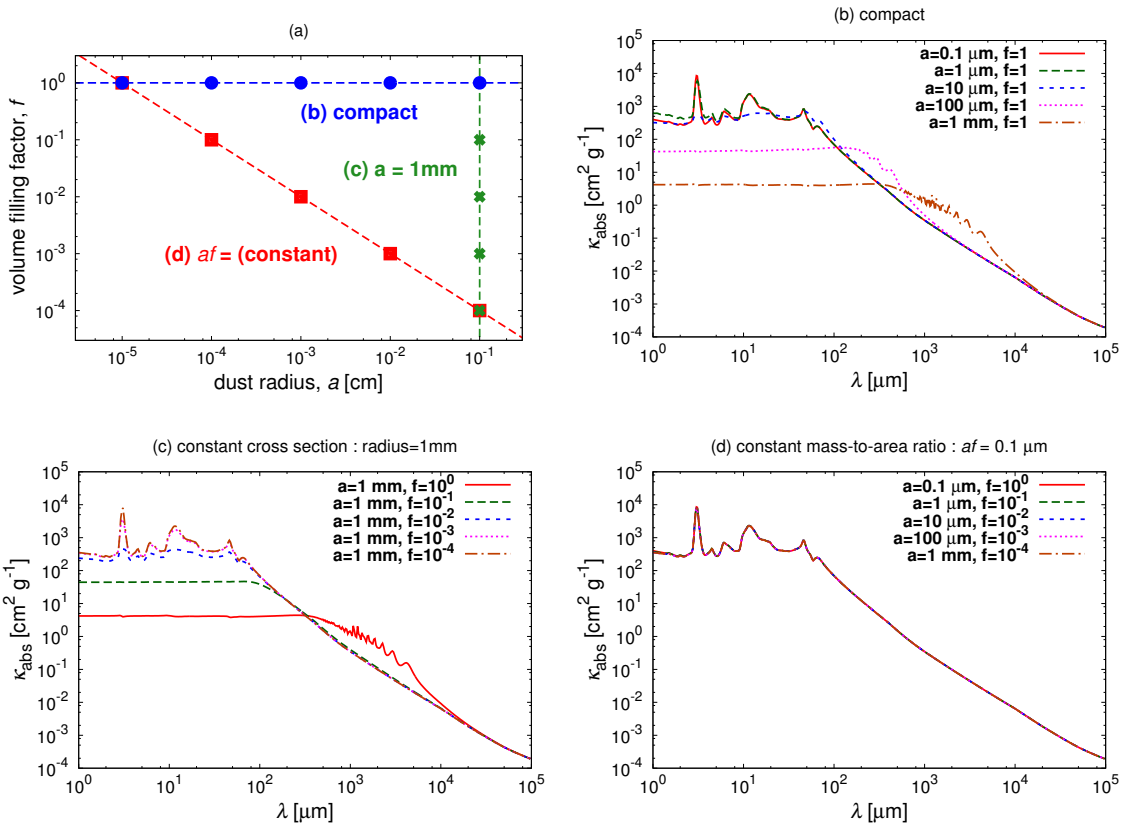

Fig. 4.2 Absorption mass opacities for each dust radius and filling factor. (a) The parameter space in the volume filling factor f against the dust radius a to investigate the mass opacity. The dotted lines correspond to (b) (c) and (d). (b) The absorption mass opacity when the dust radius a changes while $f = 1$. (c) When the dust filling factor changes while $a = 1$ mm. (d) When both a and f change while af keeps constant. The constant af corresponds to the same mass-to-area ratio of the dust aggregates.

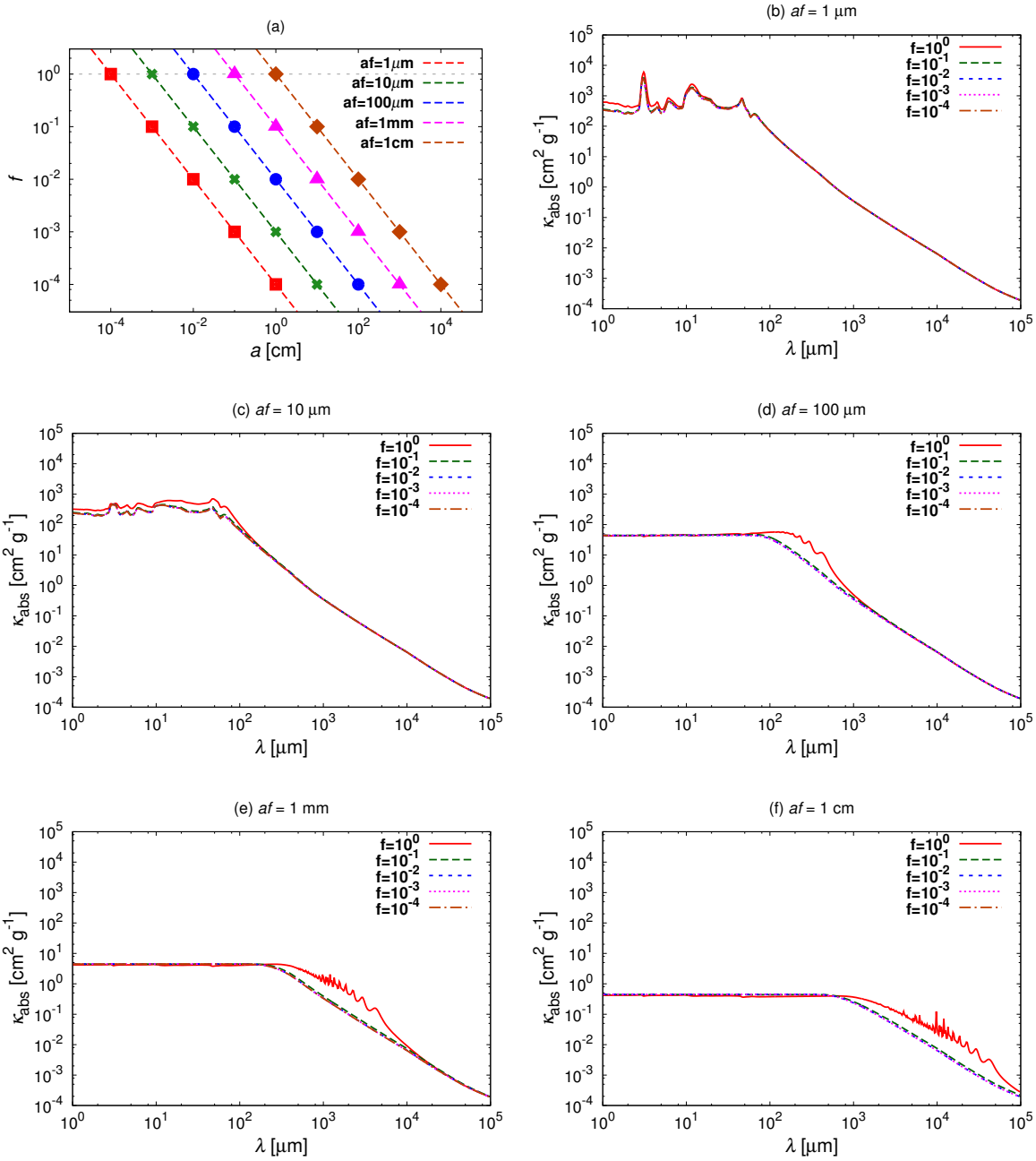

Fig. 4.3 The absorption mass opacity in cases of different af. Panel (a) shows the parameter space of f and a in the cases of (b) to (f). The mass opacities are shown in the cases of (b) $af = 1$ μm, (c) $af = 10$ μm, (d) $af = 100$ μm, (e) $af = 1$ mm, and (f) $af = 10$ mm.

That the absorption mass opacity is characterized by af is a very naive result for observations: the filling factor cannot be measured because it is degenerated with the dust radius. Therefore, to derive both the filling factor and the dust radius separately, we should find another clue rather than the general behavior of the absorption mass opacity. We find two differences which might be ways to distinguish between a and f: the interference structure of the absorption mass opacity and the scattering mass opacity at long wavelengths. We discuss the interference first and will discuss the scattering mass opacity later in this section.

The only difference in the absorption mass opacity between the compact and fluffy cases if af is the same is the interference structure, which appears when the size parameter x is close to unity. In the case of af =1 mm, for example, the absorption mass opacity in the compact case is one order of magnitude higher than the fluffy cases. This is a way to distinguish between compact grains and fluffy aggregates in protoplanetary disks. We will discuss the reason why the interference structure is unique only in the compact case in Section 4.4, and also discuss the feature as a way to distinguish between compact and fluffy aggregates by using the dust opacity index β in Section 4.5.

4.3.2 Scattering mass opacity

We also calculate the scattering mass opacity by using Mie calculations. Figure 4.4 shows the scattering mass opacities in the case of $af = 0.1\,\mu$m, $1\,\mu$m, $100\,\mu$m, and 1 mm. This figure suggests that the scattering mass opacity is not characterized by af at the longer wavelengths. At the shorter wavelengths, the mass opacity corresponds to the geometric cross section. In the compact case, the mass opacity scales as λ^{-4} at the longer wavelengths. On the other hand, in the fluffy case, the mass opacity scales as λ^{-2} at the intermediate wavelengths, then scales as λ^{-4} at the longer wavelengths. We will come back to this point with a physical explanation in Section 4.4.

As shown in Figure 4.4, the scattering mass opacity of the fluffy aggregates is expected to be higher than the compact case at the longer wavelengths even when the absorption mass opacity is almost the same. Thus, we investigate the ratio of $\kappa_{\rm sca}$ against $\kappa_{\rm abs}$. Figure 4.5 shows the ratio in each case corresponding to Fig. 4.4. In the case of compact and af = $0.1\,\mu$m, the scattering mass opacity is less than absorption. On the other hand, the scattering mass opacity dominates the absorption mass opacity even at the infrared in fluffy cases when $af = 0.1\,\mu$m. This greatly affects the infrared observations of dust grains. For example, Pagani et al. (2010) reported that dust grains in dense interstellar medium is composed of micron-sized grains (and not $0.1\,\mu$m) because of the high scattering efficiency observed

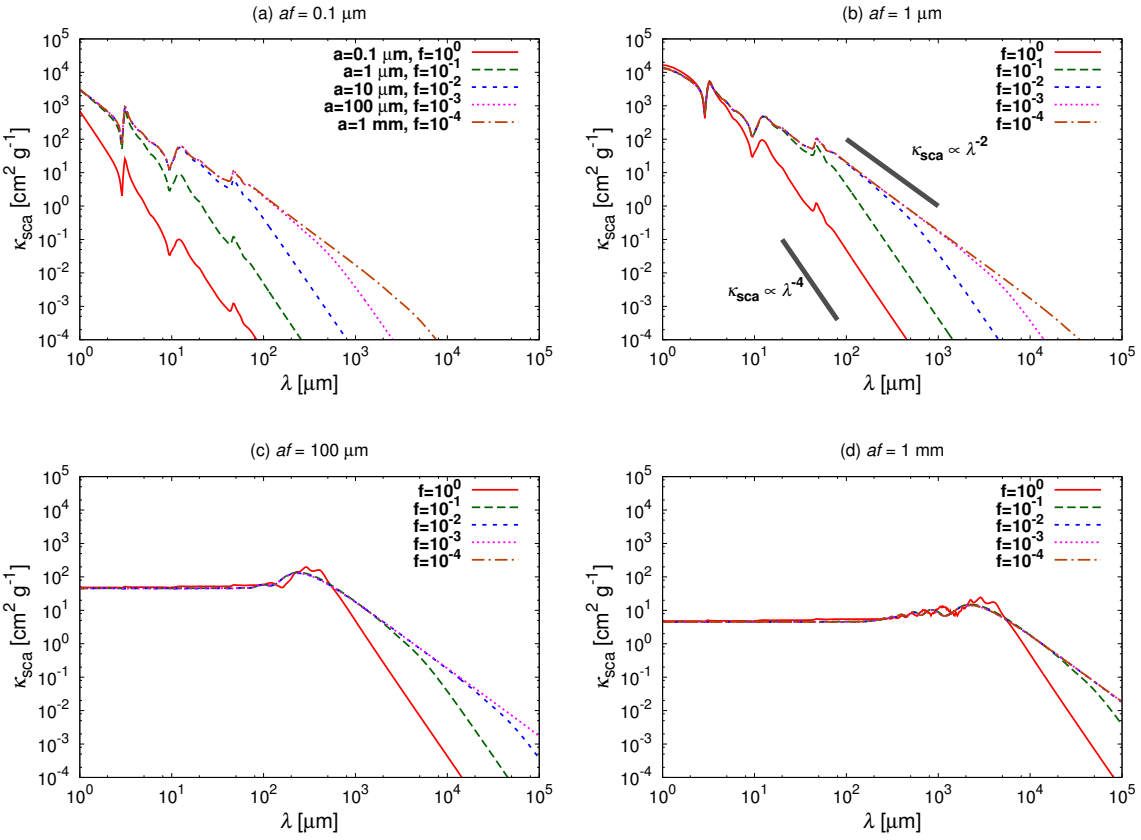

Fig. 4.4 Same as Figure 4.3 but for scattering mass opacities.

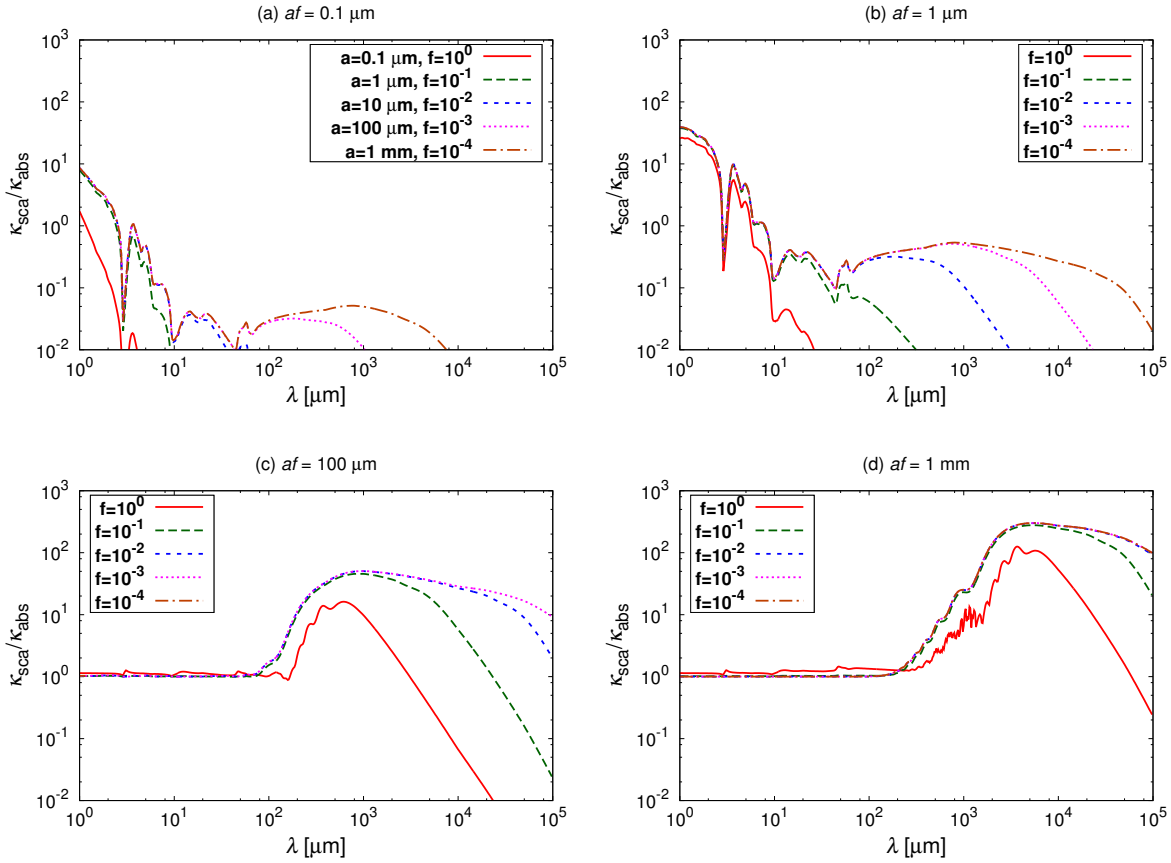

Fig. 4.5 The ratio of scattering mass opacity over absorption mass opacity $\kappa_{\rm sca}/\kappa_{\rm abs}$ in the cases of $af = 0.1$ μm, 1 μm, 100 μm, and 1 mm. Each panel shows the cases with the same af, but the filling factor ranges are in $f = 1, 10^{-1}, 10^{-2}, 10^{-3}$, and 10^{-4}.

by the Spitzer space telescope. Thus, they infer that the monomer size must be micron. However, figure 4.5 suggests that even if the monomers are 0.1 μm in size, the aggregates of 0.1 μm sized monomers represent the high albedo and thus might account for the observed high efficiency of scattering.

Figures 4.5 (c) and (d) show the scattering mass opacity in the case of $af = 100$ μm and 1 mm. The scattering mass opacity at the millimeter wavelengths is ten times larger than the absorption mass opacity in the compact case, and it is tens of times larger in the fluffy cases. This suggests that the millimeter continuum emission is dominated not by direct thermal emission, but by scattered emission in transition disks if the dust aggregates are grown to have a millimeter size. Moreover, determining the ratio of the scattering mass opacity over the absorption mass opacity at the millimeter wavelengths is a way to characterizing the porosity of the dust aggregates.

4.4 Analytic formulae of the opacities

In the previous section, we used the Mie calculations to obtain the mass opacity. In this section, we derive the analytic formulae of the mass opacity and compare them to the results of Mie calculations. By deriving analytic formulae, we explain why the mass opacity can be characterized by af. In addition, the analytic formulae would be a computationally less expensive method to calculate the opacity of large aggregates.

4.4.1 Approximation of refractive index

When we consider fluffy aggregates, the filling factor satisfies $f \ll 1$. If $f \ll 1$, from Eq. (4.5) and $\epsilon = m^2$, we obtain

$$n \simeq 1 + \frac{3}{2} f \mathrm{Re}(F), \tag{4.9}$$

$$k \simeq \frac{3}{2} f \mathrm{Im}(F), \tag{4.10}$$

to the first order of f. From these equations, we obtain that $n - 1 \propto f$ and $k \propto f$ in the case of fluffy aggregates where $f \ll 1$. We check the validity of the relations in Appendix 4.7.1.

We do not assume $f \ll 1$ when deriving the analytic formulae. After deriving the formulae, we assume $f \ll 1$ and use the relations of $n - 1 \propto f$ and $k \propto f$ to explain why the mass opacity is characterized by af.

4.4.2 Absorption mass opacity

We derive the approximated formulae of $Q_{\rm abs}$ in three limited cases, illustrated in Fig. 4.6: (1) $x \ll 1$, (2) $x \gg 1$ and optically thin ($kx \ll 3/8$) media, and (3) $x \gg 1$ and optically thick ($kx \gg 3/8$) media. We note that the absorption mass opacity is $Q_{\rm abs}$ divided by the mass-to-area ratio of the aggregates.

$x \ll 1$

When the dust radius a is much smaller than the wavelength λ, the opacity goes into Reyleigh regime. This corresponds to $x = 2\pi a/\lambda \ll 1$. In this case, $Q_{\rm abs}$ can be written as

$$Q_{\rm abs} \simeq 4x\,{\rm Im}\left(\frac{m^2-1}{m^2+2}\right) = \frac{24nkx}{(n^2-k^2+2)^2+(2nk)^2}. \tag{4.11}$$

(see Eq. (5.11) in BH83). The imaginary part k of the refractive index is much smaller than the real part n (see Fig. 4.1 and Fig. 4.15). So, we can approximate $Q_{\rm abs}$ as

$$Q_{\rm abs} \simeq Q_{\rm abs,1} \equiv \frac{24nkx}{(n^2+2)^2}. \tag{4.12}$$

This equation explains the fact that the absorption mass opacity is characterized by mass-to-area ratio or af. At the longer wavelengths, n is almost unity while $k \propto f$. Using $f \propto m/a^3$, we obtain that kx is proportional to m/a^2, which is mass-to-area ratio. Since $\kappa_{\rm abs}$ is $Q_{\rm abs}$ divided by mass-to-area ratio, $\kappa_{\rm abs}$ is independent of dust properties.

$x \gg 1$ **and optically thin**

When the dust radius a is much larger than the wavelength λ, the opacity goes into geometric optics regime. In this regime, the optical properties can be understood by tracing the ray inside the material. The fraction of energy that transmits the material is $1-\exp(-\alpha\xi)$ where $\alpha = 4\pi k/\lambda$, and ξ is the path of the ray inside the material. If $\alpha\xi < 1$, the incident light is weakly absorbed by the material because it is optically thin on the ray. We set the length $\xi = 2a$, the diameter of the sphere. Thus, the condition $\alpha\xi < 1$ corresponds to $kx < 1$.

In the limit of $a \gg \lambda$ (or equivalently $x \gg 1$) and optically thin, we obtain

$$Q_{\rm abs} \simeq Q_{\rm abs,2} \equiv \frac{8kx}{3n}\left(n^3-(n^2-1)^{3/2}\right), \tag{4.13}$$

(see Eq. (7.2) in BH83).

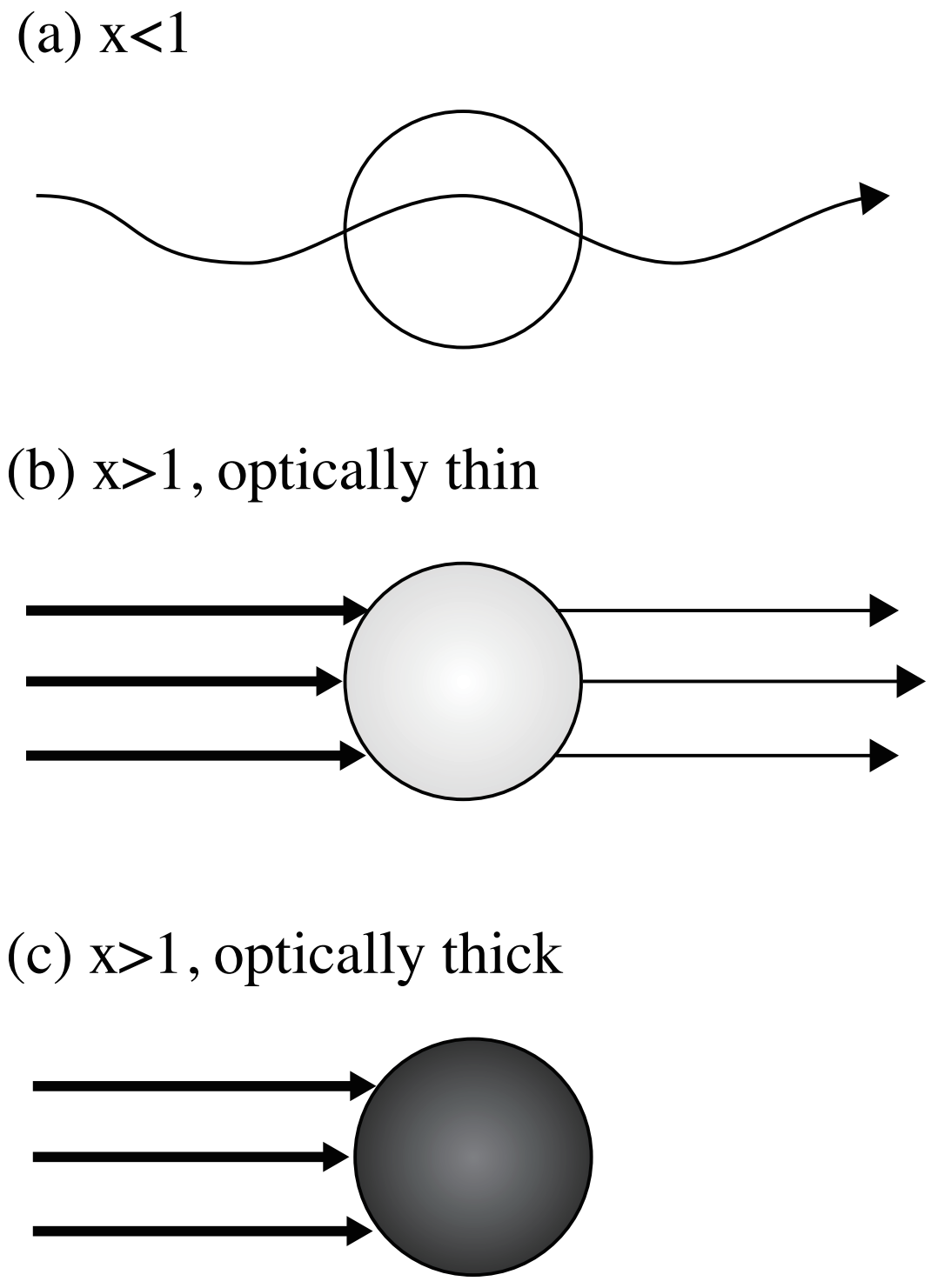

Fig. 4.6 The three limiting regime. (a) When $x \ll 1$, the opacity goes into the Rayleigh regimes. (b) When $x \gg 1$ and is optically thin ($kx \ll 3/8$), the opacity goes into the optically thin geometric regime. (c) When $x \gg 1$ and is optically thick ($kx \gg 3/8$), the opacity goes into the optically thick geometric regime.

We note that if $n = 1$, which is usually satisfied in the case of fluffy medium, $Q_{\rm abs}$ yields

$$Q_{\rm abs} = Q_{\rm abs,1} = Q_{\rm abs,2} = \frac{8kx}{3}. \tag{4.14}$$

This equation is also characterized by the mass-to-area ratio or af because $k \propto f$ and $x \propto a$. We also note that the analytic formula between optically thick and thin regimes should be changed when $Q_{\rm abs}$ is unity. Thus, we define optically thin as $kx \ll 3/8$.

$x \gg 1$ and optically thick

In the limit of $a \gg \lambda$ (equivalent to $x \gg 1$) and optically thick ($kx \gg 3/8$), on the other hand, the absorption coefficient is described as

$$Q_{\rm abs} \simeq Q_{\rm abs,3} \equiv \int_0^{\pi/2} (1 - R(\theta_i)) \sin 2\theta_i d\theta_i, \tag{4.15}$$

where the reflectance $R(\theta)$ is written as

$$R(\theta_i) = \frac{1}{2}\left(\left| \frac{\cos\theta_t - m\cos\theta_i}{\cos\theta_t + m\cos\theta_i} \right|^2 + \left| \frac{\cos\theta_i - m\cos\theta_t}{\cos\theta_i + m\cos\theta_t} \right|^2 \right), \tag{4.16}$$

and

$$\sin\theta_t = \frac{\sin\theta_i}{m} \tag{4.17}$$

(see Eq. (2.71), Eq. (7.5), and Eq. (7.7) in BH83). This regime is valid at shorter wavelengths (see Appendix 4.7.3 for the optical depth of the aggregate). As shown in Appendix 4.7.2, $Q_{\rm abs,3} \sim 1 - 0.1 \times f$, and thus $Q_{\rm abs,3} \sim 0.9$ for compact case and $Q_{\rm abs,3} \sim 0.99$ for $f = 0.1$. These values are regarded as unity in application to astronomical observations. Therefore, $Q_{\rm abs,3} \sim 1$ for most cases: the absorption cross section yields the geometric cross section. Because $Q_{\rm abs,3}$ has no dependency on f and a, $\kappa_{\rm abs}$ is characterized by af.

Analytic formula of absorption mass opacity

Combining the three limiting regimes, we obtain the analytic formula of the absorption mass opacity of dust aggregates as

$$Q_{\rm abs} = \begin{cases} Q_{\rm abs,1} & (x < 1) \\ \min(Q_{\rm abs,2}, Q_{\rm abs,3}) & (x > 1) \end{cases}. \tag{4.18}$$

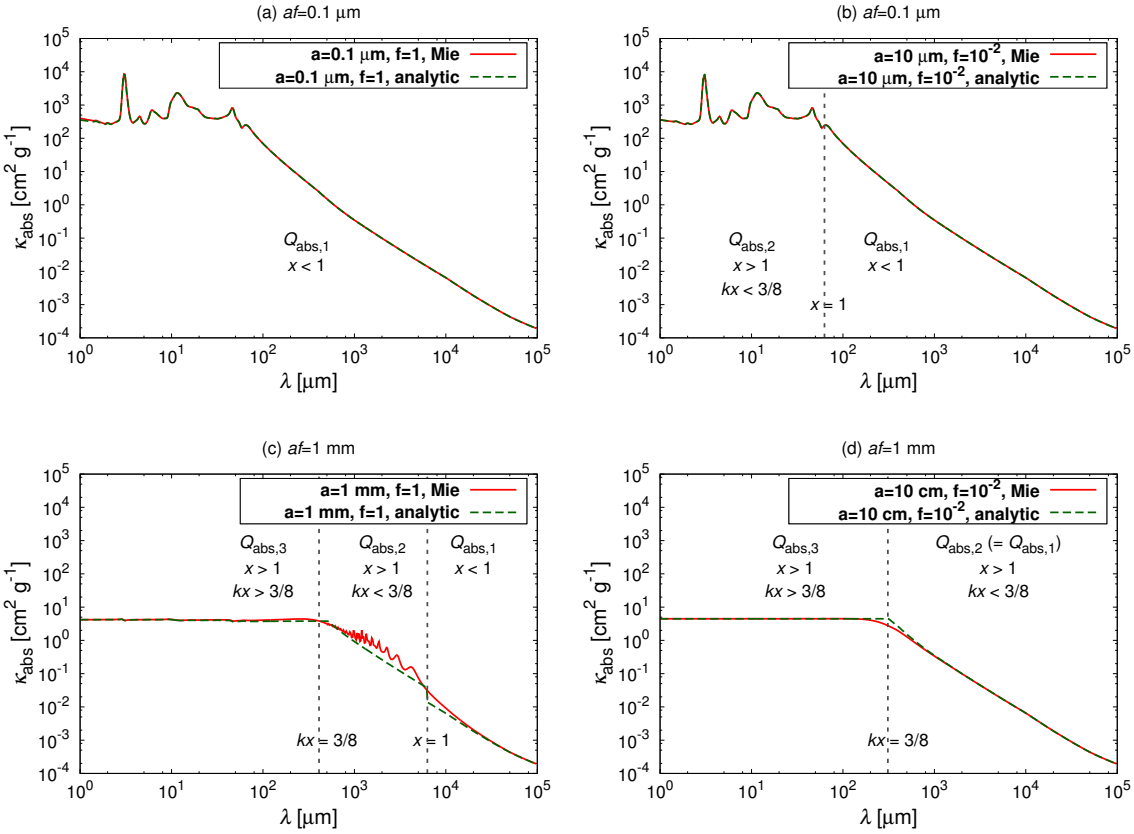

Fig. 4.7 The comparison of Mie calculations and the analytic formulae. The dotted lines show where $x = 1$ and $kx = 3/8$. (a) The mass opacity in the case of $af = 0.1$ μm and $f = 1$. (b) $af = 0.1$ μm and $f = 10^{-2}$. (c) $af = 1$ mm and $f = 1$. (d) $af = 1$ mm and $f = 10^{-2}$.

Figure 4.7 shows the absorption mass opacities calculated with both the Mie calculation and the analytic formula. The absorption mass opacity of Figs. 4.7 (a) and (b) are the same because $af = 0.1$ μm but only the filling factor is different ($f = 1$ and $f = 0.01$), as shown in the previous sections (see Fig. 4.3). Figure 4.7 (a) shows the case of $af = 0.1$ μm and $f = 1$ (compact). The whole wavelengths in this panel satisfy $x < 1$, and thus $Q_{\rm abs} \simeq Q_{\rm abs,1}$. The analytic formula greatly reproduce the Mie calculations. Figure 4.7 (b) shows the case of $af = 0.1$ μm and $f = 0.01$ (fluffy). In this case, $a = 10$ μm, and thus $x = 1$ at $\lambda = 2\pi a \simeq 63$ μm. We use $Q_{\rm abs} = Q_{\rm abs,1}$ for $x > 1$ and $Q_{\rm abs} = Q_{\rm abs,2}$ for $x < 1$ and connect them at $x = 1$. This also reproduces the Mie calculation.

Figures 4.7 (c) and (d) show the case of $af = 1$ mm, but the filling factor is 1 and 0.01, respectively. The absorption mass opacity of Figs. 4.7 (c) and (d) are almost the same except for the interference structure. The interference structure corresponds to where $x > 1$ and

$kx < 3/8$, the optically-thin geometric optics regime. We note that the difference between the Mie calculation and the analytic formulae is the interference structure. In Fig. 4.7 (c), which is the compact case, the real part of the refractive index is greater than unity. Thus, $Q_{\rm abs}$ has an enhancement because of the interference. In Fig. 4.7 (d), which is the fluffy case, on the other hand, the real part of the refractive index is almost unity and thus no enhancement appears and smoothly connects to $x < 1$ region at the longer wavelengths. From the analytic formula, we conclude that the interference structure only appears in the compact cases because n is still larger than unity when $x > 1$ and $kx < 3/8$.

4.4.3 Scattering mass opacity

In the same manner of obtaining the analytic formula of the absorption mass opacity, we also derive the analytic formula of the scattering mass opacity. In addition, by using the analysis, we explain why the mass opacity can and cannot be characterized by af.

$x \ll 1$

When $x \ll 1$, in the Rayleigh regime, $Q_{\rm sca}$ can be written as

$$Q_{\rm sca} \simeq \frac{8}{3} x^4 \left| \frac{m^2 - 1}{m^2 + 2} \right|^2, \tag{4.19}$$

(see Eq. (5.8) in BH83). At the longer wavelengths, $n - 1 \ll 1$ and $k \ll 1$. Therefore, the equation can be approximated to

$$Q_{\rm sca} \simeq Q_{\rm sca,1} \equiv \frac{32}{27} x^4 \left((n-1)^2 + k^2 \right). \tag{4.20}$$

As shown in Appendix 4.7.1, $(n-1) > k$ at the longer wavelengths. Therefore, $Q_{\rm sca,1} \propto x^4 (n-1)^2$. By using $x \propto a$ and $(n-1) \propto f$, we obtain $Q_{\rm sca,1} \propto a^4 f^2$. This is *not characterized* by af. When we consider two aggregates whose af is the same, the aggregate that has the larger radius has the larger scattering mass opacity at the longer wavelengths although $Q_{\rm abs}$ is same. In other words, the scattering efficiency at the longer wavelengths is a way to determine the filling factor of fluffy aggregates.

$x \gg 1$ **and optically thin**

If $x \ll 1$, the scattering mass opacity of an aggregate is regarded as the sum of the scattering mass opacity of each monomer because the scattered waves from all the constituent

monomers have approximately the same phase. If $x \gg 1$, by contrast, scattered waves with scattering angle $\theta > \theta_{\max} \sim 1/x$ cancel out because of the phase difference. Thus, the radiation within the solid angle of $\pi\theta_{\max}/4\pi$ is scattered. With the condition that $\theta_{\max} \sim 1/x$ and that $Q_{\rm sca,2}$ is smoothly connected to $Q_{\rm sca,1}$ at $x = 1$, we obtain

$$Q_{\rm sca} \simeq Q_{\rm sca,2} \equiv \frac{1}{x^2} Q_{\rm sca,1}. \tag{4.21}$$

Using the same discussion in the previous section, we obtain $Q_{\rm sca,2} \propto x^2(n-1)^2 \propto a^2 f^2$. This is again characterized by af. We note that the optical depth of the aggregate is unity when $Q_{\rm sca}$ is unity. Thus, the optical depth becomes unity where $x(n-1) \sim 1$ because $n - 1 > k$.

$x \gg 1$ and optically thick

When $x \gg 1$ and the medium is optically thick, $Q_{\rm sca} + Q_{\rm abs} = 2$. Therefore, in the same manner of the absorption mass opacity, we obtain

$$Q_{\rm sca} \simeq Q_{\rm sca,3} \equiv \int_0^{\pi/2} (1 + R(\theta_i)) \sin 2\theta_i d\theta_i, \tag{4.22}$$

(see Eq. (7.5) and Eq. (7.6) in BH83).

As discussed in Section 4.4.2, the integrated reflectance is $\sim 0.1 \times f$. Thus, $Q_{\rm sca,3} \sim 1 + 0.1 \times f$. This is regarded as $Q_{\rm sca,3} \sim 1$. Thus, the scattering mass opacity also goes to the geometric cross section at shorter wavelengths and is characterized by af.

Analytic formula of scattering mass opacity

The limiting regime in the case of $x \ll 1$ reproduce the results in the case $x \leq 1$. The same discussion is applicable to $x \gg 1$. Therefore, combining the three limiting regimes, we obtain the analytic formula of scattering mass opacity as

$$Q_{\rm sca} = \begin{cases} Q_{\rm sca,1} & (x < 1) \\ \min(Q_{\rm sca,2}, Q_{\rm sca,3}) & (x > 1) \end{cases}. \tag{4.23}$$

Figure 4.8 shows the comparison of scattering mass opacity obtained with the Mie calculation and the analytic formula. Figures 4.8 (a) and (b) show the case of $af = 0.1$ μm, but the filling factor is $f = 1$ and $f = 0.01$, respectively. The analytic formula in both cases reproduces the Mie calculation. Figures 4.8 (c) and (d) show the case of $af = 1$ mm, but the filling factor is $f = 1$ and $f = 0.01$, respectively. In this case, the analytic formula reproduces

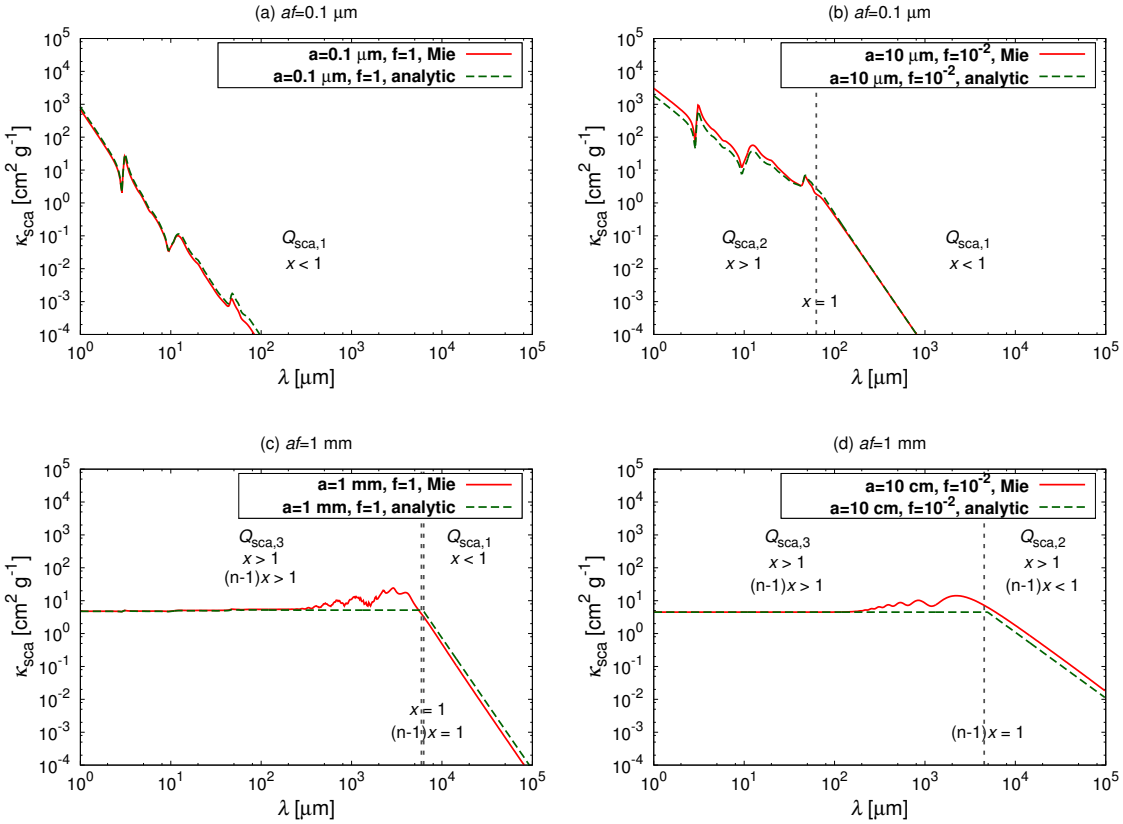

Fig. 4.8 Same as Fig. 4.7, but for scattering mass opacity.

the Mie calculation except for the interference structure because we assume that all the amplification by interference is damped when $x > 1$ and optically thin, which corresponds to $Q_{\rm sca} = Q_{\rm sca,2}$. However, the difference of the mass opacity between the analytic and Mie calculations is less than one order. Except for the interference structure, the analytic formula reproduces the Mie calculation even in the case of scattering mass opacity.

As already shown in Fig. 4.4, the scattering mass opacity is proportional to λ^{-2} at the intermediate wavelengths and λ^{-4} at the longer wavelengths in fluffy cases. This can be explained by $Q_{\rm sca,2}$. If $x = 2\pi a/\lambda$ is less than unity, which occurs at the longer wavelengths, $Q_{\rm sca} = Q_{\rm sca,1}$ and thus scales as λ^{-4} becasue $Q_{\rm sca,1} \propto x^4$. However, in the case of fluffy aggregates, we find the region where $x > 1$ and optically thin, and therefore $Q_{\rm sca} = Q_{\rm sca,2} = Q_{\rm sca,1}/x^2$. This is the reason why the scattering mass opacity at the intermediate wavelengths in fluffy cases scales as λ^{-2}.

4.5 Implications for opacity evolution in protoplanetary disks

The index of the dust opacity β has been widely used as an indicator of the dust growth. In this section, we will show how β changes as aggregates grow and drift both in compact and fluffy cases. Then, we propose a detection method of fluffy aggregates in protoplanetary disks by using the opacity index β.

4.5.1 Fluffy dust growth and opacity evolution

Before starting the discussion of β, we discuss the general mass opacity change as dust grains grow to fluffy aggregates in protoplanetary disks. We adopt a fluffy dust growth model proposed by Kataoka et al. (2013b). In this model, they reveal the overall porosity evolution from micron-sized grains to kilometer-sized planetesimals through direct sticking. In the coagulation, icy particles are sticky and thus they are not disrupted or bounced, but grow to a larger size (Wada et al., 2013, 2009, 2011). Moreover, the large radius of fluffy aggregates enables them to grow rapidly to avoid the radial drift barrier (Kataoka et al., 2013b; Okuzumi et al., 2012). Thus, the model is a complete scenario of growing path from dust grains to planetesimals by direct sticking.

Figure 4.9 shows the internal density evolution at 30 AU in orbital radius in a minimum mass solar nebula model, proposed by Kataoka et al. (2013b). We note that the figure shows the local porosity evolution, but dust aggregates start to drift inward once they grow to be

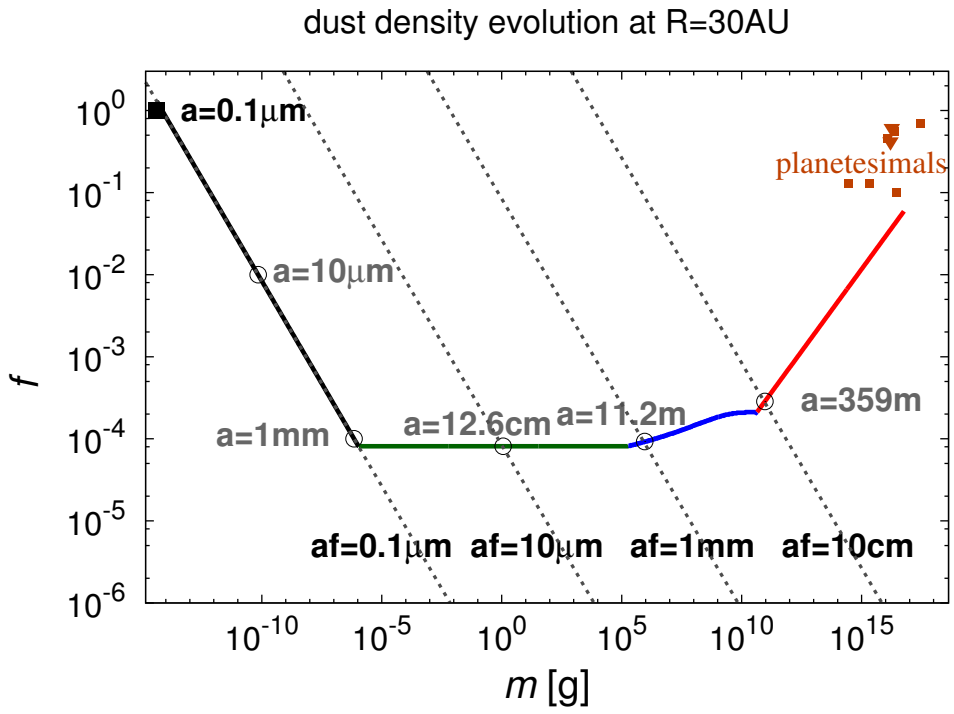

Fig. 4.9 The internal density evolution at $r = 30$ AU in the minimum mass solar nebula model (see Kataoka et al. 2013b for more details). The solid line represents the evolution. The black, green, blue, and red lines are in the coagulation phase of hit-and-stick, collisional compression, gas compression, and self-gravitational compression, respectively. The dotted lines show the af =(constant) lines, where $af = 0.1\ \mu$m, 10 μm, 1 mm, and 10 cm, respectively.

decoupled from the gas. We discuss the radial drift later in this section. The turbulent parameter $\alpha_{\rm D}$ is set to be 10^{-3} and the mean internal density is set to be 1.68 g cm^{-3}. The picture of the overall porosity evolution is as follows. As the dust grains first coagulate to form fluffy aggregates, the filling factor decreases to $f \sim 10^{-4}$. Once the collisional compression becomes effective, the density keeps constant. Then, the gas compression and the self-gravity compression make the dust aggregates compact.

The open circles represent the characteristic dust radius a, while the dotted lines show the lines of constant af. From this figure, the dust aggregates in the initial growth stage is optically the same. The initial growth is expected to be fractal. The dust aggregates coagulate with aggregates of similar sizes, and thus the fractal dimension is expected to be 2 (Okuzumi et al., 2012). Thus, the mass-to-area ratio of the aggregates keeps constant. In other words, af keeps the same value. Therefore, the initial growth is indistinguishable with no growth in the absorption mass opacity. After the initial growth, when the compression mechanisms become effective, the opacity is expected to change because the mass-to-area ratio changes.

Figure 4.10 shows the mass opacity change, corresponding to open circles in Fig. 4.9. The first three cases are degenerated in mass opacity because af is the same. Once the compression becomes effective, the mass opacity changes as expected in the dust growth. For example, when dust aggregates grow to have their radius of $a = 12.6$ cm, they have almost the same opacity as 10 μm compact grains. We note that the interference structure does not appear as aggregates grow because the filling factor is typically $f \sim 10^{-4}$ in this growth scenario.

4.5.2 Dust opacity index beta

We define β as an opacity slope between 1 mm and 3 mm. Here, we use af again because optical properties are characterized by af. We note that $af = a$ in the case of compact grains ($f = 1$). We consider several cases for calculating dust β where the filling factor f is fixed in each case. Calculating β, we consider a grain size distribution with a power law as $n \propto (af)^{-2}$ between a minimum and a maximum size, $(af)_{\rm min}$ and $(af)_{\rm max}$, respectively; $(af)_{\rm min}$ is chosen to be 0.1 μm. Figure 4.11 shows how the absorption mass opacity $\kappa_{\rm abs}$ at 1 mm and β changes as the aggregate size increases. The compact case in this figure corresponds to Fig. 3 in Ricci et al. (2010b). The red line shows the compact case, while green and blue lines are fluffy cases. The lines in the cases of $f < 10^{-2}$ are indistinguishable from the line of $f = 10^{-2}$, and thus we do not plot them. The absorption mass opacity has

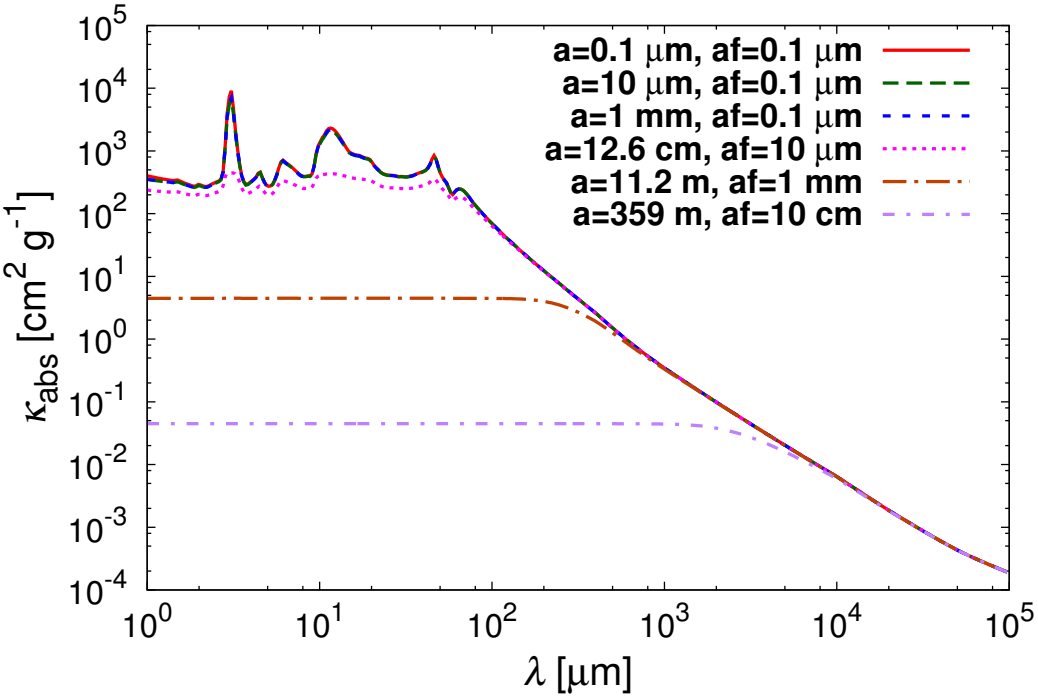

Fig. 4.10 The mass opacity change in the case of fluffy dust growth. Each line shows the mass opacity in the cases of different radius and filling factor, which corresponds to open circles in Fig. 4.9. The dust properties of the lines are as follows: red: $a = 0.1$ μm, and $af = 0.1$ μm; green: $a = 10$ μm, and $af = 0.1$ μm; blue: $a = 1$ mm, and $af = 0.1$ μm; magenta: $a = 12.6$ cm, and $af = 10$ μm; brown: $a = 11.2$ m, and $af = 1$ mm; purple: $a = 359$ m, and $af = 10$ cm.

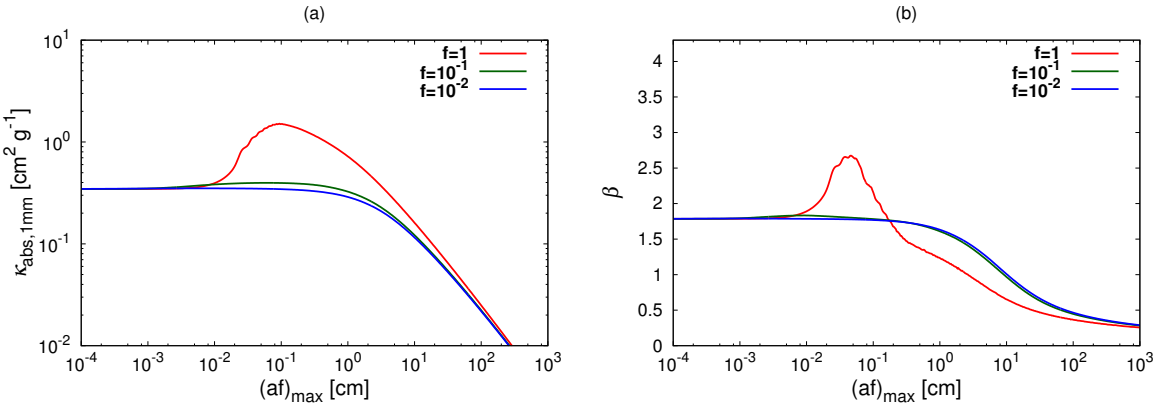

Fig. 4.11 (a) The absorption mass opacity at $\lambda = 1$mm against $(af)_{\max}$. The red, green, and blue lines show the cases of $f = 1, 10^{-1}$, and 10^{-2}. The lines in the cases of $f < 10^{-2}$ are indistinguishable from the line of $f = 10^{-2}$. The aggregate size distribution is assumed to be $n \propto (af)^{-2}$ where f is fixed in each case. (b) The β, the opacity slope between 1 mm and 3 mm, against $(af)_{\max}$.

a strong bump around $a_{0,\max} \sim 1$mm. This bump corresponds to the interference structure where the size parameter $x \sim 1$. On the other hand, the fluffy cases does not show such a bump because there is no interference. The bump of the mass opacity results in a bump of β in the compact case. The dust β increases up to ~ 2.7 in the compact case, but there is no bump in fluffy cases. In other words, β is always equal to or less than $\beta_{\rm ISM} = 1.7$ in fluffy cases.

From this result, the difference in the absorption mass opacity between compact and fluffy dust appears in the intermediate size, which is between 0.1 mm and 1 mm.

4.5.3 Radial profile of β

The radial size distribution of dust aggregates is determined by both dust growth and drift. In protoplanetary disks, the dust growth timescale strongly depends on orbital radius. In the inner part of disks, dust grains coagulate faster than in the outer part because of the shorter Keplerian period. Thus, dust aggregates have a larger size at the inner part and smaller at the outer part when considering only dust growth. When dust aggregates grow to larger sizes, they start to drift inward. Thus, the size where the aggregates start to drift is the maximum size of the aggregates at each orbital radius. The maximum size also depends on an orbital radius: the maximum size is larger in the inner part and smaller in the outer part. Combining

both effects of dust growth and drift, the radial profile of the size of dust aggregates is expected to be smaller in the outer part and larger in the inner part. Observationally, the radial profile of β have the information of the radial size distribution.

To obtain the radial profile of β, we adopt the following simple dust growth and drift model. We assume that there are initially 0.1 μm sized dust grains in the entire disk. We trace the growth and drift motion of each set of dust grains initially located at each orbital radius.

To calculate the time evolution of dust mass $M = M(t)$ and the orbital radius $r = r(t)$ at each orbital radius, we assume that dust grains have a monodisperse distribution at each orbital radius. Under this assumption, the dust growth and drift is described by (e.g., Okuzumi et al., 2012)

$$\frac{dM(t)}{dt} = \rho_{\rm d}\pi a^2 \Delta v \tag{4.24}$$

and

$$\frac{dr(t)}{dt} = -v_{\rm r}(M(t)), \tag{4.25}$$

where $\rho_{\rm d}$ is the spatial dust density, a the dust radius, Δv the relative velocity of dust grains or aggregates, and $v_{\rm r}(M(t))$ the drift velocity. We use the disk model of Kataoka et al. (2013b) (see also Okuzumi et al. 2012 for the definitions of the dust velocity and the disk model). Here, we briefly summarize the model. At a radial distance $r(t)$ from the central star, the gas-surface density profile is $1700(r/1{\rm AU})^{-p}$ g cm^{-2} where we use $p = 1$ in this paper. We note that the gas-surface density does not change with time to clarify the effects of dust growth and drift (e.g., Okuzumi et al., 2012). The initial dust-to-gas mass ratio is 0.01. The adopted temperature profile is $137(r/1{\rm AU})^{-3/7}$ K, which corresponds to midplane temperature (Chiang et al., 2001). This is cooler than optically thin disk models to focus on the dust coagulation in the midplane. The value of Δv is assumed be the root mean square of Brownian motion and turbulent motion (see Eq. (32) in Okuzumi et al. 2012). The diffusion coefficient $\alpha_{\rm D}$ is taken to be 10^{-3}. For the velocity induced by turbulence, we denote the velocity difference of dust and gas as dust-dust velocity for simplicity. We determine the dust scaleheight from the balance between sedimentation and turbulent diffusion (Brauer et al., 2008). The filling factor is fixed to be unity in the compact case and changes as a function of the orbital radius in the fluffy case following Kataoka et al. (2013b).

Figure 4.12 shows the dust growth and drift paths. The dashed lines show the paths of growing dust aggregates and the colored dotted and solid lines represent isochrones at $t = 10^5$ and $t = 10^6$ years. The isochrones represent the radial grain/aggregate-size distribution at the specific time. The size of dust aggregates increases with a decreasing orbital

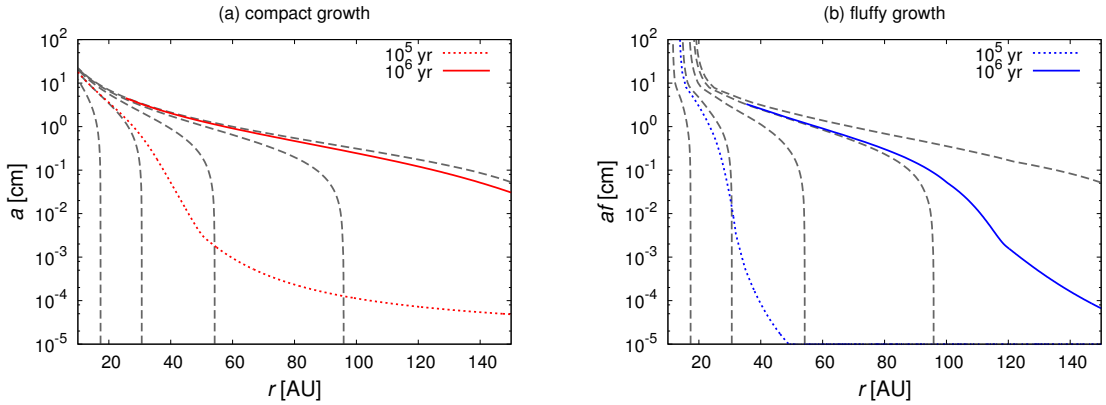

Fig. 4.12 The gray dashed lines represent the paths of the growth and drift of dust aggregates at each initial orbital radius. The solid and dotted lines represent the radial size distribution of dust aggregates at the specific time. (a) The compact case, where the red dotted line shows the isochrone at $t = 10^5$ years and the red solid line shows at $t = 10^6$ years. (b) The fluffy growth case, where the blue dotted line shows the isochrone at $t = 10^5$ years and the blue solid line at $t = 10^6$ years.

radius. This is caused by two effects: dust growth and drift. For example, on the line of the isochrone at 10^5 years in the compact case, shown in Fig. 4.12 (a), the dust growth determines the aggregate size beyond ~ 30 AU. At 30 AU or larger in orbital radius, dust growth is faster at the inner part of the disk than the outer part because the growth timescale is proportional to the Keplerian period (e.g., Okuzumi et al., 2012). At the orbital radius less than 30 AU, the maximum size is determined by the drift motion. The aggregates grow so large that they are decoupled from the gas, and drift inward. Therefore, the aggregate size at orbital radius less than 30 AU corresponds to the maximum size determined by the radial drift.

Figure 4.13 shows the radial β distribution for both compact and fluffy cases at the isochrones shown in Fig. 4.12. In the compact case, β increases to around $\beta \sim 2.7$ at 40 AU in the range of 10 AU at $t = 10^5$ years and at 150 AU in the range of 20 AU at $t = 10^6$ years. This means that protoplanetary disks have a specific radius where β is greater than $\beta_{\rm ISM} = 1.7$ in the compact case. In the fluffy case, on the other hand, β is always equal to or less than $\beta_{\rm ISM} = 1.7$. Therefore, if the radial β distribution always has a value of $\beta_{\rm ISM} = 1.7$ or less, it means that the millimeter emission comes from fluffy aggregates.

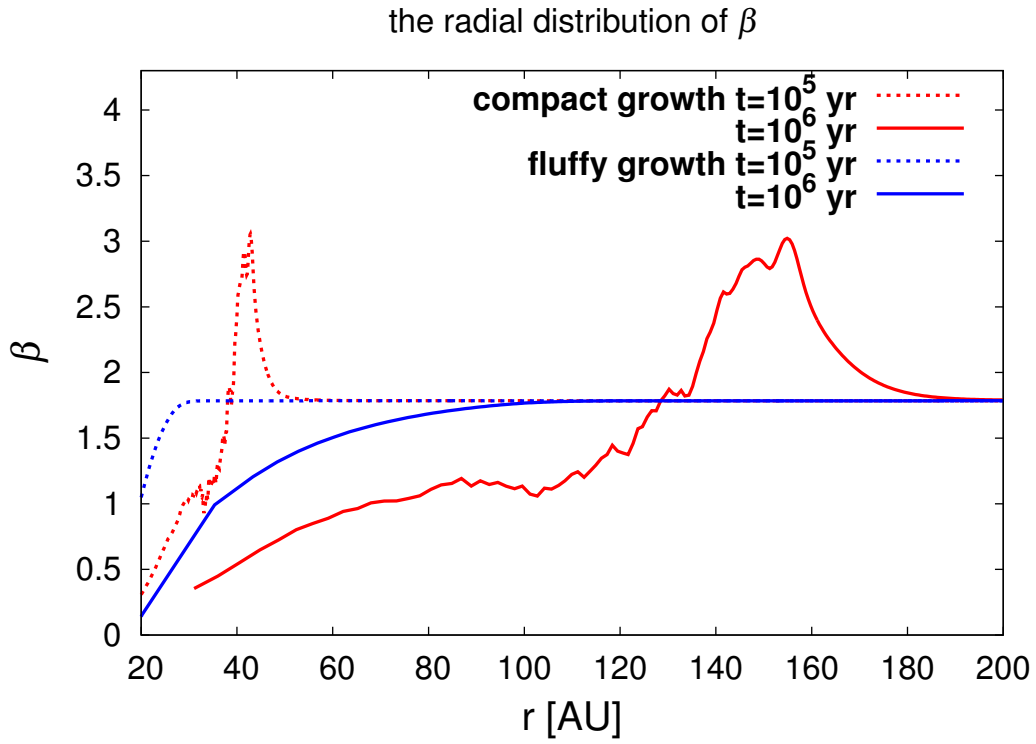

Fig. 4.13 The radial β distribution for compact and fluffy cases. Each line corresponds to the same line in Fig. 4.12.

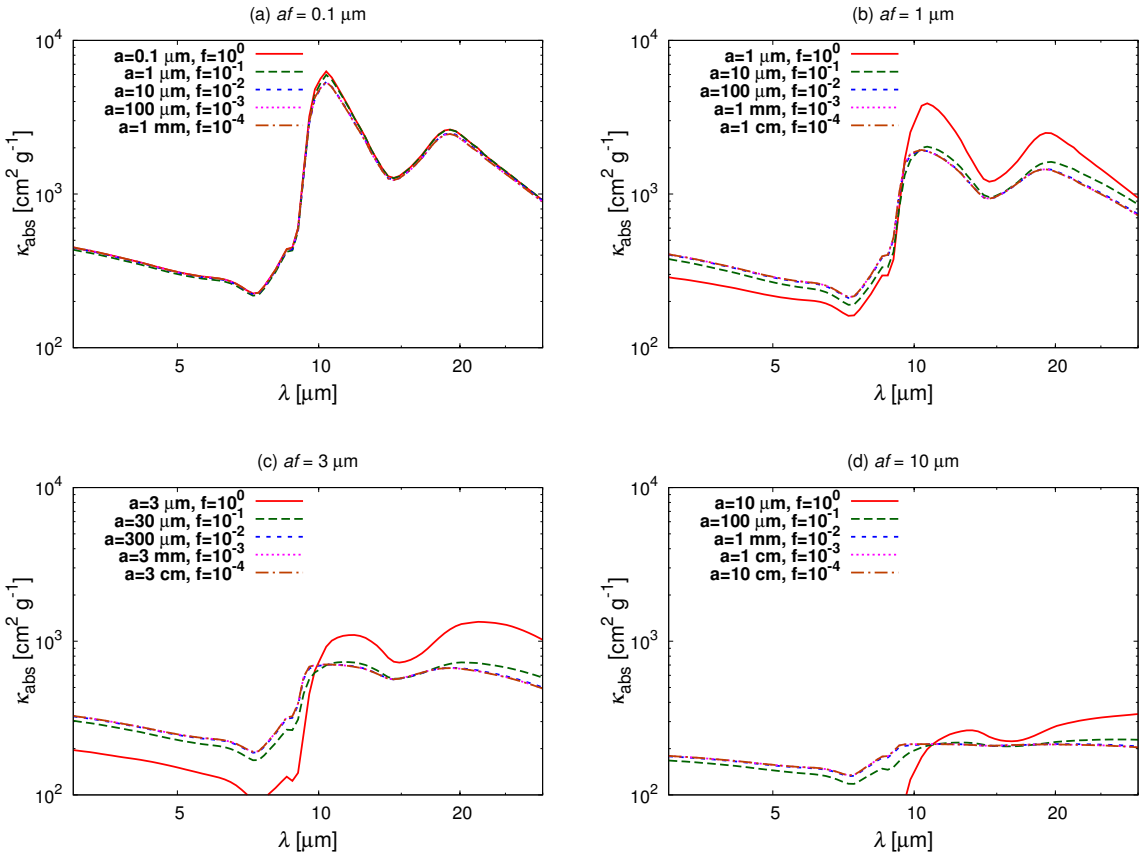

Fig. 4.14 The absorption mass opacity for silicate aggregates in cases of different af. The mass opacities are shown in the case of (a) $af = 0.1\ \mu$m, (b) $af = 1\ \mu$m, (c) $af = 3\ \mu$m, and (d) $af = 30\ \mu$m.

4.5.4 Silicate feature

In the inner part of the disk, ice particles are expected to be sublimated and there are dust aggregates whose constituent particles are made of silicate. Micron-sized silicate grains show the broad feature at 10 μm. The feature is used as a signature of grain growth (e.g., van Boekel et al., 2005). To show how the porosity affects the silicate feature, we also calculate the silicate feature of fluffy aggregates. In this section, we change the material constant: we assume pure silicate monomers. The material density is taken to be $\rho_{\rm mat} = 3.5$ g cm^{-3} and the refractive index is taken from Weingartner & Draine (2001).

Figure 4.14 shows the absorption mass opacity in cases of silicate aggregates. Each panel shows the mass absorption opacities where af is constant. When $af = 0.1\ \mu$m, the broad silicate feature is seen at around $\lambda = 10\ \mu$m and does not significantly change as the

aggregate size increases from 0.1 μm to 1 mm. In the cases of af = 1-10 μm, the silicate feature becomes weaker as af increases. The absorption mass opacity of porous aggregates ($f \leq 0.1$) is independent of the aggregate size as long as af is constant, as is also shown in the case of icy aggregates. The small differences between the cases of $f = 1$ and $f \leq 0.1$ derive from the interference as well as the icy aggregates. Thus, except for the interference, the silicate feature disappears as af increases.

4.6 Summary and discussion

We calculated the mass opacity of fluffy dust aggregates expected to be in protoplanetary disks. The wavelengths are in the range of 1 μm $< \lambda <$ 1 cm and the filling factor in the range of $10^{-4} < f < 1$. The assumed composition is the mixture of silicate, organics, and water ice (Pollack et al., 1994). We used the Mie calculation with the effective medium theory to calculate the mass opacity of fluffy aggregates. Our main findings are as follows.

- The absorption mass opacity of dust aggregates is characterized by af, where a is the dust radius and f is the filling factor. The absorption mass opacity is almost independent of the aggregate size when af is constant. This makes it difficult to distinguish between fluffy aggregates and compact grains in observations. The only difference of the absorption mass opacity between compact grains and fluffy aggregates where af is the same appears as the interference structure in the compact case at the size parameter $x \sim 1$.

- The scattering mass opacity at short wavelengths is also characterized by af, but not at long wavelengths. The scattering mass opacity at the long wavelengths is higher in more fluffy aggregates even if af is the same. The scattering mass opacity scales as λ^{-2} at intermediate wavelengths and scales as λ^{-4} at the longer wavelengths.

- We also derived the analytic formulae of the absorption and scattering mass opacities, connecting the three limiting cases, which are the Rayleigh regime, the optically-thin geometric regime, and the optically-thick geometric regime. The analytic formulae reproduce the results of the Mie calculations. The formulae are expected to greatly reduce the computational time to calculate the opacity of large fluffy aggregates. By using the analytic formulae, we analytically showed that the absorption mass opacity is characterized by one parameter af except for the interference structure. We also showed that the scattering mass opacity at the shorter wavelengths is also characterized by af, but not at the longer wavelengths. Thus, the fact that the mass opacity is

characterized by af is valid even out of the range investigated in the Mie calculation in this paper and is also applicable to other materials.

- The opacity index β is a good way to distinguish between fluffy aggregates and compact grains at observations of protoplanetary disks. If we assume the compact grain growth, with increasing grain size, the opacity index β increases to ~ 2.7 and then decreases. If we assume fluffy aggregate growth, the index β monotonously decreases from its initial value $\beta_{\rm ISM} = 1.7$ (see Fig. 4.11). If dust grains are compact in protoplanetary disks, the radial distribution of the index β should have a peak of ~ 2.7 (see Fig. 4.13).

- We also calculated the absorption mass opacity of silicate aggregates at around $\lambda = 10\,\mu$m. The opacity of fluffy aggregates has the $10\,\mu$m feature as well as compact silicate grains. The silicate feature is also appropriately characterized by af.

In this paper, as a first step, we use the effective medium theory. Voshchinnikov et al. (2005) have shown that EMT is a good approximation when considering small inclusions. We considered $0.1\,\mu$m sized monomers and the wavelength ranges from $1\,\mu$m to 10 cm. Because the monomer size is less than the wavelengths, EMT would be a good approximation. However, the validity of EMT at infrared, especially at short wavelengths, is somewhat marginal because the wavelengths are close to the monomer size. Thus, the validity of the effective medium theory should be further tested by future work.

We proposed that the radial profile of β is a way to distinguish between compact grains and fluffy aggregates. Pérez et al. (2012) have put a constraint on the radial β distribution by observing a protoplanetary disk AS 209 with VLA, SMA, and CARMA. They found that β has a lower value inside the disk rather than the constant β in the whole disk. It is consistent with the model of Fig. 4.12, where the grain size is distributed because of the difference of growth time and the maximum grain size is limited by radial drift. The results of Pérez et al. (2012) also prefer the fluffy growth scenario to the compact because there is no signature that β is large as $\beta \sim 3$. However, the observation has little information about β in the outer part of the disk because of the sensitivity limitation at the longer wavelengths. Thus, to clearly determine whether the emission comes from compact grains or fluffy aggregates, we need higher sensitivity at the longer wavelengths. Moreover, to reject the possibility of $\beta > \beta_{\rm ISM}$, we need a high spatial resolution to resolve 20 AU bump in the compact case at $t = 10^6$ years. This observation is challenging, but would be a good target of ALMA.

The fact that the scattering mass opacity at the longer wavelengths cannot characterized by af is another way to distinguish between compact grains and fluffy aggregates. Here,

we propose the polarization observation of the millimeter continuum emission. The scattered light is expected to be linearly polarized, and thus by comparing the intensity and the polarized intensity, the ratio of the scattering and absorption mass opacity can be directly observed. Although the polarized emission depends on the disk geometry and has many uncertainties, it would be a good target in the next phase of ALMA.

In addition, Mulders et al. (2013) proposed that to interpret the low effective albedo of protoplanetary disks, there are large particles at the outer disk surface and they should be porous structures to be stirred up to the surface. However, we showed that the infrared scattering opacity is determined by af In addition, the coupling efficiency of aggregates to the disk gas is also determined by af. Thus, the optical and kinematical properties are degenerated. Therefore, the porous aggregates would not help to interpret the observations of the low effective albedo.

4.7 Appendix: refractive index of fluffy aggregates

In this section, we confirm the validity of the assumptions used to derive the analytic formula in Section 4.4.

4.7.1 $(n-1) > k$ at the longer wavelengths

Figure 4.15 shows the comparison of $n-1$ and k when $f = 1, 10^{-1}, 10^{-2}, 10^{-3}$, and 10^{-4}. We confirm that the refractive index always satisfies $n-1 > k$ at the longer wavelengths in any value of f. Moreover, we also confirm that $(n-1) \propto f$ and $k \propto f$ when $f < 1$.

4.7.2 Reflectance

We define the integrated reflectance as

$$R \equiv \int_0^{\pi/2} R(\theta_i) \sin 2\theta_i d\theta_i. \tag{4.26}$$

When the medium satisfies $x \gg 1$ and is optically thick, $Q_{\rm abs}$ and $Q_{\rm sca}$ are written as $Q_{\rm abs} = Q_{\rm abs,3} = 1 - R$ and $Q_{\rm sca} = Q_{\rm sca,3} = 1 + R$. We assume that $R \ll 1$, and therefore $Q_{\rm abs}$ and $Q_{\rm sca}$ are unity in Section 4.4. Figure 4.16 shows the integrated reflectance R. Roughly speaking, $R \sim 0.1 \times f$ and thus we can assume that $Q_{\rm abs}$ and $Q_{\rm sca}$ are unity in the regime.

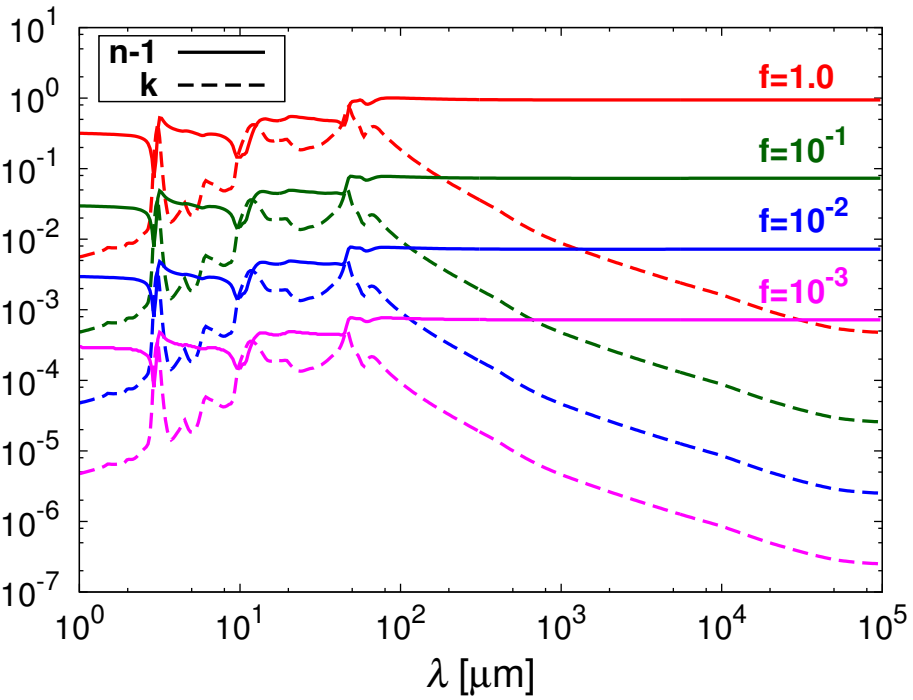

Fig. 4.15 $n-1$ and k against the wavelengths when $f = 1, 10^{-1}, 10^{-2}$, and 10^{-3}.

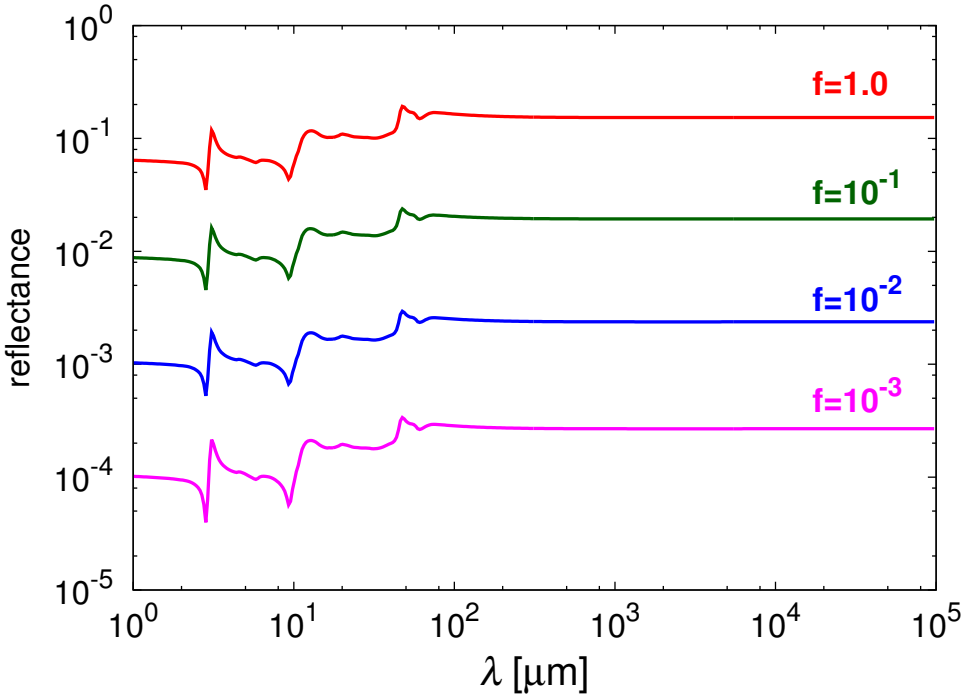

Fig. 4.16 The integrated reflectance when $f = 1, 10^{-1}, 10^{-2}$, and 10^{-3}.

4.7.3 Optical thickness inside the material

We discuss the optical thickness inside the medium by considering whether kx is greater than 3/8. Figure 4.17 shows kx in the case of $af = 0.1\,\mu$m, $10\,\mu$m, and 1 mm. We confirm

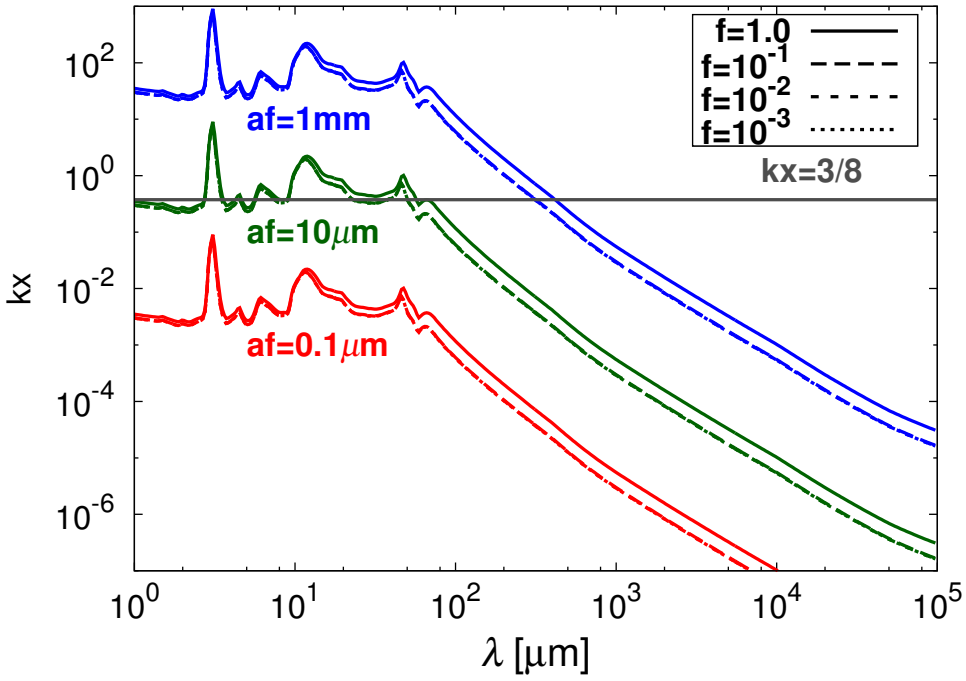

Fig. 4.17 kx against wavelengths when $af = 0.1\,\mu$m, $10\,\mu$m, and 1 mm. The solid lines represent the compact cases while the dashed lines fluffy cases.

that if af is the same, kx is almost the same at all wavelengths. In the case of $af = 0.1\,\mu$m, the medium is totally optically thin. In the case of $af = 10\,\mu$m, the medium is optically thin at the longer wavelengths and marginally optically thick when $\lambda \lesssim 10^{-2}$ cm. In the case of $af = 1$ mm, the medium is optically thin at the longer wavelengths and optically thick when $\lambda \lesssim 6 \times 10^{-2}$ cm.

Chapter 5

Conclusions

5.1 Summary and conclusions

This thesis aimed to reveal a pathway of the dust coagulation in protoplanetary disks which is free from the three main barriers in dust coagulation, which are the radial drift, fragmentation, and bouncing barriers. It has been shown that dust grains coagulate to form extremely porous structure in protoplanetary disks, which are not compressed by collisions of themselves.

In Chapter 2, we derived the compressive strength of porous dust aggregates. For numerical simulations, we adopted the particle-particle interaction model formulated by Dominik & Tielens (1997) and developed by Wada et al. (2007). As a result, we find that the compressive strengths of porous aggregates is given by

$$P = \frac{E_{\rm roll}}{r_0^3}\phi^3, \tag{5.1}$$

where ϕ is the filling factor, $E_{\rm roll}$ the rolling energy of monomer particles, and r_0 the monomer radius. We confirm that this formula is valid when the filling factor ϕ is lower than ~ 0.1. In addition, this formula is also analytically derived and confirmed.

In Chapter 3, we introduced the static compression to planetesimal formation. As sources of the static compression, we introduced the ram pressure of the disk gas and the self-gravity. As a result, we found the overall filling factor evolution from dust grains to planetesimals as follows. First, dust grains coagulate with low-speed collisions to form highly porous structure. When the filling factor comes to 10^{-4}, the static compression by ram pressure of the disk gas becomes effective. The dust aggregates continue to coagulate keeping the internal density such that the compressive strength is equal to the ram pressure

of the gas. When the mass of the aggregates reaches 10^{11} g, the self-gravity compression becomes more effective than the ram pressure of the gas. Then, the aggregates continue to coagulate with their compressive strength being equal to the self-gravitational pressure. The final products are 10 km-sized bodies with filling factor of 10^{-1}, which are similar to comets in our solar system, which are believed to be the remnants of planetesimals.

Moreover, the revealed evolution path overcomes the three barriers of planetesimal formation, which are the radial drift, fragmentation (for icy particles), and bouncing problems. Thus, this theory is proposing the first coherent planetesimal formation scenario from grains.

FIgure 5.1 illustrates the conclusions of the proposed scenario in this thesis. In our sce-

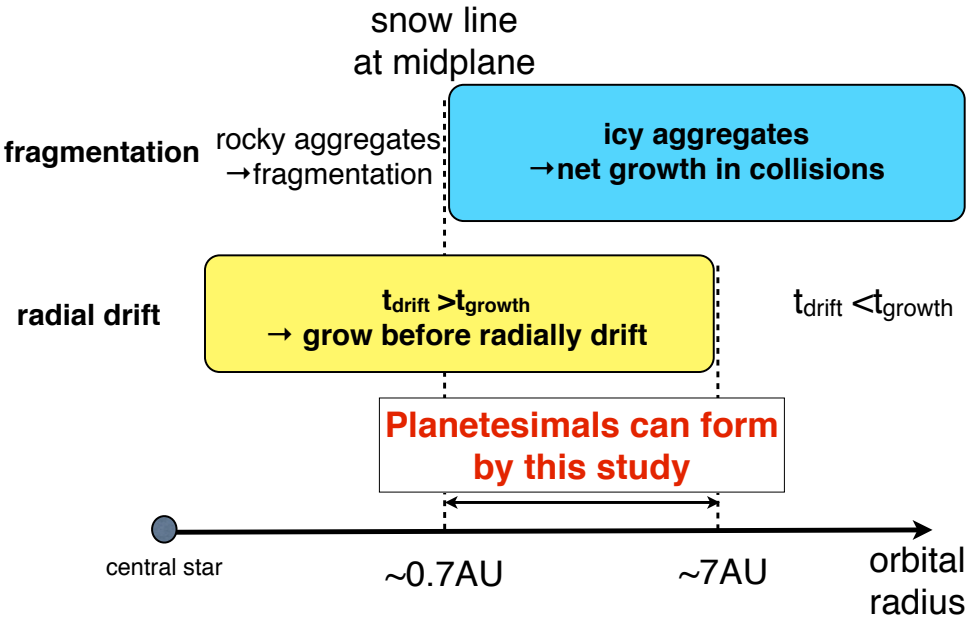

Fig. 5.1 The illustration of the planetesimal forming region in protoplanetary disks by proposed scenario in this thesis. Fragmentation represents the fragmentation barrier, which can be avoided beyond the snowline. Radial drift represents the radial drift barrier, which can be avoided inner region where growth timescale is less than the drifting timescale.

nario, fragmentation barrier is overcomed by considering icy aggregates. Thus, the scenario is applicable to the region beyond the snowline. The location of the snowline is still under debate. In the MMSN model (Hayashi, 1981), the temperature is calculated by assuming that the disk is optically thin. In this case, the snowline is at 2.7 AU. However, protoplanetary disks are thought to be optically thick. Thus, the midplane temperature is expected to be lower than MMSN. For example, the interior temperature in the model of Chiang et al. (2001) is even less than 170K at 1 AU. In the adopted model, the snowline locates at ~ 0.7

AU.

The outer radius where the proposed scenario is applicable is determined by the balance between the dust growth and drift timescale. In the outer region in disks, the dust aggregates radially drift before they grow to planetesimals. The critical radius inside which the dust aggregates can form planetesimals is sensitive to disk parameters. In the adopted model, the critical radius is ~ 7 AU. In this thesis, we demonstrated that more massive disk has larger critical outer radius to form planetesimals.

In Chapter 4, we calculated the optical properties of extremely porous aggregates. We found that the absorption cross section of extremely porous aggregates are characterized by af, where a is the dust radius and f is the filling factor. The scattering cross section is, on the other hand, characterized by af at the shorter wavelengths but larger in more porous aggregates at the longer wavelengths. We also derived the analytical expressions of the absorption and scattering opacities. The expressions greatly reduce the computational time to calculate the opacities. In addition, we proposed a method to distinguish between extremely porous aggregates ($f < 0.1$) and compact grains, in which we use the radial profile of spectral index at millimeter wavelengths. This kind of observations is expected to be performed in the coming ALMA era.

5.2 Outlook

In this thesis, we have revealed a pathway of planetesimal formation via fluffy dust aggregates and found possible differences in opacity between fluffy aggregates and compact grains. We will further proceed the theory to construct a planet formation theory to explain the formations of our solar system and exoplanets. Toward the planet formation theory, we have to construct a formation theory of planets from dust grains. Moreover, the forming process should be confirmed by observations of protoplanetary disks and should be consistent with information of our solar system. To achieve the three goals, which are the planet formation theory from dust grains, observational evidence of growth process, and the consistency with our solar system, we are planning three future works as follows.

5.2.1 Planet formation from dust grains

We have shown that we can obtain a planetesimal distribution which depends on the initial properties of protoplanetary disks by introducing static compression. This has a strong influence on the later stage of planet formation from planetesimals to planets. The later stage

always assumed a planetesimal distribution as an initial condition and calculate coagulation by N-body simulations (e.g., Kokubo & Ida, 1998) or statistical approach (e.g., Inaba et al., 2001). However, the resultant protoplanets or planets strongly depend on the initial size and orbital distribution of planetesimals (e.g., Kobayashi et al., 2011). Thus, initial planetesimal size and orbital distributions are quite important for the subsequent planet formation.

To obtain the planetesimal distribution, we will run a series of simulations of dust coagulation with porosity evolution. This kind of simulations have been done with Monte Carlo method (i.e., Zsom et al., 2010) or statistical method (i.e., Okuzumi et al., 2012). Because the statistical approach with the volume averaging method (Okuzumi et al., 2009) computationally costs much less than the Monte Carlo, we use the statistical approach. To trace the porosity evolution, we use the same kind of calculaions of Okuzumi et al. (2012), who performed the coagulation simulations with collisional compression. We will introduce the static compression to the coagulation simulations to reveal the time evolution of the planetesimal distribution. We will also introduce the effects of the gravitational focusing in statistical approach (e.g., Kobayashi et al., 2011). The gravitational focusing enables us to trace the runaway and oligarchic growth stage. In this way, we can complete the overall simulations from dust grains to planets.

Obtaining the planetesimal distribution is unique compared with other scenarios. For example, planetesimal formation by streaming instability (e.g., Johansen et al., 2007) does not introduce the size distribution and coagulations because of the huge computational costs. In addition, the instability is expected to be suppressed in turbulent disks. For another example, the direct coagulation by mass transfer (e.g., Drążkowska et al., 2013) has only a few planetesimals and they do not obtain the statistical planetesimal distribution. Compared with these theories, the proposed scenario has an advantage that planetesimal distribution can be obtained by numerical approach and thus easily connect to later stage of planet formation.

5.2.2 Testing the porosity evolution theory in protoplanetary disks with radio observations

Observational tests of the proposed theory must be performed. One way to test the theory is observations of protoplanetary disks, where the dust coagulation is ongoing. Protoplanetary disks have been observed at multi wavelengths from infrared to millimeter wave. Although planetesimals are too large to observe in protoplanetary disks, dust grains whose radius is micron to millimeter is observable in these observations. In the previous studies of dust

coagulations, dust grains are assumed to be spherical. For example, Dullemond & Dominik (2005) or Birnstiel et al. (2012) calculated the expected SED by dust coagulation. However, the dust coagulation or the radial drift is too rapid to explain the observed SEDs. The most important discrepancy between theories and observations is spectral index at sub-mm wavelengths. Although observations have indicated that dust grains has a size of 1 mm at least, the dust grains can not grow to mm-sized bodies because of the radial drift.

We have already shown that porous dust aggregates can avoid the radial drift. Therefore, proposed scenario has a possibility to explain the observed spectrum. To compare the theory with observations, we will run a radiative transfer calculations of the results of numerical simulations of dust coagulations with porosity evolution as discussed in the previous section. Because small grains greatly affect the observational spectrum, we will introduce the fragmentation effects. Then, we will try to explain the SEDs by changing the initial conditions or the fragmentation effects.

We will also challenge to obtain the observational evidence of fluffy dust aggregates. As discussed in Chapter 4, the compactness of dust aggregates is difficult to observe but we can distinguish between compact and fluffy dust aggregates by observing the radial distribution of the opacity slope. Therefore, we are planning to obtain the continuum at 1 mm and 3 mm band of a protoplanetary disk with a spatial resolution as high as 10 AU scale. The resolution at the bands is achievable with ALMA. Thus, using continuum observations of ALMA, we will observationally evidence the existence of fluffy dust aggregates.

5.2.3 Thermal history of meteorites in our solar system

One of the advantage of planet formation as a research field compared to other astronomical fields is that we can obtain information of formation of our solar system as an example of planet formation. However, the formation of our solar system occurred 45 billion years ago and thus we cannot directly obtain the information of the formation process. One of the most striking trace is the thermal history of meteorites. For example, many chondrites have experienced aqueous alteration. This process is believed as an evidence of heating events inside the parent asteroids, or planetesimals. However, it is difficult to avoid the aqueous alteration inside icy planetesimals, and thus explanations of chondrites without aqueous alteration is still on debate.

The heating source of planetesimals is the radioactive decay of Aluminum inside the planetesimals. When the cooling timescale is longer than the heating timescale, the planetesimals possess some heat and the temperature increases. This heating mechanism helps

aqueous alteration. The thermal history of planetesimals has been investigated assuming planetesimals as an initial body (e.g., Wakita & Sekiya, 2011). However, the planetesimals are temporal objects on the dust coagulation from dust grains to planets. Because we revealed the coagulation process from grains to planetesimals, we can apply the theory to reveal the thermal history of planetesimals. As a result, we can trace the coagulation and thermal evolution inside dust aggregates simultaneously.

One of the advantages of our theory is that fluffy dust aggregates may avoid aqueous alteration because the pressure inside the aggregates are too low to contain water but ice is expected to sublimate. This can potentially explain the planetesimals without aqueous alteration beyond the snowline. Although there are still many obstacles to explain the formation of our solar system to be consistent with current observations of meteorites, the proposed scenario of planetesimal formation can add a new insight into our solar system formation with investigating the thermal history of solid bodies in protoplanetary disks.

References

Adachi, I., Hayashi, C., & Nakazawa, K. 1976, Progress of Theoretical Physics, 56, 1756

Adams, F. C., Lada, C. J., & Shu, F. H. 1987, ApJ, 312, 788

A'Hearn, M. F. 2011, ARA&A, 49, 281

Andrews, S. M. & Williams, J. P. 2005, ApJ, 631, 1134

Andrews, S. M. & Williams, J. P. 2007, ApJ, 659, 705

Balbus, S. A. & Hawley, J. F. 1991, ApJ, 376, 214

Beckwith, S. V. W. & Sargent, A. I. 1991, ApJ, 381, 250

Beckwith, S. V. W., Sargent, A. I., Chini, R. S., & Guesten, R. 1990, AJ, 99, 924

Birnstiel, T., Andrews, S. M., & Ercolano, B. 2012, A&A, 544, A79

Birnstiel, T., Dullemond, C. P., & Brauer, F. 2010a, A&A, 513, A79

Birnstiel, T., Ricci, L., Trotta, F., et al. 2010b, A&A, 516, L14

Blum, J. 2004, in Astronomical Society of the Pacific Conference Series, Vol. 309, Astrophysics of Dust, ed. A. N. Witt, G. C. Clayton, & B. T. Draine, 369

Blum, J. & Münch, M. 1993, Icarus, 106, 151

Blum, J. & Wurm, G. 2000, Icarus, 143, 138

Blum, J. & Wurm, G. 2008, ARA&A, 46, 21

Bohren, C. F. & Huffman, D. R. 1983, Absorption and scattering of light by small particles

Brauer, F., Dullemond, C. P., & Henning, T. 2008, A&A, 480, 859

Calvet, N., Patino, A., Magris, G. C., & D'Alessio, P. 1991, ApJ, 380, 617

Chiang, E. I. & Goldreich, P. 1997, ApJ, 490, 368

Chiang, E. I., Joung, M. K., Creech-Eakman, M. J., et al. 2001, ApJ, 547, 1077

Chokshi, A., Tielens, A. G. G. M., & Hollenbach, D. 1993, ApJ, 407, 806

D'Alessio, P., Calvet, N., & Hartmann, L. 2001, ApJ, 553, 321

Dominik, C. & Tielens, A. G. G. M. 1995, Philosophical Magazine, Part A, 72, 783

Dominik, C. & Tielens, A. G. G. M. 1997, ApJ, 480, 647

Draine, B. T. 1988, ApJ, 333, 848

Draine, B. T. & Flatau, P. J. 1994, Journal of the Optical Society of America A, 11, 1491

Drążkowska, J., Windmark, F., & Dullemond, C. P. 2013, A&A, 556, A37

Dubrulle, B., Morfill, G., & Sterzik, M. 1995, Icarus, 114, 237

Dullemond, C. P. & Dominik, C. 2005, A&A, 434, 971

Garaud, P., Meru, F., Galvagni, M., & Olczak, C. 2013, ApJ, 764, 146

Greenwood, J. & Johnson, K. 2006, Journal of Colloid and Interface Science, 296, 284

Guilloteau, S., Dutrey, A., Piétu, V., & Boehler, Y. 2011, A&A, 529, A105

Güttler, C., Blum, J., Zsom, A., Ormel, C. W., & Dullemond, C. P. 2010, A&A, 513, A56

Güttler, C., Krause, M., Geretshauser, R. J., Speith, R., & Blum, J. 2009, ApJ, 701, 130

Haile, J. M. 1992, Molecular Dynamics Simulation: Elementary Methods, 1st edn. (New York, NY, USA: John Wiley & Sons, Inc.)

Hayashi, C. 1981, Progress of Theoretical Physics Supplement, 70, 35

Hayashi, C., Nakazawa, K., & Nakagawa, Y. 1985, in Protostars and Planets II, ed. D. C. Black & M. S. Matthews, 1100–1153

Heim, L.-O., Blum, J., Preuss, M., & Butt, H.-J. 1999, Physical Review Letters, 83, 3328

Hernández, J., Hartmann, L., Megeath, T., et al. 2007, ApJ, 662, 1067

Hollenbach, D. J., Yorke, H. W., & Johnstone, D. 2000, Protostars and Planets IV, 401

Inaba, S., Tanaka, H., Nakazawa, K., Wetherill, G. W., & Kokubo, E. 2001, Icarus, 149, 235

Isella, A., Carpenter, J. M., & Sargent, A. I. 2009, ApJ, 701, 260

Isella, A., Carpenter, J. M., & Sargent, A. I. 2010, ApJ, 714, 1746

Johansen, A., Oishi, J. S., Mac Low, M.-M., et al. 2007, Nature, 448, 1022

Johnson, K. L., Kendall, K., & Roberts, A. D. 1971, Royal Society of London Proceedings Series A, 324, 301

Kataoka, A., Machida, M. N., & Tomisaka, K. 2012, ApJ, 761, 40

Kataoka, A., Okuzumi, S., Tanaka, H., & Nomura, H. 2014, A&A, 568, A42

Kataoka, A., Tanaka, H., Okuzumi, S., & Wada, K. 2013a, A&A, 554, A4

Kataoka, A., Tanaka, H., Okuzumi, S., & Wada, K. 2013b, A&A, 557, L4

Kempf, S., Pfalzner, S., & Henning, T. K. 1999, Icarus, 141, 388

Kenyon, S. J. & Hartmann, L. 1987, ApJ, 323, 714

Kimura, H., Kolokolova, L., & Mann, I. 2003, A&A, 407, L5

Kimura, H., Kolokolova, L., & Mann, I. 2006, A&A, 449, 1243

Kobayashi, H., Tanaka, H., & Krivov, A. V. 2011, ApJ, 738, 35

Kokubo, E. & Ida, S. 1996, Icarus, 123, 180

Kokubo, E. & Ida, S. 1998, Icarus, 131, 171

Kolokolova, L., Kimura, H., Kiselev, N., & Rosenbush, V. 2007, A&A, 463, 1189

Kothe, S., Blum, J., Weidling, R., & Güttler, C. 2013, Icarus, 225, 75

Kozasa, T., Blum, J., & Mukai, T. 1992, A&A, 263, 423

Krause, M. & Blum, J. 2004, Physical Review Letters, 93, 021103

Kudo, T., Kouchi, A., Arakawa, M., & Nakano, H. 2002, Meteoritics and Planetary Science, 37, 1975

Lambrechts, M. & Johansen, A. 2012, A&A, 544, A32

Langkowski, D., Teiser, J., & Blum, J. 2008, ApJ, 675, 764

Larson, R. B. 1969, MNRAS, 145, 271

Li, A. & Greenberg, J. M. 1997, A&A, 323, 566

Lommen, D. J. P., van Dishoeck, E. F., Wright, C. M., et al. 2010, A&A, 515, A77

Lynden-Bell, D. & Pringle, J. E. 1974, MNRAS, 168, 603

Machida, M. N., Inutsuka, S.-i., & Matsumoto, T. 2010, ApJ, 724, 1006

Mathis, J. S., Rumpl, W., & Nordsieck, K. H. 1977, ApJ, 217, 425

Meakin, P. 1991, Reviews of Geophysics, 29, 317

Min, M., Dominik, C., Hovenier, J. W., de Koter, A., & Waters, L. B. F. M. 2006, A&A, 445, 1005

Min, M., Hovenier, J. W., & de Koter, A. 2003, A&A, 404, 35

Min, M., Hovenier, J. W., & de Koter, A. 2005, A&A, 432, 909

Min, M., Waters, L. B. F. M., de Koter, A., et al. 2007, A&A, 462, 667

Miyake, K. & Nakagawa, Y. 1993, Icarus, 106, 20

Mukai, T., Ishimoto, H., Kozasa, T., Blum, J., & Greenberg, J. M. 1992, A&A, 262, 315

Mulders, G. D., Min, M., Dominik, C., Debes, J. H., & Schneider, G. 2013, A&A, 549, A112

Nakagawa, Y., Nakazawa, K., & Hayashi, C. 1981, Icarus, 45, 517

Nakagawa, Y., Sekiya, M., & Hayashi, C. 1986, Icarus, 67, 375

Okuzumi, S. 2009, ApJ, 698, 1122

Okuzumi, S., Tanaka, H., Kobayashi, H., & Wada, K. 2012, ApJ, 752, 106

Okuzumi, S., Tanaka, H., & Sakagami, M.-a. 2009, ApJ, 707, 1247

Ormel, C. W. & Cuzzi, J. N. 2007, A&A, 466, 413

Ormel, C. W., Paszun, D., Dominik, C., & Tielens, A. G. G. M. 2009, A&A, 502, 845

Ormel, C. W., Spaans, M., & Tielens, A. G. G. M. 2007, A&A, 461, 215

Ossenkopf, V. 1993, A&A, 280, 617

Pagani, L., Steinacker, J., Bacmann, A., Stutz, A., & Henning, T. 2010, Science, 329, 1622

Paszun, D. & Dominik, C. 2006, Icarus, 182, 274

Paszun, D. & Dominik, C. 2008, A&A, 484, 859

Paszun, D. & Dominik, C. 2009, A&A, 507, 1023

Pérez, L. M., Carpenter, J. M., Chandler, C. J., et al. 2012, ApJ, 760, L17

Pinilla, P., Birnstiel, T., Ricci, L., et al. 2012, A&A, 538, A114

Pollack, J. B., Hollenbach, D., Beckwith, S., et al. 1994, ApJ, 421, 615

Poppe, T., Blum, J., & Henning, T. 2000, ApJ, 533, 454

Ricci, L., Testi, L., Natta, A., & Brooks, K. J. 2010a, A&A, 521, A66

Ricci, L., Testi, L., Natta, A., et al. 2010b, A&A, 512, A15

Ricci, L., Trotta, F., Testi, L., et al. 2012, A&A, 540, A6

Ros, K. & Johansen, A. 2013, A&A, 552, A137

Rucinski, S. M. 1985, AJ, 90, 2321

Schwartz, P. R. 1982, ApJ, 252, 589

Seizinger, A. & Kley, W. 2013, A&A, 551, A65

Seizinger, A., Speith, R., & Kley, W. 2012, A&A, 541, A59

Sekiya, M. 1998, Icarus, 133, 298

Shakura, N. I. & Sunyaev, R. A. 1973, A&A, 24, 337

Shen, Y., Draine, B. T., & Johnson, E. T. 2008, ApJ, 689, 260

Shen, Y., Draine, B. T., & Johnson, E. T. 2009, ApJ, 696, 2126

Smirnov, B. M. 1990, Phys. Rep., 188, 1

Suyama, T., Wada, K., & Tanaka, H. 2008, ApJ, 684, 1310

Suyama, T., Wada, K., Tanaka, H., & Okuzumi, S. 2012, ApJ, 753, 115

Tanaka, H., Himeno, Y., & Ida, S. 2005, ApJ, 625, 414

Tanaka, H., Wada, K., Suyama, T., & Okuzumi, S. 2012, Progress of Theoretical Physics Supplement, 195, 101

van Boekel, R., Min, M., Waters, L. B. F. M., et al. 2005, A&A, 437, 189

van der Marel, N., van Dishoeck, E. F., Bruderer, S., et al. 2013, Science, 340, 1199

Voshchinnikov, N. V., Il'in, V. B., & Henning, T. 2005, A&A, 429, 371

Wada, K., Tanaka, H., Okuzumi, S., et al. 2013, A&A

Wada, K., Tanaka, H., Suyama, T., Kimura, H., & Yamamoto, T. 2007, ApJ, 661, 320

Wada, K., Tanaka, H., Suyama, T., Kimura, H., & Yamamoto, T. 2008, ApJ, 677, 1296

Wada, K., Tanaka, H., Suyama, T., Kimura, H., & Yamamoto, T. 2009, ApJ, 702, 1490

Wada, K., Tanaka, H., Suyama, T., Kimura, H., & Yamamoto, T. 2011, ApJ, 737, 36

Wakita, S. & Sekiya, M. 2011, Earth, Planets, and Space, 63, 1193

Warren, S. G. 1984, Appl. Opt., 23, 1206

Weidenschilling, S. J. 1977, MNRAS, 180, 57

Weidenschilling, S. J. 1980, Icarus, 44, 172

Weidenschilling, S. J. & Cuzzi, J. N. 1993, in Protostars and Planets III, ed. E. H. Levy & J. I. Lunine, 1031–1060

Weidling, R., Güttler, C., & Blum, J. 2012, Icarus, 218, 688

Weingartner, J. C. & Draine, B. T. 2001, ApJ, 548, 296

Windmark, F., Birnstiel, T., Güttler, C., et al. 2012a, A&A, 540, A73

Windmark, F., Birnstiel, T., Ormel, C. W., & Dullemond, C. P. 2012b, A&A, 544, L16

Wurm, G. & Blum, J. 1998, Icarus, 132, 125

Wyatt, M. C. 2008, ARA&A, 46, 339

Youdin, A. N. & Lithwick, Y. 2007, Icarus, 192, 588

Youdin, A. N. & Shu, F. H. 2002, ApJ, 580, 494

Zsom, A., Ormel, C. W., Dullemond, C. P., & Henning, T. 2011, A&A, 534, A73

Zsom, A., Ormel, C. W., Güttler, C., Blum, J., & Dullemond, C. P. 2010, A&A, 513, A57

Zubko, V. G., Mennella, V., Colangeli, L., & Bussoletti, E. 1996, MNRAS, 282, 1321

Acknowledgements

I am grateful for the supervisor, Kohji Tomisaka, who supported my PhD life in NAOJ, and also provided a great insight into star formation through a collaboration work (Kataoka et al., 2012). I am also grateful for the collaborators of this research, Hidekazu Tanaka, Satoshi Okuzumi, Koji Wada, and Hideko Nomura. And special thanks to Masaomi Tanaka, Masahiro Machida, Takayuki Muto, Munetake Momose, Misato Fukagawa, Takashi Tsukagoshi, Hiroshi Kobayashi, Takayuki Tanigawa, Tomoyuki Hanawa, Hiroko Shinnaga, Mareki Honma and his group, people in the Division of Theoretical Astronomy in NAOJ, people in Department of Astronomy in Kyoto University, Sanemichi Takahashi, Yuri Fujii, Masanobu Kunitomo, Shigeo Kimura, Kazunori Akiyama, Andrea Isella, Luca Ricci, Kees Dullemond, Paola Pinilla, Joanna Drazkowska, Frederik Windmark, Anders Johansen, Michiel Lambrechts, Katrin Ros, my friends, and my family.